DESIGN AND OPTIMIZATION OF HIGH-PERFORMANCE GETE-BASED THERMOELECTRIC MATERIALS

A Thesis submitted by

Wanyu Lyu

For the award of

Doctor of Philosophy

2023

ABSTRACT

Thermoelectric materials can achieve a conversion effect between heat energy and electricity. The conversion efficiency of thermoelectric materials is determined by the dimensionless *figure of merit* (zT), $zT = S^2\sigma T/\kappa_{tot}$, where S, σ, $S^2\sigma$, and κ_{tot} represent the Seebeck coefficient, electrical conductivity, power factor, and total thermal conductivity, respectively. The pristine GeTe has a high σ due to the high carrier concentration (n_p) induced by intrinsic Ge vacancies. This high n_p also led to a low S which obtained a relatively low $S^2\sigma$. Thus, combined with a relatively high κ_{tot}, a peak zT value of ~1 was obtained in GeTe. Rare earth elements doping can affect the transport properties of GeTe thermoelectric materials with below advantages, including aliovalent elements doping to reduce n_p, the localized magnetic moments due to the unfilled 4f-electrons, the large mass fluctuation, and strain-field fluctuation effect on point defect scattering. All these features motivate us to investigate the rare earth elements doped GeTe system for the purpose of reducing the κ_{lat}, exploring the effect of doping with local magnetic moment elements on the thermoelectric properties of GeTe. This project is conducted in the following parts: The thermoelectric performance of GeTe-based thermoelectric materials can be significantly enhanced by substituting REs (Eu, Gd, Er, and Tm) at the Ge site of GeTe. The zT_{ave} *are* increased from 0.38 of pristine GeTe to ~ 0.60 of $Ge_{0.98}RE_{0.02}Te$ at the entire temperature range. Lu was found to have a relatively small radius and electronegativity difference with Ge compared with other rare earth elements, which can induce a high doping level in GeTe. A peak zT of 1.75 at 673 K and an average zT of 0.92 within the temperature range of 303-723 K are obtained in $Ge_{0.9}Lu_{0.02}Sb_{0.08}Te$. Rare earth Nd doping in the TAGS-85 ($GeTe_{85}(AgSbTe_2)_{15}$) system obtained the highest zT values of 1.65 at 727 K. Overall, several breakthroughs in GeTe thermoelectrics have been made and documented in journal papers. The challenges of high-performance n-type GeTe and the practical application of GeTe thermoelectric devices still need to be further investigated.

CERTIFICATION OF THESIS

I Wanyu Lyu declare that the PhD Thesis entitled “Design and optimization of high-performance GeTe-based thermoelectric materials” is not more than 100,000 words in length including quotes and exclusive of tables, figures, appendices, bibliography, references, and footnotes.

This Thesis is the work of Wanyu Lyu except where otherwise acknowledged, with the majority of the contribution to the papers presented as a Thesis by Publication undertaken by the student. The work is original and has not previously been submitted for any other award, except where acknowledged.

[redacted]

Date:28/02/2023

Endorsed by:

[redacted]

Zhigang Chen
Principal Supervisor

Hao Wang
Associate Supervisor

Jin Zou
Associate Supervisor

Student and supervisors’ signatures of endorsement are held at the University.

STATEMENT OF CONTRIBUTION

Paper 1:

Lyu, W.-Y., Liu, W.-D., Li, M., Hong, M., Guo, K., Luo, J., Xing, J-J., Sun, Q., Xu, S-D., Zou, J., Chen, Z.-G. (2022). The effect of rare earth element doping on thermoelectric properties of GeTe. *Chemical Engineering Journal*, 446. https://doi.org/ 10.1016/j.cej.2022.137278

The student **Wanyu Lyu** contributed 70% to this paper. Collectively Wei-Di Liu, Meng Li, Min Hong, Kai Guo, Jun Luo, Juanjuan Xing, Qiang Sun, Shengduo Xu, Jin Zou, Zhi-Gang Chen contributed the remainder.

Paper 2:

Lyu, W.-Y., Liu, W.-D., Li, M., Shi, X.-L., Hong, M., Cao, T., Guo, K., Luo, J., Zou, J., Chen, Z.-G. (2023). Condensed Point Defects Enhance Thermoelectric Performance of Rare-Earth Lu-Doped GeTe. *Journal of Materials Science & Technology*. https://doi.org/10.1016/j.jmst.2023.01.004

The student **Wanyu Lyu** contributed 70% to this paper. Collectively Wei-Di Liu, Meng Li, Xiao-Lei Shi, Min Hong, Tianyi Cao, Kai Guo, Jun Luo, Jin Zou, Zhi-Gang Chen contributed the remainder.

Paper 3:

Lyu, W. Y., Hong, M., Liu, W. D., Li, M., Sun, Q., Xu, S. D., Zou, J., Chen, Z.-G. (2021). Rare-Earth Nd Inducing Record-High Thermoelectric Performance of $(GeTe)_{85}(AgSbTe_2)_{15}$. *Energy Material Advances, 2021*, 1-8. doi:10.34133/2021/2414286

The student **Wanyu Lyu** contributed 70% to this paper. Collectively Min Hong, Wei Di Liu, Meng Li, Qiang Sun, Sheng Duo Xu, Jin Zou, and Zhi-Gang Chen contributed the remainder.

ACKNOWLEDGEMENTS

” Necessity, weight, and value are three concepts inextricably bound: only necessity is heavy, and only what is heavy has value.”

— Milan Kundera, The Unbearable Lightness of Being

At first, I would like to express my great appreciation to my principal supervisor, Prof. Zhi-Gang Chen, for his great help with my research and life. And thanks to my associated supervisors, Prof. Jin Zou and Prof. Hao Wang, for their professional guidance and support. Thanks to Dr. Wei-di Liu for giving me full support for my research with his professional knowledge and patience. Thanks to A. Prof. Min Hong for his great help with my research. At last, I would like to thank Prof. Kai Guo for his great help and support.

Secondly, I would like to thank other members of my group. Thanks to Dr. Meng Li, who helps me with my research and calculations and, as a good friend, gives me a lot of help in life. Dr. Xiao-Lei Shi, who helped me with professional experience in experimentation and knowledge, Dr. Han Gao and Dr. Qiang Sun, who provided skillful material characterizations, Thanks to Dr. Sheng-Duo Xu, Dr. Yuan Wang, and Dr. Lijun Wang for their kind help. Thanks to Ms. Shuai Sun, Mr. Tian-Yi Cao, and Mr. Bo-Xuan Hu, Mr. Wen-Yi Chen, Mr. Yuanqing Mao, and Mr. Qisuo Yang for their kindness and help. I would also like to thank people from the thermoelectric materials group at Shanghai University for their kind help.

Thirdly, I would also like to acknowledge the Australian Research Council for supporting my research work. I would like to acknowledge the CSC for providing me with a living stipend. The Australian Microscopy and Microanalysis Research Facility (AMMRF) for providing characterization facilities and supportive service, the Research Computing Centre (RCC) at

the University of Queensland, and the National Computational Infrastructure (NCI) supported by the Australian Government for providing computation resources and services This research has been supported by an Australian Government Research Training Program Scholarship.

Finally, I would like to thank my parents. They taught me the most important quality of being kind to others. Then, I want to thank those very important friends in my life. They are so sincere and kind that when I feel lost, I have the power to resist everything when I look at them. They have always been my role models. Thanks to Chen Bi, she has always supported and encouraged me during my Ph.D. study. Thanks to Xiaomei Yao, her tenderness and patience allowed me to open myself and learn to express myself. And my good friends Ma Wan, Zheng Rui, Hua Hua, Fang Fang, and Qi Jun are such sincere and kind people; whether it is financial or emotional support, they are always ready to help me. Thanks to NONO for accompanying me and giving me warm help in Brisbane.

TABLE OF CONTENTS

LIST OF FIGURES

ABBREVIATIONS

BSE: back-scattered electrons

BTE: boltzmann transport equation

CBM: conduction band minimum

DFT: density functional theory

DOS: density-of-states

DSC: differential scanning calorimetry

EBSD: electron back-scattered diffraction

EDS/EDX: energy dispersive (X-ray) spectroscope

FFT: fast fourier transform

FIB: focused ion beam

GGA: generalized gradient approximation

HAADF: high angle annular dark field

HOMO: the highest occupied molecular orbital

LDA: local density approximation

LFA: laser flash analysis

LUMO: the lowest unoccupied molecular orbital

PAW: projector augmented wave method

PBE: the Perdew-Burke-Ernzerh of exchange correlation functional

SAED: selected area electron diffraction

SE: secondary electrons

SEM: scanning electron microscope

SOC: spin-orbital coupling

SPS: spark plasma sintering

SPB: single parabolic band

TE: thermoelectric

TEC: thermoelectric cooler

TEG: thermoelectric generator

TEM: transmission electron microscope

VBM: valence band maximum

XRD: X-ray diffraction
XPS: X-ray photoelectron spectroscope
WQ: water quenching

CHAPTER 1: INTRODUCTION

1.1. Background

The population of the world has developed steadily over the last few decades, with rapidly increasing economic and industrial development. The oil crisis and environmental issues were also brought on. High fossil energy consumption has not only impeded business growth but has also contributed to many social difficulties. For instance, the oil rush, and rising prices, and the global energy dispute prevention. Fossil fuels are a non-clean source of carbon. When burnt and consumed, toxic gases are produced, the ozone layer is damaged, greenhouses are activated, and the human living condition is greatly threatened. Consequently, green and sustainable energy conversion materials are emerging and booming under the concurrent pressure of energy scarcity and environmental degradation. Wind power generation and the application of solar cells have fully alleviated energy exhaustion and environmental pollution caused by fossil fuel combustion. However, wind energy and solar energy are extensively used for commercial utilization which focuses on the efficiency of energy utilization. Besides, another way to improve energy efficiency is to recycle waste heat. Heating, vehicle exhaust, and manufacturing processes produce a large amount of waste heat that can be converted by using thermoelectricity into electricity. Because thermo-electric power generators are solid, stable, and portable units that do not have moving parts, they are perfect for small, distributed power generation. Efforts to replace the alternator in cars with a thermoelectric generator on the exhaust flow are now underway, which improves fuel efficiency. Progress in thermoelectric power could also allow the replacement of compression-based cooling by solid-state Peltier coolers.

Thermoelectric materials (TE) that can transform heat into electricity and vice versa draw much attention in terms of waste heat utilization (Kusrini et al., 2018; Liebl, 2009; Park et al., 2018; James R. Salvador et al., 2012), including automobiles (General Motors and BMW), thermonuclear power space mission (Prilepo, Pustovalov, Sinyavskiy, Sudak, & Yatsenko, 2012), and solid-state refrigeration, such as conventional refrigeration for portable refrigerators and medicinal keeping (Lafaurie Ponce, Chejne, Ramirez Aristeguieta, Gómez, & Múnera Cano, 2019; Sharma, Dwivedi, & Pandit, 2014). With the development of thermoelectrical materials, researchers are now developing various flexible, wearable thermoelectric materials, including intelligent body temperature watches and power generation biomedical detectors (L. Huang et al., 2019; T. Sun et al., 2020). Given the great number of potential applications and significant academic and scientific effects, thermoelectric materials have received massive attention over the last few decades. Thermoelectric efficiency is evaluated by the dimensionless figure of merit $zT=\frac{S^2\sigma}{\kappa_{tot}}T$, where S, σ, κ_{tot} and T are the Seebeck coefficient, electrical conductivity, thermal conductivity, and absolute temperature, respectively. Among them, the first three parameters are coupled with each other. This property of TE limits the efficiency of thermoelectric materials. Such as, the change of the Seebeck coefficient with carrier concentration is opposite to the relationship between conductivity and carrier concentration. The $S^2\sigma$ is defined as a power factor that can assess the electrical property in total. There are many methods focused on easing this restriction in thermoelectric materials, such as tuning the carrier concentration to an optimized level (Pei, LaLonde, et al., 2011; Pei, May, & Snyder, 2011), band engineering including resonance band level (M. Hong, Z. G. Chen, et al., 2018), decreasing the energy of light and heavy valence band (Pei, Wang, & Snyder, 2012; Tang, Gibbs, et al., 2015), band alinement (W. He et al., 2019), et al. Also, inducing the nanostructured materials to decrease the lattice thermal conductivity (Girard et al., 2010; Yang et al., 2015) and flexible thin-film preparation all push the development of thermoelectric (Y. Wang et al., 2019). Among them, the mid-temperature GeTe has been studied recently due to its multi-degree of tuning performance and without the high toxicity lead as PbTe. Adopting the easily optimized carrier concentration and structure information, the GeTe-based materials have been extensively investigated.

The IV-VI chalcogenides AB (A = Ge, Sn, Pb, and B = Te) are the state-of-the-art materials for thermoelectric applications in the temperature range of 400 K–800 K (H. L. Liu et al., 2012). PbTe has been studied comprehensively and extensively as one of the classical thermoelectric materials that also has high thermoelectric properties (Kim, Zhao, Kanatzidis, & Seidman, 2017). However, the high toxicity of Pb limited its practical application. GeTe with a high carrier concentration resulting from easily formed Ge vacancies was considered to be a low-efficiency thermoelectric material. The lower formation energy of Ge vacancies results in a high carrier concentration (~10^{21} cm^{-3}). This hole density is much higher than the optimal level, so that pristine GeTe shows high electrical conductivity and a lower Seebeck coefficient with the peak *zT* up to 0.8 at 720 K (Levin, Besser, & Hanus, 2013). Nevertheless, it is easy to decrease the carrier concentration by doping with aliovalent elements or alloying with another thermoelectric material. Such as, substituting Ge with Pb as a donor dopant, which can decrease the electrical conductivity and increase the Seebeck coefficient. The Sb substitute in the Ge site leads to the highest *zT* value of 2. GeTe crystallized in the cubic phase at high temperature and then underwent a phase transition to a rhombohedral structure when the temperature was reduced to low temperature. Due to the higher symmetry of the cubic phase, it can achieve higher performance. Therefore, some research focuses on decreasing the phase transition temperature to get higher performance. In addition, IV–VI chalcogenides usually have multiple valence-bands that favorably achieve band engineering optimization in thermoelectric materials. Thus, the improvement of power factors by decreasing the energy difference between light band valence and heavy band valence in GeTe were widely implemented. Considering these intrinsic properties and the degree of regulation freedom, GeTe has been extensively studied and has achieved considerable improvements.

1.2. Objective and scope

This project aims to optimize the thermoelectric performance of GeTe-based materials. So that the commercialization of GeTe-based materials can be pushed, as well as to alleviate energy stress and environmental pollution. To fulfil this goal, the specific objectives of the project are listed below：

1. Rare earth elements have a large mass and strain-field fluctuation which can enhance phonon scattering by point defect scattering. Rare earth elements, Eu, Gd, Er, and Tm, were used to investigate the doping effect on lattice thermal conductivity in GeTe system. And the local magnetic moments of rare earth elements affect S was also discussed.

2. The rare earth element doping successfully enhances the zT values of GeTe. However, it is limited by the solubility of rare earth elements. Thus, higher electronegativity Lu was used to further reduce the thermal conductivity in the GeTe system. In addition, the Sb alloying was used to further reduce n_p.

3. To improve the thermoelectric properties of the GeTe system by doping with rare earth elements in the alloyed TAGS-85 system (Tellurium Antimony Germanium Silver with composition $(GeTe)_{85}(AgSbTe_2)_{15}$). The TAGS system has been investigated during the last decades. Among them, the performance of TAGS-85 achieved the best properties both in electrical and thermal performance. This system not only improved the power factor due to the decreased carrier concentration, but also decreased the thermal conductivity. Thus, as a potential system of GeTe, we introduce Nd into the TAGS-85 system to further enhance its properties.

1.3. Thesis outline

This thesis is outlined in 7 chapters in the following sequence:

Chapter 1 is the introduction to this thesis.

Chapter 2 overviews the development history of thermoelectric technology, and the various widely studied thermoelectric materials. The current progress of GeTe-based thermoelectric materials is reviewed, as well as the research gap in GeTe-based thermoelectric materials.

Chapter 3 is the methodology and approach which provide experimental details.

Chapter 4 presents the effect of rare earth element doping on the thermoelectric properties of GeTe. The doping limit induced difference in electrical and thermal properties was highlighted.

Chapter 5 illustrates condensed point defects enhance thermoelectric performance of rare-earth Lu-doped GeTe. 2 mol.% Lu and 8 mol.% Sb co-doping in GeTe achieve a high *zT* value of 1.75 at 673 K.

Chapter 6 shows that rare earth Nd Induced in $(GeTe)_{85}(AgSbTe_2)_{15}$ can obtain high thermoelectric performance in TAGS-85.

Chapter 7 draws the conclusions of this thesis and points out the potential future directions.

CHAPTER 2: LITERATURE REVIEW

In this chapter, we will first overview the development history of thermoelectric technology, including the thermoelectric effect, thermoelectric materials, and applications. Then, the various widely studied thermoelectric materials will be enumerated. The related evaluation parameters of thermoelectric materials will be introduced. As well as the current progress of GeTe-based thermoelectric materials. At last, we clarify the research gap in GeTe-based thermoelectric materials, as well as the new possibilities for advancement in the below literature review.

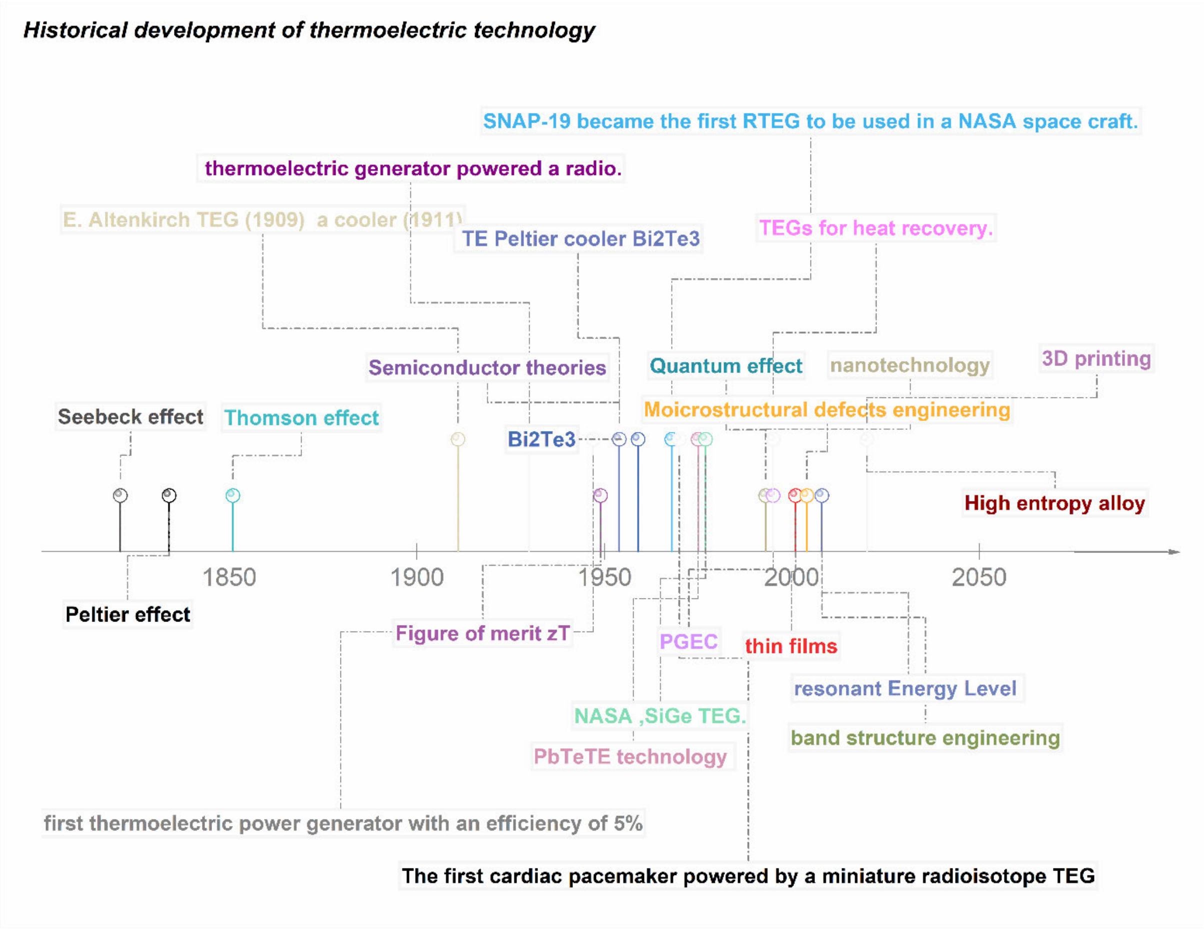

Figure 2.1. Historical development of thermoelectric technology.

2.1. A brief history of thermoelectric technology

Today, the development of thermoelectric materials and devices has entered a new era. Thermoelectric technology related theories have been developed and are gradually improving (Cao, Shi, & Chen, 2023; Davide Beretta et al., 2019; Shi, Zou, & Chen, 2020; Snyder et al., 2020; X. Zhang et al., 2020). The discovery of new thermoelectric materials and the performance improvement of classical materials are developing rapidly. The development of different dimensional materials, including one-dimensional, two-dimensional, and three-dimensional materials, provides new possibilities for thermoelectric materials (Burton, Howells, Atoyo, & Carnie, 2022; Dresselhaus et al., 2007; Jo, Choo, Kim, Heo, & Son, 2019). Thermoelectric devices are also booming in various fields, including medical devices (Ben Amar, Kouki, & Cao, 2015), on-chip device (W.-Y. Chen, Shi, Zou, & Chen, 2022), wearable devices (Kishore, Nozariasbmarz, Poudel, Sanghadasa, & Priya, 2019), etc (R. He, Schierning, & Nielsch, 2018). In this part, we will briefly introduce the development history of thermoelectricity, in order to have a comprehensive understanding of thermoelectric technology and open a window for the future.

2.1.1. Seebeck effect

Thermoelectric effects stemming from a “false discovery” of magnetic deflection induced by temperature difference between two conductors were found by Thomas Johann Seebeck (German) in 1821 Th. J. Seebeck "Magnetische Polarisation der Metalle und Erze Durch Temperatur-Differenz"1822-23 in Ostwald's Klassiker der Exakten Wissenshaften Nr. 70 (1895). Seebeck Biography 1. Seebeck Biography 2.. This magnetic effect was later proved to be induced by an electric current generated from the temperature difference, which is known as the Seebeck effect. After that, Seebeck surveyed various materials to create his “Seebeck system” including simple substance elements, and alloy compounds as well as a qualitative ordering of their relative Seebeck effect. This research makes a big contribution to the following survey about thermoelectrics. In 1910, Werner Haken (Haken, 1910) characterized the Seebeck coefficient (S) and electrical conductivity (σ) of many compounds, and identified the good thermoelectric materials including

Sb_2Te_3, Bi_2Te_3, SnTe, PbTe etc. The Seebeck effect explained by the latter scientist is shown in **Figure 2.2**a, a temperature change between joints 1 and 2 generates a current in the whole conductor, the voltage (ΔV) will be detected between these two conductors. As long as the $\Delta T=T_h-T_c$ is small enough, the relative Seebeck effect (S) will be a constant, written as

$$S=\frac{\Delta V}{\Delta T}\ (\Delta T\rightarrow 0) \tag{2-1}$$

2.1.2. Peltier effect

In 1834, Jean Charles Athanase Peltier discovered that an electrical current can generate a heating or cooling effect at the junction of two dissimilar metals (Peltier, 1834). Although Peltier tried to attribute this phenomenon to the theory of Joule heat dissipation, he inevitably failed to find out the physical origin of the effect. Until 1838, Heinrich Friedrich Emil Lenz proved that when current is forced to flow through different conductors, the junction between different conductors releases and absorbs additional heat with two different directions of current flow (Physik, 1838). This absorbed heat at the junction is proportional to the electrical current. Today, this phenomenon is called the Peltier effect, and the proportionality constant is known as the Peltier coefficient. As shown in **Figure 2.2**b, the Peltier coefficient can be expressed by the following formula:

$$\Pi=\frac{Q}{I} \tag{2-2}$$

Q is the heat absorption and emission rate at the node; I represents the current in the circuit. At the junction of the two conductors, there will be a temperature change, that is, the heat release temperature at one joint will increase, and the heat absorption temperature at the other joint will decrease.

2.1.3. *Thomson effect*

The above two effects focus on two different metals or conductors. Thomson creates the third effect named Thomson effect, which combined Seebeck and Peltier effect in 1855 (Thomson, 1851). That is a material that can achieve the convention between heat and electricity, as well as prove this effect in experimental results. As shown in **Figure 2.2**c, a current I flows through a uniform conductor was heated to form a temperature gradient $\Delta T=T_2-T_1$, the endothermic or exothermic rate should be calculated as below：

$$Q=\beta I\Delta T \tag{2-3}$$

β is the Thomson coefficient, with the unit V/K, the formula can be transferred to

$$\beta=\frac{Q}{I\Delta T} \tag{2-4}$$

Thomason coefficient is positive with the same direction of current and temperature gradient and comes with an endothermic behavior in a conductor. Whereas it is negative with the reverse current direction. The microscopic physical nature of the Thomson effect is the potential energy difference of carriers under different temperature gradients.

Also, Thomason deduced the relation between these three-effects, known as the Kelvin relation,

$$\mathrm{S}_{\mathrm{ab}}=\frac{\Pi_{\mathrm{ab}}}{\mathrm{T}} \tag{2-5}$$

$$\frac{dS_{ab}}{dT}=\frac{\beta_a-\beta_b}{T} \tag{2-6}$$

which has great significance for the study of thermoelectricity and has been proved correct by many experimental studies to date, including for metallic and semiconductor materials.

2.1.4. *Thermoelectric theory and device*

These three effects positioned the foundation of the thermoelectric theory, but did not mention the comprehensive theory about thermoelectric devices (TED), like power generation and refrigeration. Thirty years later, Altenkirch (in 1909) solved this problem, He raised the three key factors related to the thermoelectric performance, which is Seebeck coefficient, electrical conductivity, and thermal conductivity (Altenkirch, 1909, 1911). It points the way to thermoelectric research. With the development of semiconductor physics in the 1930s, the research on thermoelectric materials turned to higher Seebeck coefficient semiconductors (~100μV/K) which favorably improved thermoelectric performance than metals. This results in a series of studies on investigating good semiconductors to be utilized as thermoelectric materials. Consequently, some traditional thermoelectric materials with high thermoelectric properties have been reported. Including Bi_2Te_3, PbTe, and SiGe, which achieved a breakthrough in performance compared with early metal materials (Biswas et al., 2012; Hong, Chen, Yang, & Zou, 2016; Hong, Chen, & Zou, 2018; Hu et al., 2015; Zhu, Hu, Zhao, & He, 2016). These materials still have great research potential.

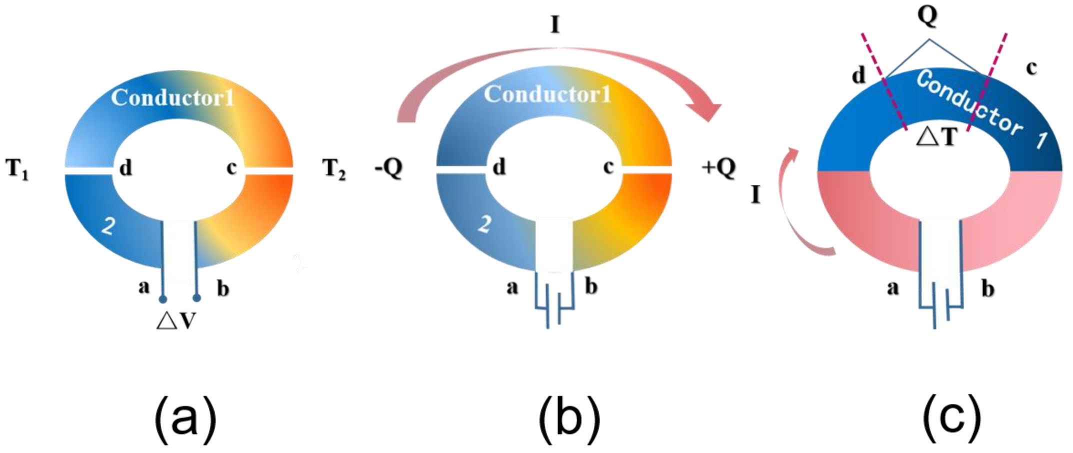

Figure 2.2. The schematic diagram of (a) the Seebeck effect, (b) the Peltier effect, and (c) the Thomson effect.

2.2. The evaluation parameters

2.2.1. Conversion efficiency

The maximum efficiency of power generation for TE material is defined by the below formula:

$$\eta = \left(\frac{T_h - T_c}{T_h}\right)\left[\frac{\sqrt{1+zT}-1}{\sqrt{1+zT}+\left(\frac{T_h}{T_c}\right)}\right] \tag{2-7}$$

In this equation, η is the efficiency of power generation, T_h is the hot side temperature, T_c is the cold side temperature, and zT represents the dimensionless figure of merit as mentioned in the formula. Among them,

$$\eta_{Carnot} = \left(\frac{T_h - T_c}{T_h}\right) \tag{2-8}$$

As we can see, the whole efficiency of power generation will be limited by the Carnot cycle, which depends on the temperature gradient between the hot and cold sides. Furthermore, the zT value is also determined η, so most of the research focuses on how to optimize the thermoelectric properties. **Figure 2.3** shows the efficiency comparison of thermoelectric materials and other energy-conversion technologies. So far, the power generation efficiency of thermoelectrics is lower than other sources because the highest zT value of thermoelectric is around 2. It is comparable with other sources when the zT value is improved up to 4.

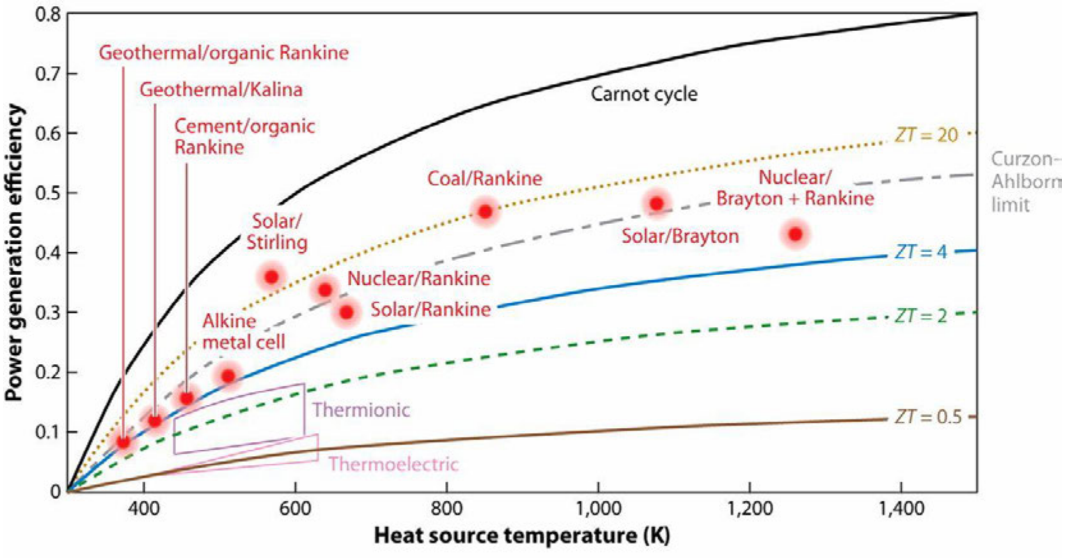

Figure 2.3. The efficiency comparison of thermoelectrics and other energy-conversion technologies as a function of the heat-source temperature (J. He & Tritt, 2017; Shakouri, 2011).

2.2.2. Figure of merit zT

In 1911, German scientist Altenkirch established a theoretical model to explore better thermoelectric materials and determined the relationship among the Seebeck coefficient, electrical conductivity, and thermal conductivity.

$$z=\frac{S^2\sigma}{\kappa_{tot}} \tag{2-9}$$

Thermoelectric conversion efficiency can be measured by a simple dimensionless parameter, *zT*.

$$zT=\frac{S^2\sigma}{\kappa_{tot}}T \tag{2-10}$$

Where S is the Seebeck coefficient (μV K^{-1}), σ is the electrical conductivity (S m^{-1}), κ_{tot} is the total thermal conductivity (W $m^{-1}K^{-1}$). According to Manha-Sofo theory, the Seebeck effect can be expressed as:

$$S=\frac{8\pi^2 k_B T}{3e^2 h}m*\left(\frac{\pi}{3n}\right)^{2/3} \tag{2-11}$$

$$\sigma=ne\mu \tag{2-12}$$

The product of the Seebeck coefficient and electrical conductivity named Power factor $PF=S^2\sigma$. The total thermal conductivity is consisted of electrical thermal conductivity and lattice thermal conductivity.

$$k_{total}=k_e+k_l \tag{2-13}$$

2.3. Thermoelectric materials development

There are three main types of thermoelectric materials classified by operation temperature in thermoelectric devices. The classical thermoelectric material Bi_2Te_3 has decent thermoelectric properties at room temperature and is extensively applied to thermoelectric materials, so-called cryogenic material. Bi_2Te_3 belongs to the R3m rhombohedral system, with a high pristine Seebeck coefficient and low thermal conductivity, the *zT* value of undoped samples is around 0.2. The thermoelectric performance could be improved by substituting, alloying, or using the solution method to synthesize nanoplates, the highest *zT* value reported so far is 1.56 at 300 K with nanostructured $Bi_{0.52}Sb_{1.48}Te_3$ (Hong et al., 2016; Wenjie Xie, Tang, Yan, Zhang, & Tritt, 2009). Bi_2Te_3 can be substituted with each other to prepare p-type and n-type thermoelectric materials (Hu et al., 2015). Another thermoelectric material, widely investigated since the 19th century, PbTe is essentially utilized in the mesothermal region (400 K-700 K). PbTe adopts the NaCl crystal structure, empty group of $Fm\bar{3}m$ with high-symmetry structure and stable chemical properties, as well as high melting point, thus PbTe based analogs are more suitable for middle temperature compared with Bi_2Te_3. Doping with other IV−VI chalcogenides such as SnTe, PbSe, GeTe by alloying can efficiently improve the property of PbTe. With the emerge of nanomaterials, solution preparation of nanomaterials and embedding of nanocrystals were used to increase the zT value by reducing thermal conductivity. K introduce in $PbTe_{0.7}S_{0.3}$ system enhanced zT values up to 2.2 at 923K which generates abundant nano precipitates to decrease the thermal conductivity (H. J. Wu et al., 2014). In addition, doping 2mol% Na into the PbTe-4mol%SrTe system processing with SPS decreases the thermal conductivity by scattering long-wave phonons with mesoscale nanostructures. Thus, the overall zT values are 2.1 at 800 K (Kim, Zhao, Kanatzidis, & & Seidman, 2017). Furthermore, there are other mid temperature thermoelectric materials have been studied over a few decades. Such as $CoSb_3$ skutterudites, Mg-based alloys, Zintl phase materials, SnTe and SnSe (Brown, 2006; Z.-G. Chen, Shi, Zhao, & Zou, 2018; Liu, Zhang, Li, & Zhao, 2007; Santhanam, 1981; G. Tan et al., 2015; Tang, Hanus, Chen, & Snyder, 2015; Q. Zhang et al., 2013; Zhao, 2016). Speaking of high-temperature applications, SiGe (Dismukes, Ekstrom, Steigmeier, Kudman, & Beers, 1964; Joshi, 2008; X. W. Wang et al., 2008) and half-Heusler materials (Fu et al., 2015; W. Xie et al., 2012) are the most advanced.

2.4. The fundamental characteristics of GeTe

2.4.1. Crystal structure

The phase diagram of binary Ge-Te is shown in **Figure 2.4**a (A. Schlieper, Y. Feutelai, S.G. Fries, B. Legendre, & Blachnik, 1999). Ge and Te elements with a composition close to 1:1 undergo a solid-state melting process to form a GeTe compound with a melting point of 993 K. GeTe has two stable phases: the high-temperature β-phase crystalize in cubic structure (C-GeTe, space group $Fm\bar{3}m$) and the low temperature α-phase with rhombohedral structure (R-GeTe, space group *R3m*). As can be seen form **Figure 2.4**b, the experiment XRD results show the indexed peak change from (024) and (220) of R-GeTe to (220) of C-GeTe at around 700 K (Levin et al., 2013). This phase change is caused by the thermal strain-induced displacement of Ge atoms (1/2, 1/2, 1/2) to (1/2-*x*, 1/2-*x*, 1/2-*x*), the Te atoms bending along the diagonal [111] direction.

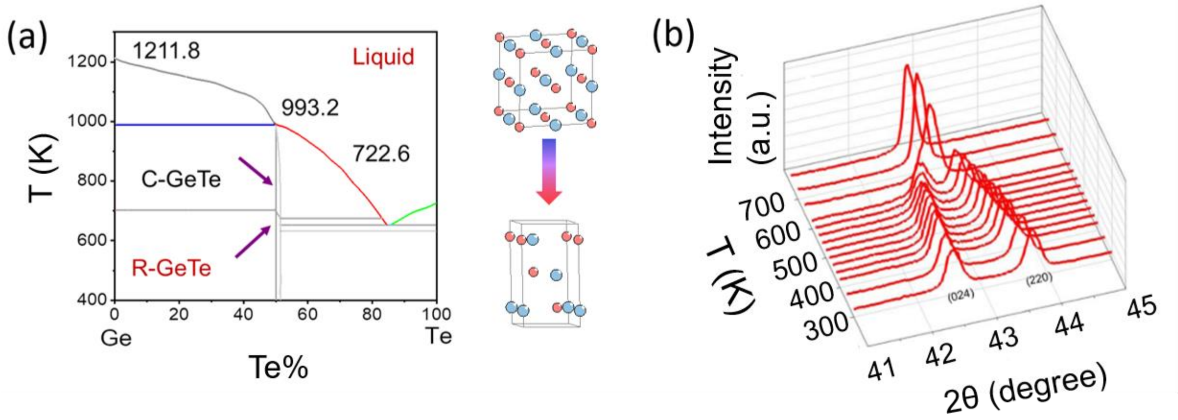

Figure 2.4. (a) The phase diagram of binary Ge-Te, (b) the XRD results with different temperatures of undoped GeTe (A. Schlieper et al., 1999; Levin et al., 2013).

2.4.2. Intrinsic Ge vacancies

GeTe is an intrinsic p-type thermoelectric material with a carrier concentration of $\sim10^{21}$ cm^{-3} at room temperature. This is due to the lowest formation energy of Ge vacancies as shown in **Figure 2.5** a-b. The loss of Ge may be caused by the thermal strain induced the displacement of Ge during the phase change from C-GeTe to R-GeTe. This Ge vacancy was also reported to contribute to the formation of a displacement channel to facilitate the rearrangement of Te atoms (Edwards et al., 2006). The important role of Ge vacancy is also found in Ge-Sb-Te ternary compounds (GST), which drive a metal-insulator transition (Christian Pauly et al., 2013;

W. Zhang et al., 2012). Ge vacancies concentration were reported between 8%-10% on the Ge sublattice (A. V. Kolobov, J. Tominaga, P. Fons, & Uruga, 2003). Refer to J.E. Boschker's estimation in perfect crystal, a simple cubic 4×4 GeTe unit cell with parameter of 6Å contains 18.4×10^{21} unit cells, 8% Ge vacancies generated from this Ge sublattice site, the Ge vacancies theoretically can contribute a carrier concentration of $\sim3\times10^{21}$ cm^{-3} (Boschker, Wang, & Calarco, 2017). However, the experimental carrier concentration is smaller than this estimated one. The experimental results show the composition of Ge vacancy is around 1%-3% **Figure 2.5**c (Hong & Chen, 2022). This result is reasonable considering the possible defects can trap or annihilate the carriers.

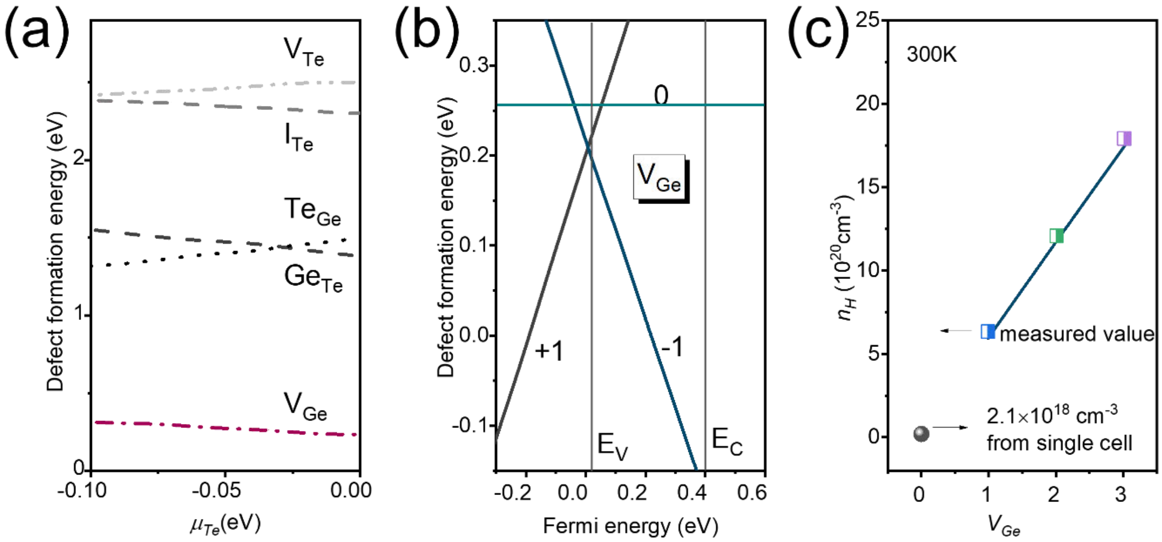

Figure 2.5. Defect formation energy of pristine GeTe as a function of the chemical potential of (a) Te, and (b) fermi level, and (c) the carrier concentration as a function of Ge vacancy content (Hong & Chen, 2022; B. Huang & Robertson, 2012).

2.4.3. Electrical band structure

The electronic band structure and corresponding DOS of R-GeTe and C-GeTe are displayed in **Figure 2.6**a-b. R-GeTe is an indirect semiconductor with a band gap of 0.62 eV calculated from the maximum valence band edge at the Σ point (VB$_{\Sigma}$) to the minimum conduction band edge at the L point (CB$_{L}$). Ge 4p^{2} and Te 4p^{2} dominated the VB edge and CB edge, respectively. As GeTe is a p-type semiconductor with intrinsic hole concentration, element doping at the Ge site can achieve fermi level tuning and optimize carrier concentration (n_p). C-GeTe has a direct band gap of 0.23 eV from the VB edge (VB$_{L}$) to CB edge (CB$_{L}$) at the L point. The maximum VB edge switch from the Σ point to the L point shows increased symmetry of C-GeTe. This enables GeTe to have multi freedom manipulation degree to achieve high band degeneracy.

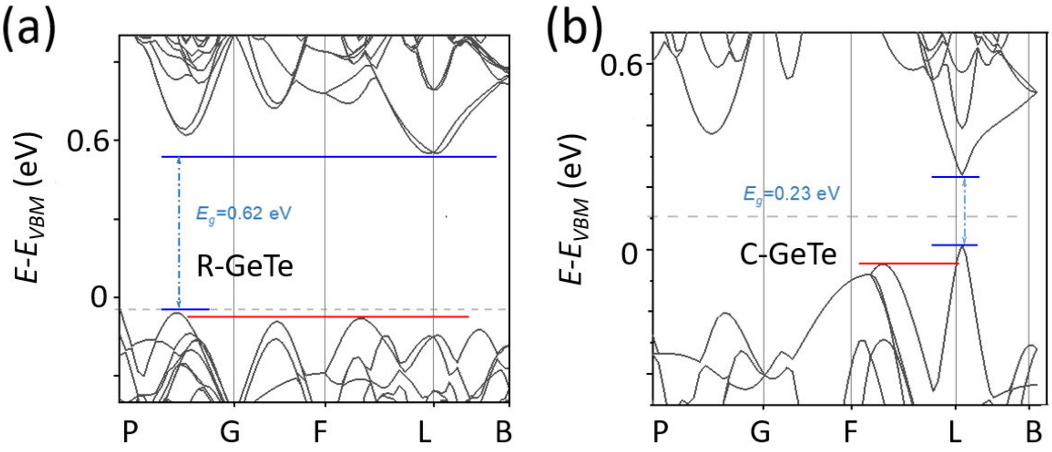

Figure 2.6. Band structures of (a) rhombohedral structured GeTe, and (b) cubic structured GeTe.

2.4.4. Thermoelectric performance of pristine GeTe

GeTe has outstanding thermoelectric performance at both low and mid temperatures and has attracted increased attention (Hong, Zou, & Chen, 2019b; Xinyue Zhang et al., 2020). GeTe crystalizes into the rhombohedral structure (R-GeTe, space group $R3m$) at low temperatures and transits into the cubic structure (C-GeTe, space group $Fm\bar{3}m$) at 700 K due to the displacement of Ge atoms induced by thermal strain (Chatterji, Kumar, & Wdowik, 2015; Hong et al., 2019b). Pristine GeTe is a highly degenerate p-type semiconductor with a high hole concentration (n_p~10^{21} cm^{-3}) due to the Ge vacancies (S. Perumal, S. Roychowdhury, & K. Biswas, 2016) . This is caused by the low formation energy of Ge vacancy in the GeTe system (Damon, Lubell, & Mazelsky, 1967). The high n_p induces a large σ and in turn, a small S. Therefore, tuning n_p to optimization level (~5×10^{19} cm^{-3}) should be the key to achieving high $S^2\sigma$ (Shuai, Sun, Tan, & Mori, 2020; L. Yue et al., 2019). On the other hand, undoped pristine GeTe has a high κ_l (~3.2 $W\cdot m^{-1}\cdot K^{-1}$at room temperature), which is far above the minimum κ_l (κ_{min} of ~0.3 $W\cdot m^{-1}\cdot K^{-1}$). These factors have limited the peak zT value of pristine GeTe to ~0.8 at 720 K (S. Perumal et al., 2016).

2.5. Strategies of thermoelectric performance optimization on GeTe

2.5.1. Carrier concentration engineering

The high zT values of good thermoelectric materials need to have large S and σ, and also a low κ_{tot} (κ_{ele}+κ_{lat}). The dilemma of thermoelectric parameter regulation stems from the coupling effect between the electrical property parameter and the thermal property parameter. The schematic diagram displayed in **Figure 2.7**a shows the n_H dependent thermoelectric parameters including S, σ, $S^2\sigma$, κ_{tot}, κ_{ele}, zT. S and σ cannot be optimized at the same time, so there is an optimal power factor as a function of n_H. In addition, σ also has a coupling relationship with the thermal performance parameter κ_{ele}, due to higher σ will lead to higher κ_{ele}, which is contrary to the requirement of lower thermal conductivity. Therefore, peak zT values correspond to slightly different optimal n_H values. Therefore, the regulation of carrier concentration is the most intuitive and effective method to optimize thermoelectric performance.

According to Ioffe's first empirical attempt in doped semiconductors, the carrier concentration "sweet spot" of good thermoelectrics is n_H between 10^{18}–10^{20} cm^{-3}, corresponding to degenerate semiconductors or semimetals. GeTe has an intrinsically high hole concentration n_p of ~10^{21} cm^{-3} due to easily formed Ge vacancies. This results in a zT value of ~1 in pristine GeTe due to high κ_{ele} and relatively low $S^2\sigma$. The theoretically optimized n_p of GeTe based materials is 5×10^{19} cm^{-3}. Thus, adjusting n_p to this "sweet spot" is generally used to effectively regulate the thermoelectric parameters to increase zT value. There are many methods to reduce n_p in the GeTe system, including experiment-based chemical composition regulation, self-doping, aliovalent element doping, and alloying.

Since the composition of the GeTe compound itself is not strictly 1:1, defects are always inevitable in the process of compound synthesis. Therefore, the carrier concentration can be variable with different experiment conditions and also easily tuned by a Ge-rich environment. These are effective methods to adjust the carrier concentration without introducing a third element. Figure **2.7**b shows the n_p optimization as a function of experimental-based regulation, excess Ge doping, and other elemental doping. As shown in **Figure 2.7**b, K.S. Bayikadi reported an in-situ vacancy control route using a post annealing process. With post annealing temperatures rising from 800 to 900 ℃, the composition of Ge and Te is close to 1:1 with reduced Ge vacancies. The corresponded n_p decreases from 9.01×10^{20} to 7.33×10^{20} cm^{-3}. zT value increases from 0.7 to 1.37 at 773 K (Bayikadi et al., 2019). $Ge_{1+x}Te$ (x=-0.01-0.04) were designed to investigate excess Ge doping to inhibit the generation of Ge vacancy (Dong et al., 2019). This can decrease n_p from 8×10^{20} to 3×10^{20} cm^{-3} due to the suppression of Ge vacancies. Together with increased mobility due to weakened carrier scattering, the electrical properties of $Ge_{1+x}Te$ were pushed higher. The zT values can be enhanced up to 1.6. Element doping/alloying can reduce n_p by substituting aliovalent elements or introducing point defects. Srinivasan *et al.* (Srinivasan et al., 2019a) optimized n_p to 6.35×10^{20} cm^{-3} with the composition $Ge_{0.93}Ga_{0.07}Te$. Shuai *et al.* (Shuai et al., 2020) reported that transition metal Cr doping in GeTe can reduce the n_p to 3.82×10^{20} cm^{-3} by decreasing the Ge vacancy formation energy. Liu *et al.* (Z. Liu et al., 2020) observed that the n_p can be decreased from 8.63×10^{20} cm^{-3} of pristine GeTe to 2.09×10^{20} cm^{-3} of $Ge_{0.94}Sc_{0.06}Te$ by Sc doping, leading to a significantly increased $S^2\sigma$ from

10.4 μW·cm^{-1}·K^{-2} to 23.3 μW·cm^{-1}·K^{-2} at room temperature. Co-doping or alloying of two or more elements or compounds can further reduce n_p. Bu et al. [28] reported that alloying GeTe with 1.5 mol.% Cu_2Te, 2 mol.% BiTe, and 8 mol.% PbTe can tune the n_p of GeTe-based thermoelectric materials close to the optimum level of ~5×10^{19} cm^{-3}, leading to a high zT of 2.4 at 650 K (Bu et al., 2019). However, point defects induced by doping can decrease carrier mobility (μ_p) and in turn, deteriorate σ. Thus, most peak zT values are obtained within the doping range of 0.01 to 0.03 (Nshimyimana et al., 2020; Srinivasan et al., 2019a). Owing to the similar electronegativity between Sb/Bi and Ge, Sb and Bi are widely used as co-doping elements to optimize n_p (Hong et al., 2020; Luo Yue et al., 2020).

The n_p dependent S of Sb and Bi doped GeTe was plotted in **Figure 2.7**c, the optimal n_p of GeTe is around 2×10^{20} cm^{-3} in Sb/ Bi alloyed GeTe system. With the above optimization strategies of carrier concentration, the zT value can be improved due to the improved $S^2\sigma$ and also largely decreased κ_{ele}.

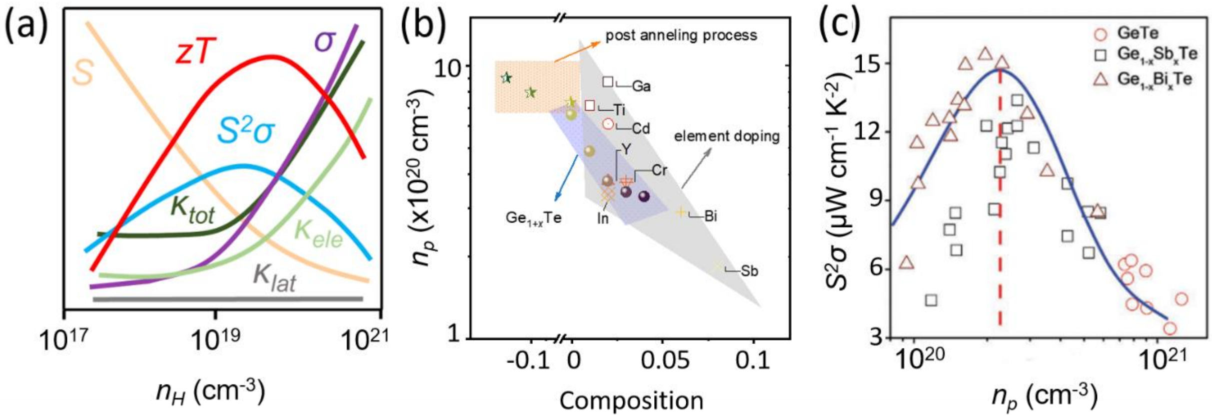

Figure 2.7. (a) The schematic diagram of thermoelectric parameters as a function of carrier concentration, (b) carrier concentration engineering of different methods, and (c) the $S^2\sigma$ as a function of n_p of Bi/Sb doped GeTe (Bayikadi et al., 2019; Dong et al., 2019; Gao et al., 2021; M. Hong, Y. Wang, et al., 2018; W. D. Liu et al., 2020; Suresh Perumal, Subhajit Roychowdhury, & Kanishka Biswas, 2016; Perunnal, Roychowdhury, Negi, Datta, & Biswas, 2015; Shuai et al., 2020; Shuai et al., 2019; Srinivasan et al., 2019b).

2.5.2. Band engineering

Band engineering as an effective way to regulate electrical transport properties has been investigated by many researchers. As shown in **Figure 2.8**a-b, band engineering can achieve electrical transport properties by increasing band convergence $N_{V,}$ introducing resonant energy, band flatten. For the IV–VI compounds PbTe and SnTe, The Group III elements Ga, In, and Tl were reported to have a resonant level effect on IV–VI compounds due to the s-orbital energy level of doping elements are between s-orbital energy level of cation (Pb/Sn) and anion (Te) elements (X. Tan et al., 2018). The schematic diagram density of state of induce in resonant states is shown in **Figure 2.8**a. This is also suitable for IV–VI compound GeTe. As shown in **Figure 2.8**c, L. Wu examined the possible distortions of the electronic density of states (DOS) near the E_F of group IIIA elements (Ga, In, Tl) in GeTe. Among them, In shows a large enhancement compared with Ga, Tl. Thus, the increased S due to increased m^*(**Figure 2.8**d) together with the suppressed thermal conductivity, leads to a reasonably high zT of 1.3 at 628K of $In_{0.02}Ge_{0.98}Te$ (L. Wu et al., 2017). In co-doping with Sb can also contribute to DOS distortion near the E_F and result in increased S in turn enhancing the thermoelectric performance (M. Hong, Z. G. Chen, et al., 2018). This is similar to the doping of other IV–VI chalcogenides like Tl-doped PbTe (Heremans, 2008), and In-doped SnTe (Q. Zhang et al., 2013). In addition, B. Srinivasan reported that Ga doping induces in an resonant energy level and increase the effective mass m^*(Srinivasan et al., 2019b), as shown in **Figure 2.8**e.

The Group V elements As/Sb/Bi tend to have weak band convergence effects (X. Tan et al., 2018). The Sb/Pb/Bi doped GeTe is consistent with the theoretical situation of the carrier concentration variation. This indicates the effective mass may not change a lot (Hong, Zou, & Chen, 2019a). **Figure 2.8**b shows that the band structure does not change obviously compared to undoped GeTe. The experiment results can also clarify this. Cd doping in GeTe can decrease ΔE of VBs by inducing an impurity band. This impurity energy level is caused by the Cd_5s^2 orbitals (M. Hong, Y. Wang, et al., 2018). Zn can also induce a strong band convergence effect in GeTe based materials and cause increased S as displayed in **Figure 2.8**f. D.K. Bhat, mentioned that Zn doping in GeTe can also induce a resonant energy level.

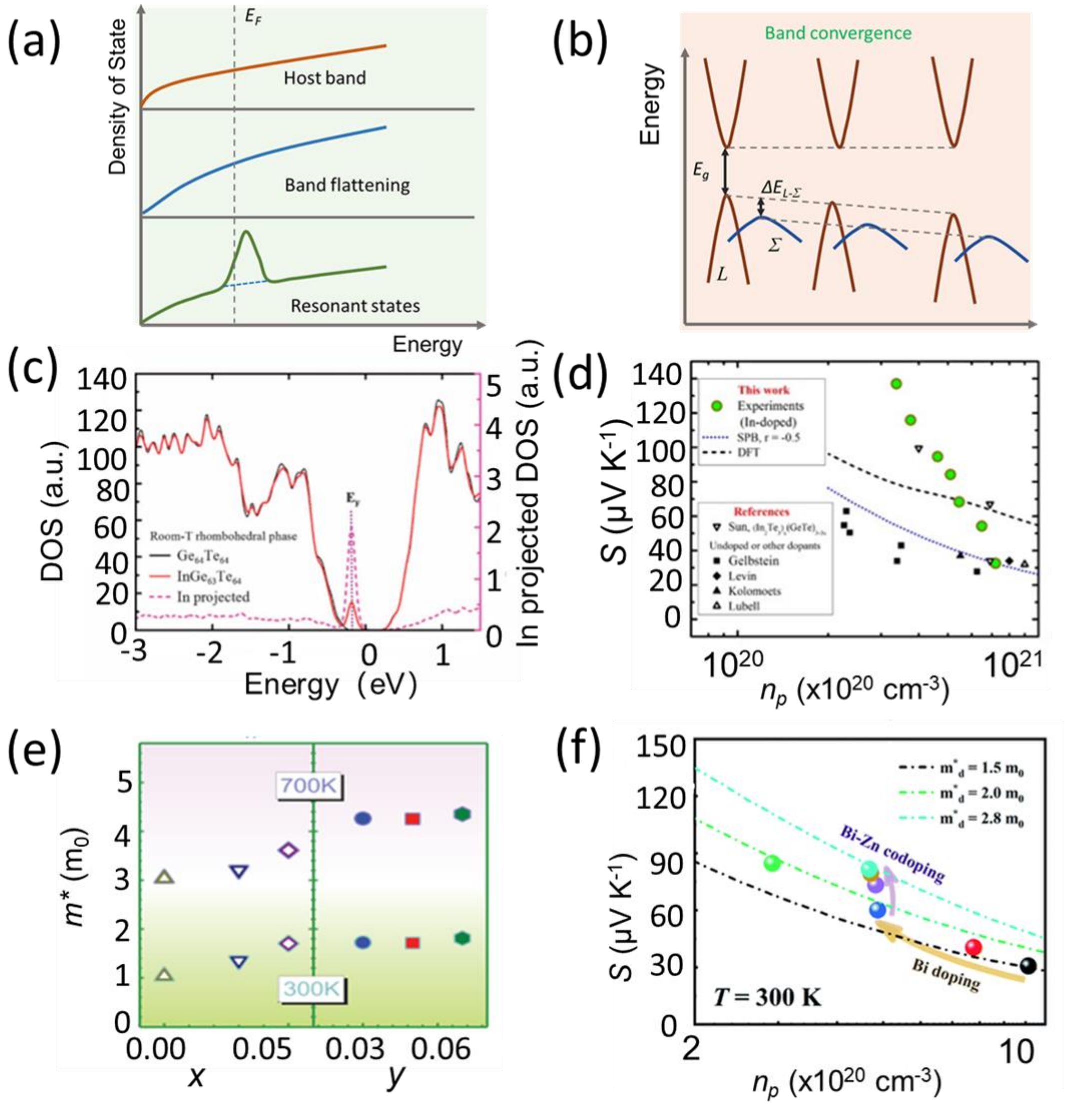

Figure 2.8. (a) The density of state diagram of band flattens and the resonant states, (b) the schematic diagram of band convergence, (c) the DOS of In doped GeTe, (d) the *S* of In doped GeTe as a function of carrier concentration n_p, (e) the effect mass $m^*$of Ga doped GeTe changes with doping content, and (f) S as a function of n_p of Zn and Bi co-doped GeTe

(Bhat & Shenoy, 2020; M. Hong, Z. G. Chen, et al., 2018; Srinivasan et al., 2019b; L. Wu et al., 2017).

2.5.3. Phonon scattering engineering

Unlike the coupling effect of other evaluation parameters of thermoelectric performance, κ_{lat} can be individually adjusted to optimize thermoelectric performance. Many strategies have been used to decrease κ_{lat} (J. Q. Li et al., 2019; Roychowdhury, Samanta, Perumal, & Biswas, 2018; Samanta, Roychowdhury, Ghatak, Perumal, & Biswas, 2017; Siegert et al., 2015; H. Tan et al., 2019; D. Wu, Xie, Xu, & He, 2019). Such as, inducing diverse defects at different levels including point defects which affect high-frequency phonons, dislocations, and grain boundaries, mainly scattering low-frequency phonons. These crystal defects can accelerate the scattering rates of phonon waves, leading to the reduction of κ_{lat} (Z. Chen, Zhang, & Pei, 2018). A low κ_{lat} of 1.1 Wm^{-1} K^{-1} was achieved in $Ge_{0.90}Bi_{0.10}Te$ due to collective phonon scattering from mesostructured grain boundaries, nano-structured precipitates, nano-structured defect layers, and solid solution point defects. In addition, the nano precipitate, as one of the low-frequency phonon scattering factors has an important impact on GeTe. The small number of intrinsic nanostructures in $CoGe_2$ synthesis into uniformity GST ($(GeTe)_nSb_2Te_3$) systems as additional precipitates can decrease the thermal conductivity. Therefore, the *zT* values were further enhanced up to 1.9 in the composition of $(CoGe_2)_{0.2}(GeTe)_{17}Sb_2Te_3$ (Fahrnbauer, Souchay, Wagner, & Oeckler, 2015).

In addition, alloying with other group compounds can effectively work on lattice thermal conductivity by producing the herringbone structure, which called structural modulation. Alloying with $AgSbTe_2$/$AgSbSe_2$ /$AgBiSe_2$ systems can induce strong alloying scattering to reduce the thermal conductivity (J. R. Salvador, Yang, Shi, Wang, & Wereszczak, 2009; Samanta et al., 2017). As one of the alternatives, In_2Te_3 alloyed GeTe to decrease the lattice thermal conductivity from 1.8 Wm^{-1} K^{-1} to 0.9 W m^{-1}

K^{-1} at 323 K, the 0.05% doped sample shows lower lattice thermal conductivity than the pristine one during the whole temperature area. This decline results from the strong phonon scattering caused by fluctuations both in mass and strain (H. Sun, Lu, Chi, Morelli, & Uher, 2014). The presence of PbTe precipitates strongly influences the thermoelectric properties as it increases the Seebeck coefficient and decreases the thermal conductivity, which collectively gives rise to a maximum *zT* of 0.81 for the composition of $(GeTe)_{0.82}(PbTe)_{0.18}$ at 673 K.

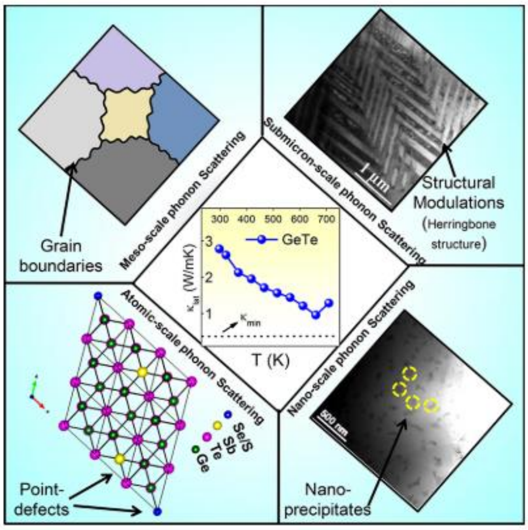

Figure 2.8. (a) Illustration of the different phonon scattering mechanisms (Roychowdhury et al., 2018).

2.5.4. Decoupling electrical and thermal transport properties

In the above, the strategies including carrier concentration engineering, band engineering, and phonon scattering engineering that can effectively optimize the *zT* values are overviewed. However, the element doping method that is used to achieve these strategies can also cause increased coherence of thermal and electrical properties when the doping scale increases for both materials and numbers. This is due to the increased doping scale, including dopant numbers and doping level, which will cause a large energy barrier and increased carrier scattering due to crystal mismatch. Or the electronic bands misalignment. This will affect the carrier mobility and power factor. Thus, decoupling the electric and thermal transport properties to ensure a high carrier mobility becomes an important role in breaking this trade-off between electrical and thermal transport properties.

Li, N. *etc*. (N. Li et al., 2021) claim the importance of electronegativity in thermoelectric GeTe-based solid solutions and thus provides valuable guidance for designing novel thermoelectric materials. Yu, Y., et al reported the quantum gaps defined by a class of planar defects characterized by nano-potential well can decouple the carrier and phonon transport by selectively scattering phonons while allowing to pass effectively as shown in **Figure 2.9**. The other effective method is that induced in Cu or Cu based alloys can effectively enhance or compensate for the loss of carrier mobility (N. Li et al., 2021; Yin et al., 2021). This can raise a higher *zT* value compare with other elements. Li, N. reported that the Cu based GeTe–I–V–VI$_2$ solid solutions $(GeTe)_{0.92}(CuSbTe_2)_{0.08}$ have achieved *zT* of 1.30 and 1.58 at 773 K higher than Na based GeTe–I–V–VI$_2$ alloys (N. Li et al., 2021).

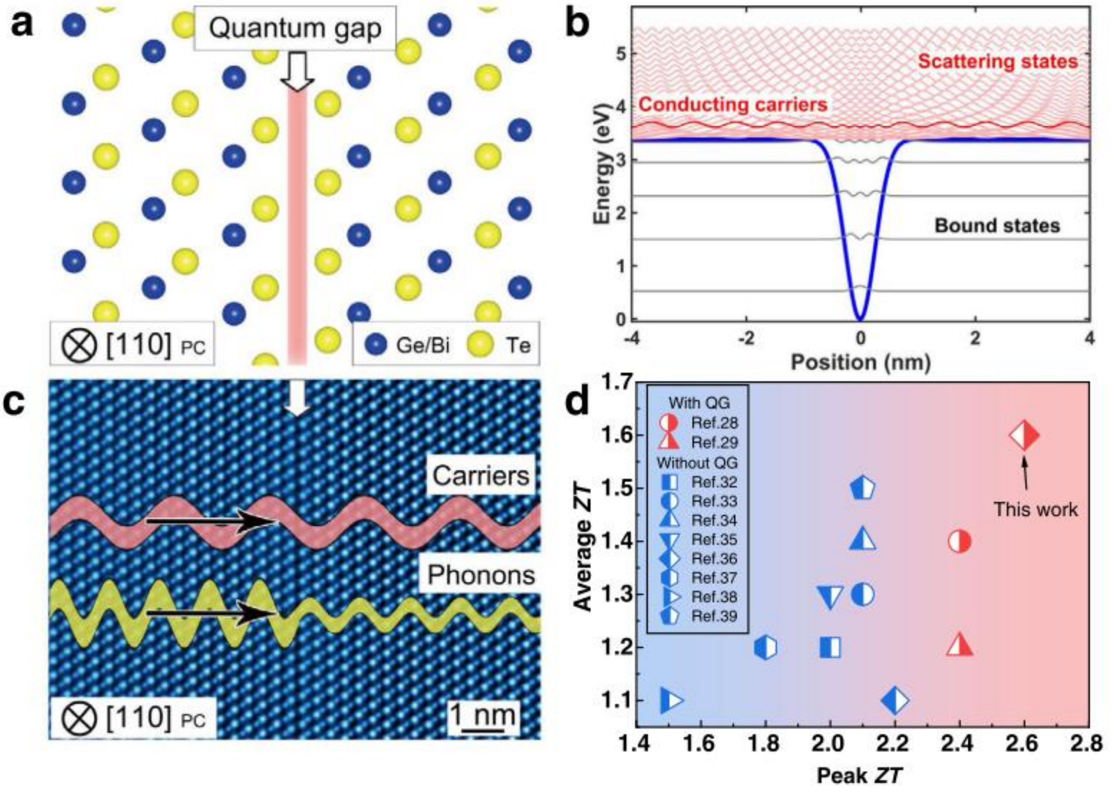

Figure 2.9. Quantum gap effect of GeTe-based thermoelectric (Yu et al., 2022).

2.6. Summary and Research Gap

In summary, we have reviewed the history of thermoelectric effects, the evaluation method of thermoelectric materials' performance, and the power generation. The figure of merit is mainly used to assess the properties of materials, and when combined with the control of temperature differences, it can determine the efficiency of generation. After that, we conclude the statues of some classic thermoelectric materials studied in the last decades. PbTe, as the extensively investigated material, shows a substantial position in the medium temperature application. GeTe, as another IV-VI chalcogenide, expresses the advanced performance recently eased by the limited utilization of toxic Pb. In addition, we detailed the crystal structure, band structure, and thermoelectric properties of GeTe to analyze the microstructure characteristics of the material itself.

GeTe crystallize in a rhombohedral structure at low temperatures and turns into a cubic structure when the temperature rises to 700K. Due to greater band degeneration and better intrinsic phono-phonon interaction, the high-temperature rack salt structure of GeTe results in a higher *zT*. As a result, the additional phase transition temperature reduction supports the *zT* improvement over a large range of temperatures. Due to the easily formed cation vacancy, pristine GeTe with high hole concentration exhibits a lower Seebeck coefficient, high electrical conductivity, as well as the higher electrical thermal conductivity, which leads to a lower *zT* value. Consequently, the straightforward way to optimize the performance of GeTe is to decrease the hole density. By increasing annealing temperature, or doping with aliovalent elements like Sb, Bi, can achieve the reduction of carrier concentration effectively. Thus, the power factor was improved result from the decreased electrical conductivity and the increment of

Seebeck coefficient. In addition, band engineering through the local distortion of the DOS and valence-band alignment leads to high *zT*. Lattice thermal conductivity reduction has been achieved by strengthening point defect scattering, inducing multi-scale defects. Even if noteworthy efforts have been made for the last few decades to boost the GeTe performance of materials, progress in high-performance GeTe research remains quite slow. In particular, the following research gaps have yet to be addressed:

1) Element doping, as one of the most efficient methods, can regulate both electrical and thermal transport properties. However, the rare earth elements doping in the GeTe system haven't been clarified. Considering the advantages of rare earth elements including large mass and radius which can favor point defect scattering, with high valence (+2, +3, +4) than Ge which can provide electron in GeTe system, local magnetic moment of most rare earth elements may contribute to Seebeck coefficient. The research on rare earth elements doping effect of GeTe is meaningful.

2) The doping limit or solubility of element substitution on GeTe system has been neglected. Carrier concentration tuning and point defect scattering effects rely on the doping content of elements. Thus, increasing solubility may can further modify the thermoelectric performance by strengthening the effect of these strategies.

3) TAGS-85, as one of the important materials, has been widely studied and have achieved good results. For now, the *zT* value of GeTe-based materials is higher than 2.5. Further tuning of TAGS-85 may can lead to new breakthrough that can be used in devices.

4) The *zT* value of GeTe has been increased to higher than 2.7. This is enough for the device application. However, the device design for GeTe-based materials is still on the way to be researched. Thus, the device design investigation related parameters and also the suitable modules are important for future directions.

CHAPTER 3: METHODOLOGIES

The research methodologies used in this project are introduced in this chapter. We summarize the experimental methods and data processing approach related to this research project. It includes a detailed introduction to the preparation method of GeTe-based thermoelectric materials, the characterization of crystal structure and microstructure, as well as thermoelectric performance measurement. The methodology flow chart is shown in Figure 3.1.

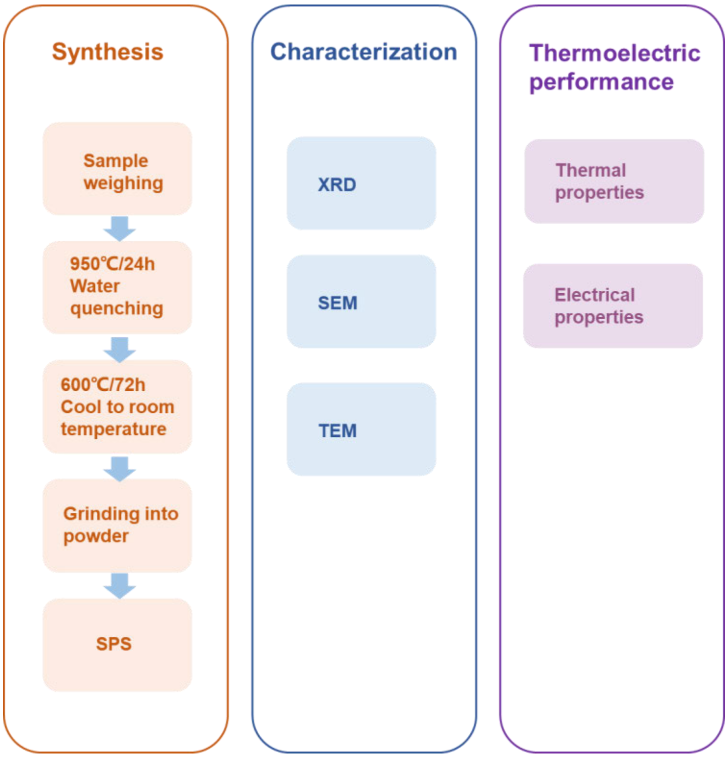

Figure 3.1. Methodology flow chart.

3.1. Synthesis

3.1.1. Preparation of powder samples by melting method

With the continuous development of science and technology, there are various approaches for preparing thermoelectric materials. Conventional thermoelectric materials can be synthesized by melting, mechanical synthesis such as ball milling, hydrothermal, microwave, etc. Among them, the melting method is extensively used to prepare large-scale inorganic thermoelectric materials. Not only due to its advantages of feasibility and low cost, which can easily be synthesized, but also because the thermoelectric materials obtained by the melting method have higher performance. Thus, considering the advantages mentioned above and the feasibility of existing equipment in the laboratory, we decide to use the melting method to fabricate our GeTe system materials.

In this project, we use the muffle furnace to complete experimental synthesis. The particularized procedure for GeTe-based materials synthesis is shown in **Figure 3.2**, the details are: The high purity elemental materials were balanced according to the molar ratio. Then put all these pieces into a quartz tube and sealed with enough vacuum. The starting materials in a vacuum quartz tube into the muffle furnace, sintering for 24 hours at 950 °C, followed by water quenching. Then annealing for 72 hours with temperature 600 °C followed by water-quenching. Finally, carefully smash the quartz tube and take the resulting ingots out, then grind them into powder with agate mortar, and keep them in the properly labeled sample tube for future use.

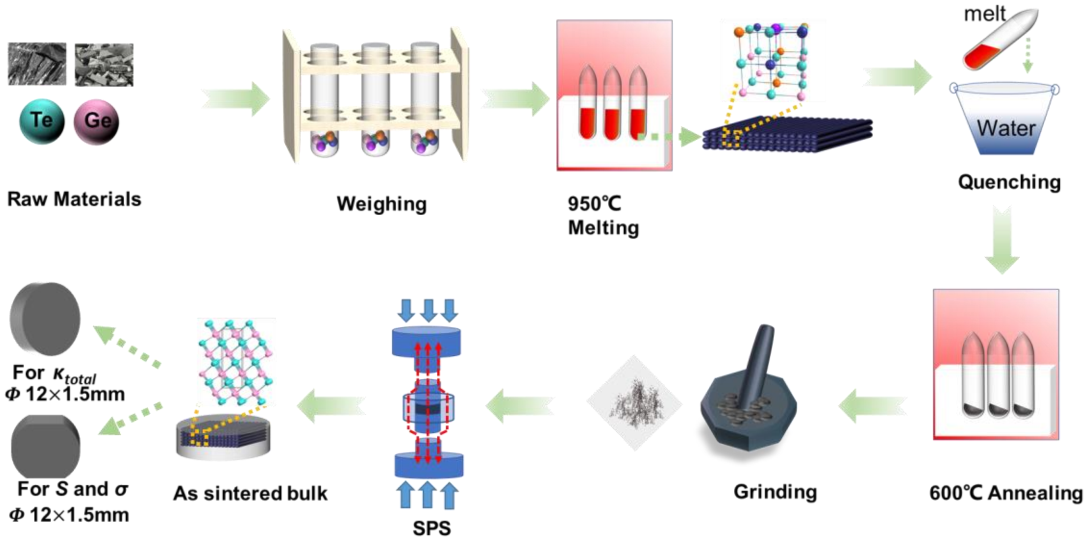

Figure 3.2. The synthesis process of GeTe-based materials.

3.1.2. Preparation of bulk samples by SPS

The resulting samples from powder synthesis need to be compressed into bulk samples for characterization and thermoelectric performance assessment. Herein, we use the spark plasma sintering (SPS), also known as pulsed electric current sintering (PECS) method, to prepare disk materials. The principle of SPS is to obtain high-density block samples quickly by using current heating and pressure assistance. The SPS system configuration is shown in **Figure 3.3**a. It consists of a graphite die that holds the powder, a fixed electrode on the top, and a moving electrode on the bottom where the mechanical load is put, and the current goes through. The SPS system uses pulsed direct current (DC) as the power supply to heat samples which directly pass through the graphite die and the resulting powders to sintering temperature. This heating method favors it to get high density (>90% theoretical density) circular at a lower sintering temperature compared to conventional sintering techniques (Nisar, Zhang, Boesl, & Agarwal, 2021). In addition, the rapid sintering process resists grain size growth which is beneficial for electrical and thermal transport performance.

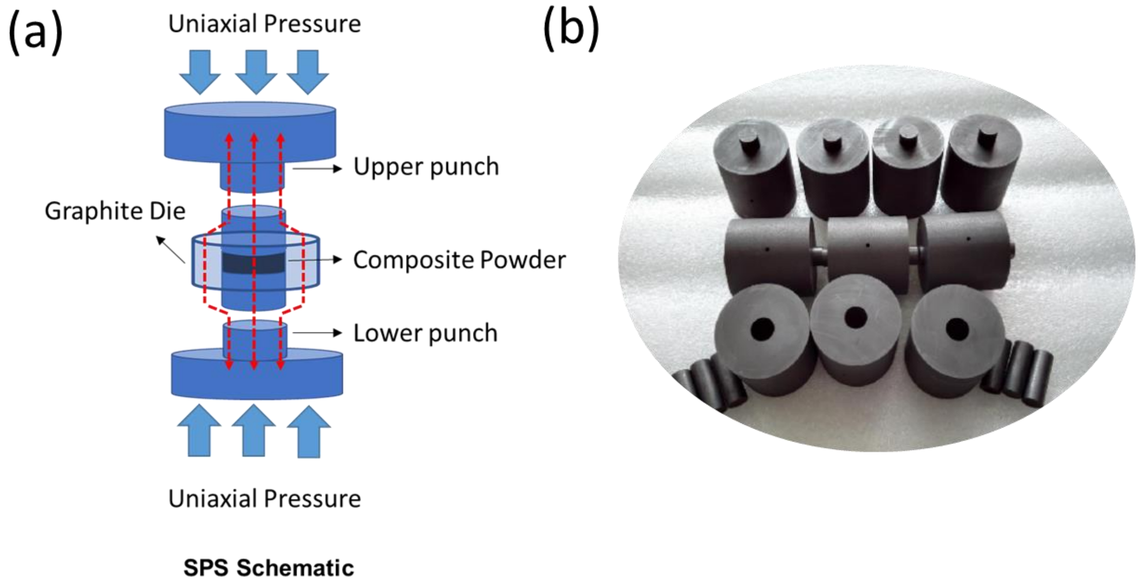

Figure 3.3. (a) SPS system configuration, (b) the graphite dies.

In this experiment, the high strength graphite die set was used to hold the sample powders. As shown in **Figure 3.3b**, the graphite die diameter was 12.5mm or 10mm with 35mm height, and there is a round hole in the middle of the die that is used to sense the inner temperature by inserting a thermocouple. Two graphite punches have a size of Φ 12mm×5mm to keep the powder in the graphite die.

3.2. Characterization

In this part, X-ray diffraction (XRD) is used to characterize the phase structure and purity of prepared materials. The composition of the resulting bulk is determined by EDS analysis. In addition, the scanning electron microscope (SEM) and transmission electron microscope (TEM) are performed to examine the microstructure information. The detailed analysis of these characterization methods is listed below.

3.2.1. X-Ray Diffraction (XRD)

X-Ray diffraction (XRD), as a fundamental technology that can determine the crystal structure information including atomic and molecular structure, as well as the cell parameters is widely used in TE materials analysis. During my research, the phase structure and purity of synthesized materials were indexed by XRD.

The schematic diagram of the principle of XRD based on the Bragg's law is displayed in **Figure 3.4**a. The corresponding equation is

$$2d\sin\theta=n\lambda \tag{3-1}$$

where d is the inter-planar distance, θ is the incident angle, λ is the wavelength of an X-ray and n is an arbitrary integer. The X-ray can be considered as electromagnetic wave generated by striking a metal target with a high energy electron beam. Then the diffraction pattern can be generated when X-rays interact with periodic atomic structures.

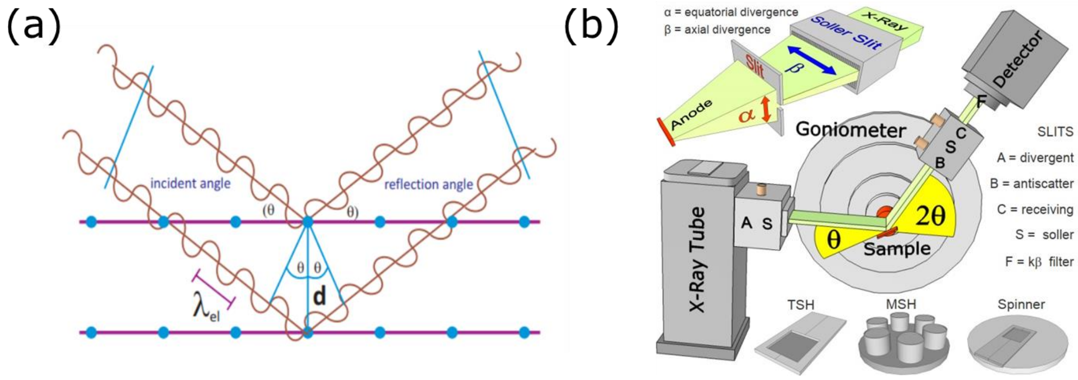

Figure 3.4. (a) The principle of XRD, (b) the schematic configuration of XRD instrument (https://letstalkacademy.com/x-ray-diffraction/, https://hust.com.vn/what-is-x-ray-diffraction-xrd.html).

3.2.2. Scanning Electron Microscopy (SEM)

The scanning electron microscope (SEM) is a powerful tool to characterize the morphologies of TE materials. In SEM, the surface of the sample is scanned by a focused electron beam to generate signals that contribute to the formation of the image. As shown in **Figure 3.5**a, the high-energy electrons generated from the incident electron beams hit the sample, the signals are formed include secondary electrons (SE), backscattered electrons (BSE), energetic dispersive characteristic X-ray (EDS). Among them, SE and BSE are commonly applied for imaging samples, where SE is used for showing the morphology and topography of samples, and BSE is used for illustrating the contrasts in composition in multiphase samples. The field-emission scanning electron microscope (FE-SEM, JSM-7001F, JEOL, Japan) was applied to explore the microstructures and composition of the resulting disks. The schematic configuration of SEM is displayed in **Figure 3.5**b.

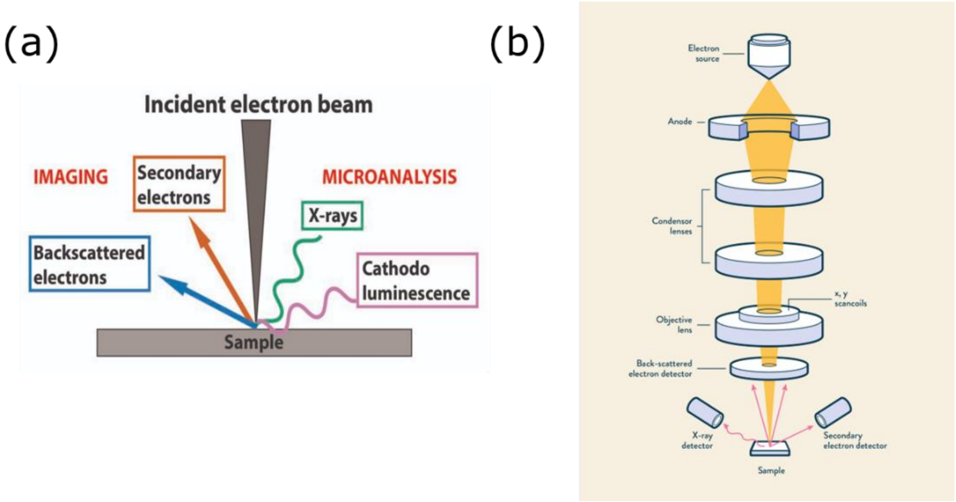

Figure 3.5. (a) The principle of electronic signals released from sample interaction regions in SEM, (b) the schematic configuration of the SEM microscope (https://emil.sites.unlv.edu/the-applications-of-epma-and-sem/, https://www.technologynetworks.com/analysis/articles/sem-vs-tem 331262).

3.2.3. High-resolution transmission electron microscope (TEM)

The transmission electron microscopy (TEM) technique is mainly used to obtain high-resolution images when the electrons interact with samples as the beam transmits through the specimen. As presented in **Figure 3.6**a, the accelerated electron beam is emitted from a filament and then modulated by lenses with respect to the spot size and brightness. The convergence angle and the intensity of the electron beam can therefore be adjusted by the condenser apertures. The signals, received from electron beam hitting samples, are selected and magnified by well--aligned lens system and presented by camera system. There are mainly two types of amplitude contrast, i.e., the mass-thickness contrast and the diffraction contrast, where the former is generated by the different scattering angle of heavy or light area, while the latter refers to different Bragg condition by different crystallography. The schematic configuration of TEM is shown in **Figure 3.6**b. The cystography information of GeTe based materials were characterized by the high-resolution transmission electron microscope (HR-TEM, Tacna F20, Philips, United States).

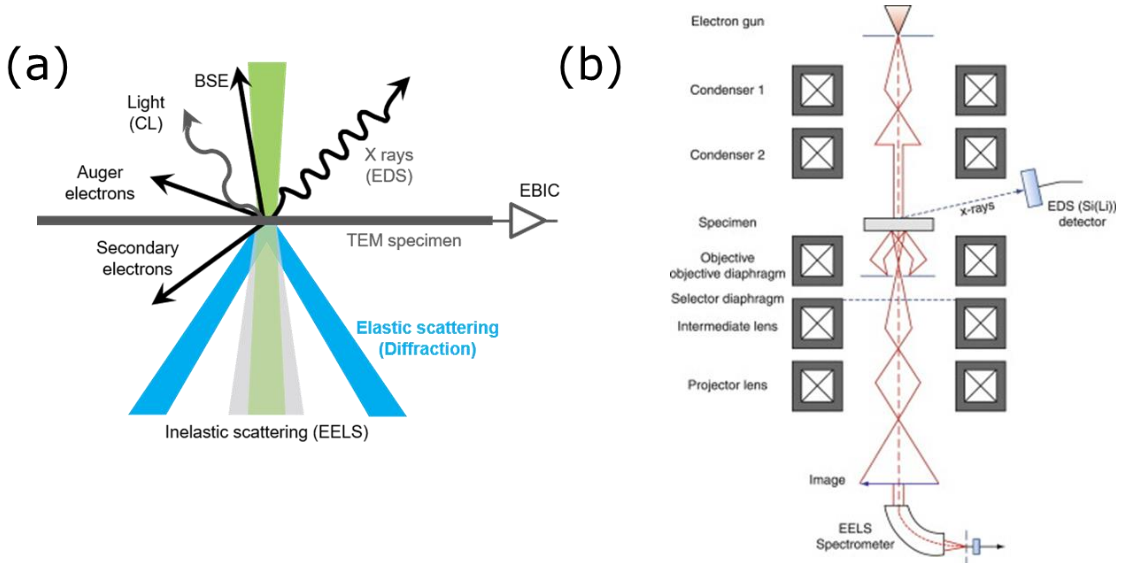

Figure 3.6. (a) The principle diagram of the formed signals in TEM imaging, (b) the schematic configuration of TEM (https://www.gatan.com/techniques/4d-stem, https://www.sciencedirect.com/topics/physics-and astronomy/transmission-electron-microscopy).

3.3. Thermoelectrical Properties

As we have known, the quality of thermoelectric materials depends on their thermoelectric figure of merit zT which is determined by Seebeck coefficient (S), electrical conductivity (σ) and thermal conductivity (κ_{tot}). In this section, the experimental techniques for the above parameters will be introduced in detail. We will outline the principle of the ZEM-3, ULVAC which simultaneously measures the S and σ, the thermal diffusivity (D) measured by laser flash method (LFA 457, NETZSCH), the Hall system which can determine the carrier concentration, as well as the supported computational information to further analyze these parameters.

3.3.1. Electrical transport property

The electrical performance evaluated by Seebeck coefficient (S) and electrical conductivity (σ) were concurrently recorded by ZEM-3 (ULVAC

Technologies, Inc., Japan) on a cuboid. **Figure 3.7** displays the ZEM-3 unit of Seebeck coefficient and electrical conductivity measuring system.

The electrical resistivity measurement is using the four-probe method, which is respectively distributed on the vertical two probes and the right side parallel two probes. At first, the bulk sample is loaded vertically in the middle of the upper and bottom current electrode, where the current went through. To ensure good contact, the sample surface needs to be smooth. After that, the two parallel thermocouples are set on the right side of bulks in order to detect the voltage. The electrical conductivity σ is calculated form measured electrical resistivity ρ with a formula $\sigma=1/\rho$, where the electrical resistivity is obtained by $\rho=RS/l$. The resistance R is achieved by the voltage V recorded by the right two parallel probes with a known distance l divided by current I given by a constant current power supply. S represents the cross-section area of the sample.

As shown in Figure 3.7, the whole sample and holders are put in a furnace, the lower block is the temperature setting heater to make a temperature alteration, and the parallel two thermocouples sense the temperature as well as the voltage variation. The Seebeck coefficient S is measured by a statistical DC method that measures the temperature gradient ΔT from the upper and lower temperatures T_1 and T_2, After that, the thermal electromotive force dE is measured between the same two probes on the right side of the thermocouple.

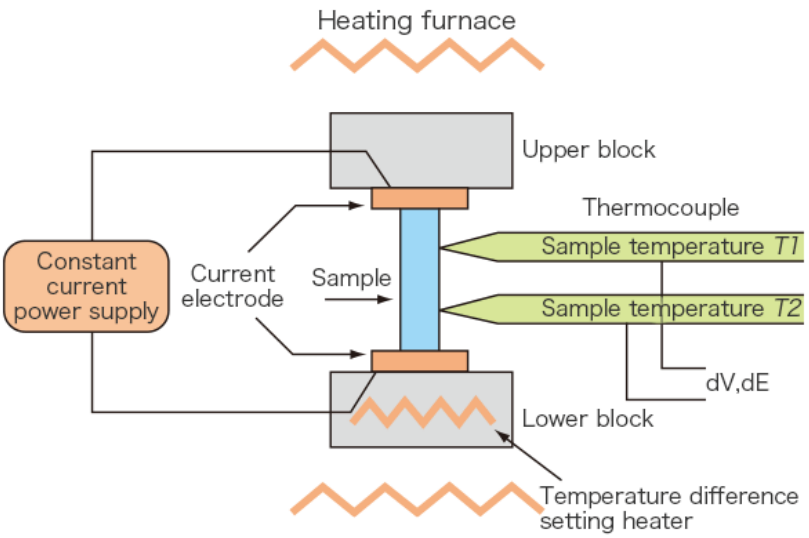

Figure 3.7. Schematic diagram of the Seebeck coefficient and electrical conductivity measuring system (ULVAC-ZEM-3) (https://showcase.ulvac.co.jp/en/products/heat-treatment-and-thermal-properties/thermoelectric-evaluation-device/thermoelectric properties/zem-3series.html).

All the samples are prepared for SPS sectioning and polishing. This experiment is conducted in a temperature range from 300K to 800K separated by a temperature difference of 10, 20,30 respectively, with the entire setup under low-pressure helium gas to avoid sample oxidation.

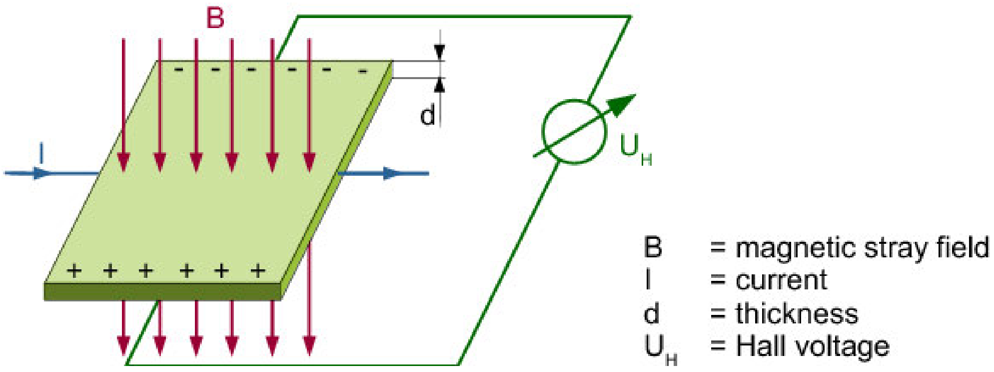

Figure 3.8. Schematic diagram of the Hall system principal.

The Hall coefficient (R_H) based on the Van der Pauw technique was utilized to obtain n_H and μ_H through the equations $n_H=1/(eR_H)$ and $\mu_H = \sigma R_H$, where e is the electron charge, n_H represents carrier concentration, and μ_H denotes carrier mobility. **Figure 3.8** shows the principle of the Hall system, a specific magnetic stray field B (1.5T during this research) perpendicular to the direction of current flow I can generate a fixed voltage V_H, so that R_H is obtained by V_H/I. All that is essential in evaluating the thermoelectric efficiency (zT) is the straightforward measurement of the resistivity, but additional information on the underlying transport and charging carrier scattering mechanisms is provided by the Hall carrier concentration and mobility.

3.3.2. Thermal transport property

The thermal transport properties in this project were measured by a laser flash diffusivity apparatus (LFA 467, Netzsch, Japan) as shown in **Figure 3.9**a-b, the result of the thermal diffusivity coefficient D was obtained. The total thermal conductivity (κ_{tot}) was calculated by the formula $\kappa_{tot}=D\times C_p\times\rho$, where C_p is the specific heat estimated from the Dulong-Petit approximation for heat capacity, ρ is the density of bulks acquired by applying Archimedes' law displayed in **Figure 3.9**c. To limit emissivity deviation, the sample was covered with a thin graphite layer.

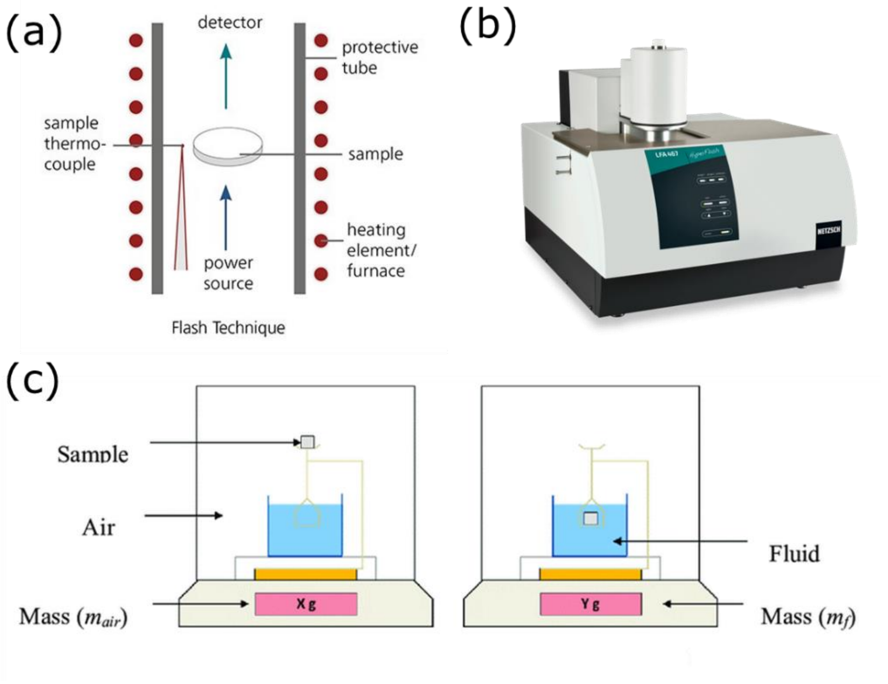

Figure 3.9. (a) The mechanism of LFA 467 for the measurement of *D*, (b) the picture of LFA 467 equipment, (c) the schematic diagram of Archimedes' method determining sample density (Arvieu, Cassiopée Galy, Guen, & Lacoste, 2020) (https://analyzingtesting.netzsch.com/en/products/thermal-diffusivity-and-conductivity/lfa-467-hyper-flash-light-flash-apparatus).

CHAPTER 4: THE EFFECT OF RARE EARTH ELEMENT DOPING ON THERMOELECTRIC PROPERTIES OF GETE

4.1. Introduction

As a promising medium-temperature thermoelectric material, GeTe shows high *zT*. Rare earth elements (REs) have a larger atomic mass (*M*) and radius (*R*) compared with Ge and can induce additional mass fluctuation and strain-field fluctuation, which can correspondingly strengthen phonon scattering to further reduce the κ_l. Correspondingly, in this study, the $Ge_{0.98}RE_{0.02}Te$ (RE = Eu, Gd, Er, Tm) was designed to investigate the effect of RE-substitution at the Ge site of GeTe on its thermoelectric performance.

4.2. Publication

4.3. Conclusion

The RE-doped GeTe with composition $Ge_{0.98}RE_{0.02}Te$ (RE = Eu, Gd, Er, Tm) was synthesized. RE doping effectively reduces the lattice thermal conductivity and enhances the power factor, which leads to increased *zT* values. However, the doping limit of REs on the GeTe system hinders the further enhancement of *zT* values. Hence, Lu with low electronegativity and a radius difference with Ge shows potential for further reduced lattice thermal conductivity and increased *zT* values. Thus, the Lu and Sb co-doped GeTe system was designed to achieve this purpose.

CHAPTER 5: CONDENSED POINT DEFECTS ENHANCE THERMOELECTRIC PERFORMANCE OF RARE EARTH LU-DOPED GETE

5.1. Introduction

The strength of point defect phonon scattering induced by element doping is evaluated by mass and radius differences between host and guest atoms. Rare earth elements (REs) show both a higher mass and radius difference than other elements and can significantly reduce κ_l. Our previous study has proven that rare-earth elements, Eu, Gd, Er, and Tm, can effectively reduce the κ_l and enhance the average zT of GeTe-based thermoelectric materials. However, due to the large electronegativity difference between rare-earth elements and Ge, the small solubility of rare-earth elements in GeTe limits their capacity for further enhancing thermoelectric performance. Lu with a smaller radius and electronegativity difference than other rare elements, may have a higher doping limit, which can further push the zT value up.

5.2. Publication

5.3. Conclusion

Lu doping effectively reduces the lattice thermal conductivity from 0.77 $W \cdot m^{-1} \cdot K^{-1}$ of GeTe to 0.35 $W \cdot m^{-1} \cdot K^{-1}$ of $Ge_{0.98}Lu_{0.02}Te$ at 673 K, and further induces a high *zT* value of 1.5 in $Ge_{0.98}Lu_{0.02}Te$ at 673 K. Extra Sb alloying optimizes the carrier concentration from 1.02×10^{21} cm^{-3} of $Ge_{0.98}Lu_{0.02}Te$ to 1.77×10^{20} cm^{-3} of $Ge_{0.90}Lu_{0.02}Sb_{0.08}Te$, which results in a reasonable power factor of 33.82 $\mu W \cdot cm^{-1} \cdot K^{-2}$ and a low electrical thermal conductivity of 0.75 $W \cdot m^{-1} \cdot K^{-1}$ at 673 K in $Ge_{0.90}Lu_{0.02}Sb_{0.08}Te$. Correspondingly, a peak *zT* of 1.75 at 673 K and an average *zT* of 0.92 within the temperature range of 303-723 K are obtained in $Ge_{0.9}Lu_{0.02}Sb_{0.08}Te$. The doping of rare earth elements can effectively optimize the thermoelectric performance of GeTe. In this circumstance, heavy rare earth elements were used in our projects. TAGS-85 as one of the promising GeTe-based alloys, has been used in devices and shows good performance. Considering this, the rare earth element Nd may show potential for further enhancing the *zT* values of the TAGS-85 system.

CHAPTER 6: RARE-EARTH ND INDUCING RECORD-HIGH THERMOELECTRIC PERFORMANCE OF $(GeTe)_{85}(AgSbTe_2)_{15}$

6.1. Introduction

As a rare-earth element, Nd as a dopant can affect the transport properties of thermoelectric materials in many ways: (a) Nd doping in TAGS-85 can result in local lattice distortion due to larger atomic size; (b) multielectron Nd^{3+} can affect carrier concentration due to different valence electron counts or influence of the chemical bond; (c) different from the large localized magnetic moments of Ce ($4f^{15}d^{16}s^2$) and Yb ($4f^{13}6s^2$), Nd ($4f^46s^2$) has a small localized magnetic effect, which can induce an interesting change to *S*. Considering the complex crystal structure of TAGS-85, three cation sites (Ge, Ag, and Sb) can be substituted by Nd compares the formation energy of Nd substitution at different cation sites of TAGS-85. Nd can preferentially substitute for Sb due to the lowest formation energy. Here, we design the sample with a nominal composition of $Ge_{0.74}Ag_{0.13}Sb_{0.13-x}Nd_xTe$ (x =0, 0.02, and 0.04) to optimize the thermoelectric performance.

6.2. Publication

AAAS
Energy Material Advances
Volume 2021, Article ID 2414286, 8 pages
https://doi.org/10.34133/2021/2414286

Energy Material Advances
A SCIENCE PARTNER JOURNAL

Research Article

Rare-Earth Nd Inducing Record-High Thermoelectric Performance of $(GeTe)_{85}(AgSbTe_2)_{15}$

Wan Yu Lyu,[1,2] **Min Hong**,[1,2] **Wei Di Liu**,[1,2] **Meng Li**,[2] **Qiang Sun**,[2] **Sheng Duo Xu**,[2]
Jin Zou,[2,3] **and Zhi-Gang Chen**[1,2]

[1]*Centre for Future Materials, University of Southern Queensland, Springfield, Queensland 4300, Australia*
[2]*School of Mechanical and Mining Engineering, The University of Queensland, Brisbane, Queensland 4072, Australia*
[3]*Centre for Microscopy and Microanalysis, The University of Queensland, Brisbane, Queensland 4072, Australia*

Correspondence should be addressed to Zhi-Gang Chen; zhigang.chen@usq.edu.au

Received 5 December 2020; Accepted 19 January 2021; Published 16 March 2021

As a promising midtemperature thermoelectric material with both higher thermoelectric performance and mechanical property, Tellurium Antimony Germanium Silver (TAGS-x), written as $(GeTe)_x(AgSbTe_2)_{1-x}$, especially $(GeTe)_{0.85}(AgSbTe_2)_{0.15}$ (TAGS-85), has attracted wide attention. Herein, we innovatively use Nd doping to synergistically decrease the carrier concentration to the optimal level leading to enhanced dimensionless figure of merit, zT. Our density-functional theory calculation results indicate that Nd-doping reduced carrier concentration should be attributed to the enlargement of band gap. The optimized carrier concentration results in an ultrahigh power factor of ~32 μW cm^{-1} K^{-2} at 727 K in $Ge_{0.74}Ag_{0.13}Sb_{0.11}Nd_{0.02}Te$. Simultaneously, the lattice thermal conductivity of $Ge_{0.74}Ag_{0.13}Sb_{0.11}Nd_{0.02}Te$ retained as low as ~0.5 at 727 K. Ultimately, a record-high zT of 1.65 at 727 K is observed in the $Ge_{0.74}Ag_{0.13}Sb_{0.11}Nd_{0.02}Te$. This study indicates rare-earth Nd doping is effective in boosting the thermoelectric performance of TAGS-85 and approached a record-high level via synergistic effect.

1. Introduction

Fossil fuel overexploitation and the corresponding environment pollution have called for growing development of sustainable energy-utilization technologies [1]. Thermoelectrics, which can achieve the reciprocal energy conversion between heat and electricity, are one promising candidate [2, 3]. However, the wide commercialization of thermoelectrics is limited by the low thermoelectric energy conversion efficiency, evaluated by the dimensionless figure of merit, $zT = S^2\sigma T/\kappa_{total}$. Here, S is the Seebeck coefficient, σ is the electrical conductivity, and κ_{total} represents the total thermal conductivity (accumulation of electron (κ_e) and lattice (κ_l) parts) [4]. $S^2\sigma$ is defined as the power factor to evaluate the overall electrical performance. To enhance zT, both high $S^2\sigma$ and low κ_{total} are required. Multiple strategies have been developed to enhance $S^2\sigma$ of thermoelectric materials, such as carrier concentration (n, n_p for holes) optimization [5, 6], resonance level engineering [7], band convergence [8–10], energy filtering [11], quantum confinement [12], and Rashba effect [13]. Alternatively, hierarchical phonon scattering centers, including point defects, dislocations, stacking faults, dense grain boundaries [14, 15], and phase interfaces, can effectively decrease κ_l and κ_{total} to achieve high zT values [16, 17].

IV-VI tellurides (Ge/Sn/Pb-Te) are promising midtemperature thermoelectric materials due to their relatively high zT values [5, 18–21]. For example, PbTe-based thermoelectric material has approached the high zT value of 2.2 at 915 K in PbTe-4 mol.% SrTe with 2 mol.% Na [18, 22]. However, the high toxicity of Pb limits its practical application. Alternatively, κ_l of SnTe is relatively higher which leads to lower zT value of only 1.51 at 800 K [23] comparing with PbTe [18] and GeTe [24]. Therefore, nontoxic and high-performance GeTe-based thermoelectric materials, with the peak zT values higher than 2 [24, 25], have attracted extensive attention. To boost the thermoelectric performance of GeTe with good mechanical property and make it suitable for application, rhombohedral GeTe is alloyed with cubic $AgSbTe_2$ and forms a continuous solid solution, called as Tellurium Antimony Germanium Silver (TAGS-x,

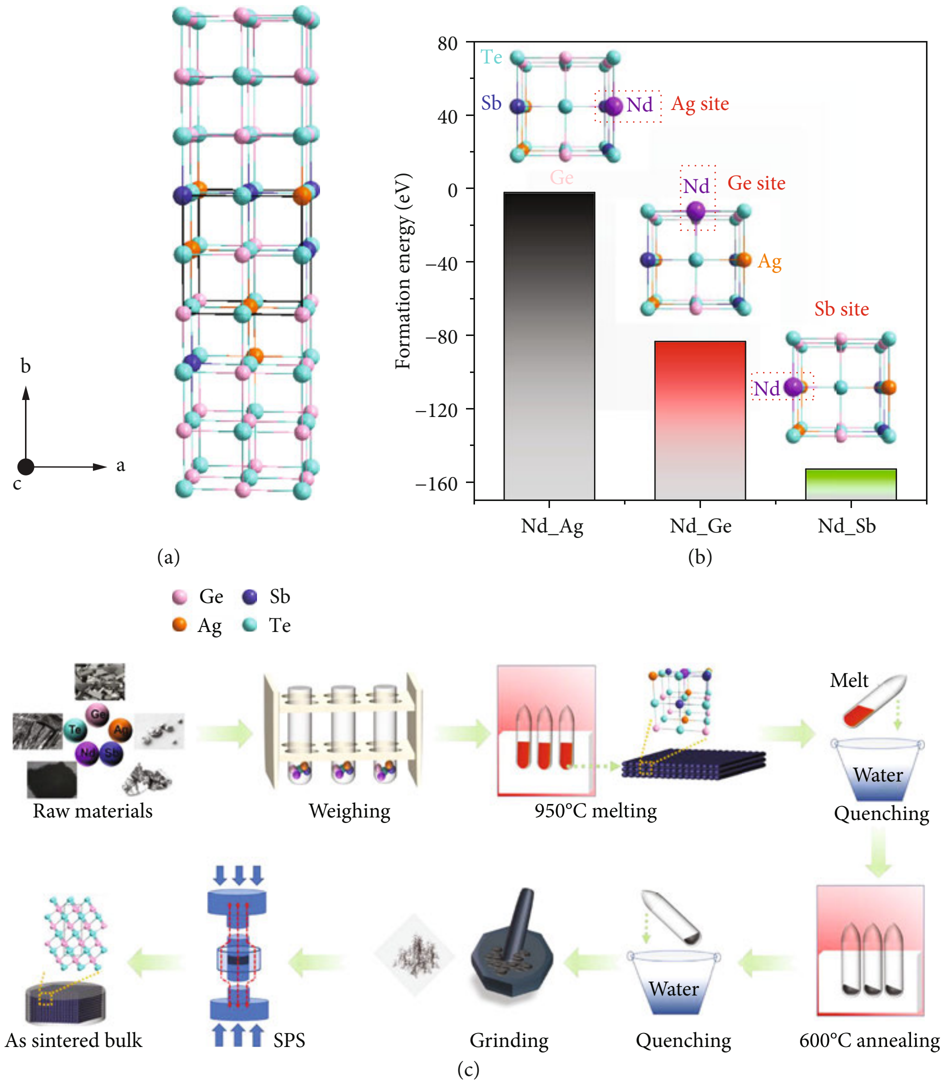

Figure 1: Experimental design and synthesis process. (a) Crystal structure of cubic TAGS-85; (b) calculated formation energy for Nd doping in Ag, Ge, and Sb sites of cubic TAGS-85, respectively; (c) schematic diagram of the experiment preparation process.

written as $(GeTe)_x(AgSbTe_2)_{1-x}$, where x ranges from 0.7 to 0.9) [26, 27]. TAGS-85, which can also be written as $Ge_{0.74}Ag_{0.13}Sb_{0.13}Te$, has approached the highest peak zT (zT_{max}) of 1.36 at 700 K with good mechanical properties (elastic modulus of 50 GPa and Poisson's ratio of 0.24) [27]. However, the thermoelectric performance of TAGS-85 is still lower than other state-of-the-art thermoelectric materials, such as PbTe [28]. Thus, recent studies of TAGS-85 focus on further improving the thermoelectric performance. Self-doping achieved by tuning the ratio of Ag/Sb ratio can effectively enhance the zT_{max} value of TAGS-85 up to 1.6 at 750 K [29]. Levin et al. [30, 31] reported that the large atomic size and localized magnetic moment of rare-earth elements Dy, Yb, and Ce can increase zT values of TAGS-85. For example, 1% Ce and 1% Yb substitution in Te site can boost up S by 16% to 205 $\mu V\,K^{-1}$ [30], attributed to the localized paramagnetic moment, leading to an enhanced zT_{max} of 1.5 at 700 K.

To better understand the influence of rare-earth element doping on thermoelectric performance of TAGS-85, we selected Nd as the dopant to optimize thermoelectric performance of TAGS-85. As a rare-earth element, Nd as dopant can affect transport properties of thermoelectric materials in many ways: (a) Nd doping in TAGS-85 can result in local lattice distortion due to larger atomic size; (b) multielectron Nd^{3+} can affect carrier concentration due to different valence electron counts or influence of the chemical bond [32]; (c) different with large localized magnetic moments of Ce ($4f^1 5d^1 6s^2$) and Yb ($4f^{13} 6s^2$), Nd ($4f^4 6s^2$) has small localized magnetic effect, which can induce interesting change to S [30, 31]. Considering the complex crystal structure of TAGS-85, three cation sites (Ge, Ag, and Sb) can be substitute by Nd (Figure 1(a)). Figure 1(b) compares the formation energy of Nd substitution at different cation sites of TAGS-85. As can be seen, Nd can preferentially substitute Sb due to the lowest formation energy. Here, we design the sample with nominal composition as $Ge_{0.74}Ag_{0.13}Sb_{0.13-x}Nd_xTe$ ($x = 0$, 0.02, and 0.04). Figure 1(c) schematically shows the experiment process, where all samples are prepared by

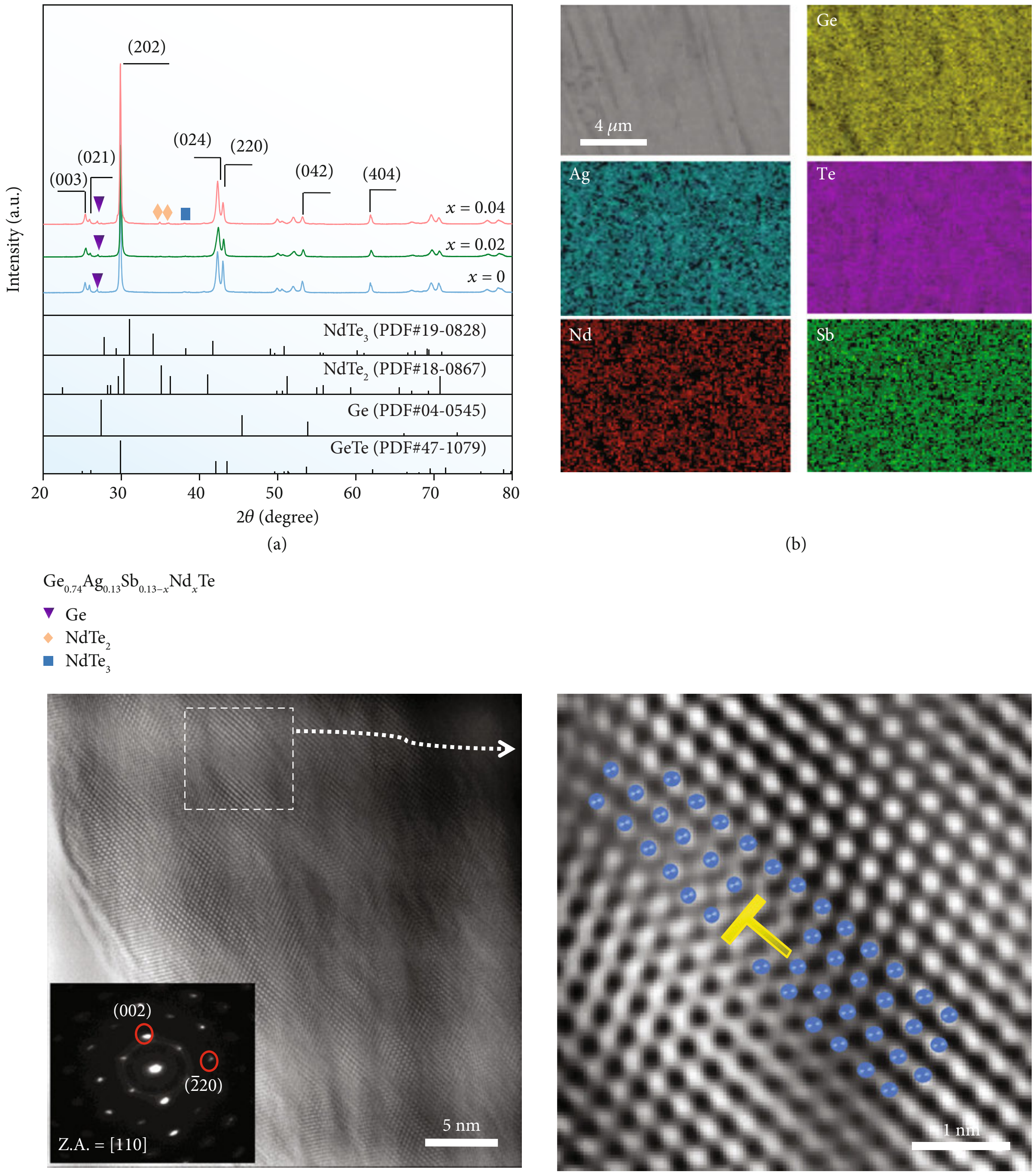

(a)

(b)

(c)

(d)

Figure 2: Characterization of crystal structure and microstructure morphologies. (a) XRD patterns of as-sintered $Ge_{0.74}Ag_{0.13}Sb_{0.13\text{-}x}Nd_xTe$ ($x = 0$, 0.02, and 0.04) pellets, (b) backscattered SEM images of corresponding EDS element maps of as-sintered $Ge_{0.74}Ag_{0.13}Sb_{0.11}Nd_{0.02}Te$ pellet, (c) HRTEM image of as-sintered $Ge_{0.74}Ag_{0.13}Sb_{0.11}Nd_{0.02}Te$ pellet (inset is the corresponding SAED pattern in [110] zone axis (Z.A.)), and (d) enlarged HRTEM of white square circled area in (c).

melting, quenching, annealing, and spark plasma sintering (SPS). Our results show that Nd doping can effectively reduce n_p of TAGS-85 close to the optimal level due to band gap enlargement. Correspondingly, zT_{max} can be boosted to as high as 1.65 in $Ge_{0.74}Ag_{0.13}Sb_{0.11}Nd_{0.02}Te$.

2. Experimental Methods

2.1. Synthesis. Polycrystalline Nd-doped TAGS-85 was prepared in the formulae of $Ge_{0.74}Ag_{0.13}Sb_{0.13\text{-}x}Nd_xTe$ ($x = 0$, 0.02, and 0.04). Precursors, including Ge (99.999%, Sigma-

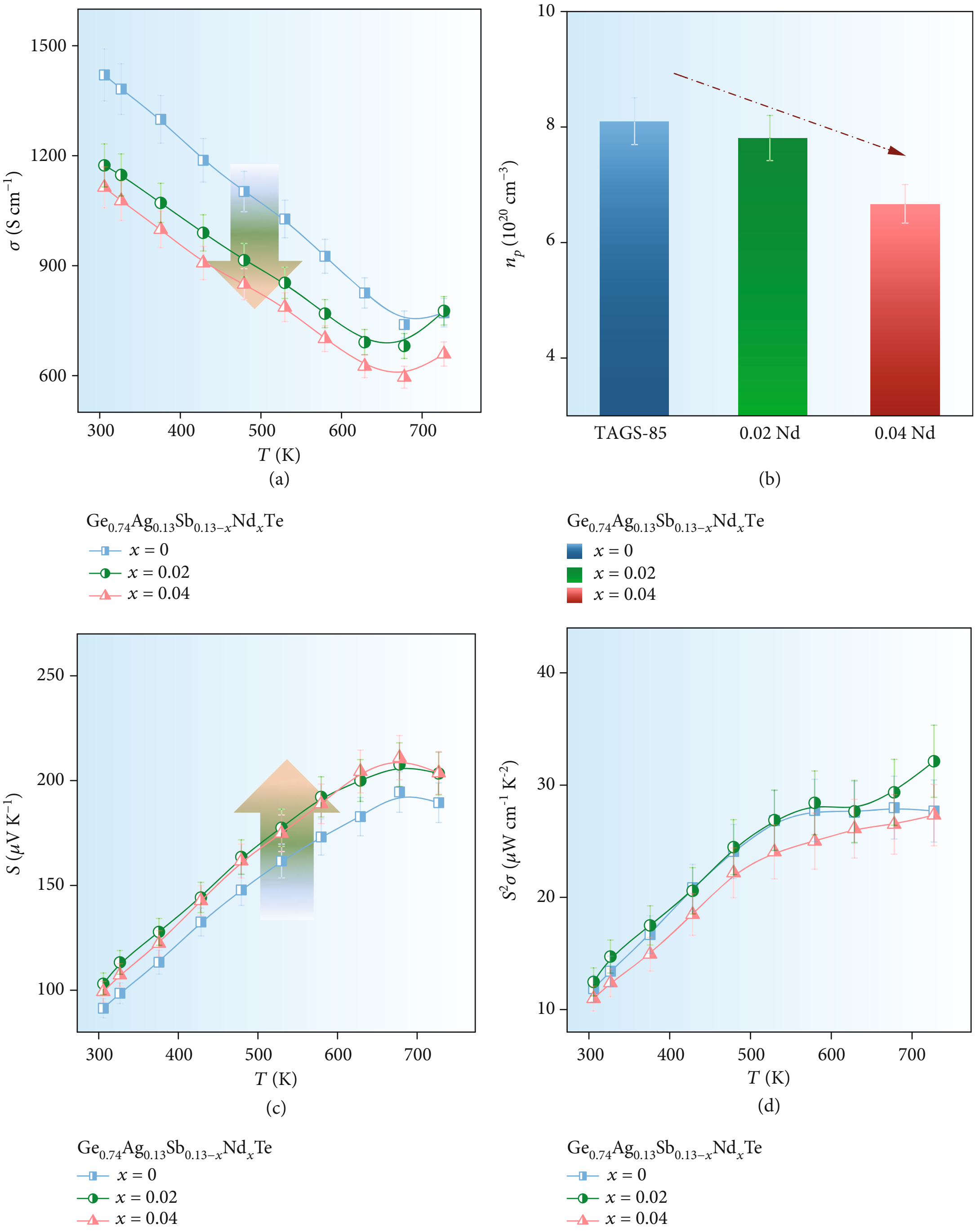

FIGURE 3: Electrical property of the as-sintered $Ge_{0.74}Ag_{0.13}Sb_{0.13-x}Nd_xTe$ ($x = 0$, 0.02, and 0.04) pellets. (a) Temperature-dependent σ, (b) room temperature n_p, (c) temperature-dependent S, and (d) $S^2\sigma$ of the as-sintered $Ge_{0.74}Ag_{0.13}Sb_{0.13-x}Nd_xTe$ ($x = 0$, 0.02, and 0.04) pellets.

Aldrich, Australia), Te (99.999%, Sigma-Aldrich, Australia), Ag (99.99%, Sigma-Aldrich, United States), Sb (99.999%, Alfa Aesar, United States), and Nd (99.999%, Alfa Aesar, United States), were weighed following the nominal compositions. The weighted precursors were sealed in quartz ampules and heated in 1223 K for 12 hours followed by water quenching. The obtained samples were further annealed at 873 K for 2 days and quenched again. This two-step quenching method is designed to reduce Ge vacancies and inhibit the formation of the second phase, Ag_8GeTe_6 [33]. The resultant products were further ground into powders and sintered into pellets (SPS, 65 MPa and 673 K) for performance measurement.

2.2. Characterization. The crystal structures of as-prepared samples were characterized by X-ray diffraction (XRD, Bruker, United States, Cu K_α radiation with a wavelength of 1.5418 Å, $10^\circ \leq 2\theta \leq 80^\circ$, step with 0.02°). A field-emission scanning electron microscope (FE-SEM, JSM-7001F, JEOL, Japan) equipped with energy-dispersive spectrum (EDS)

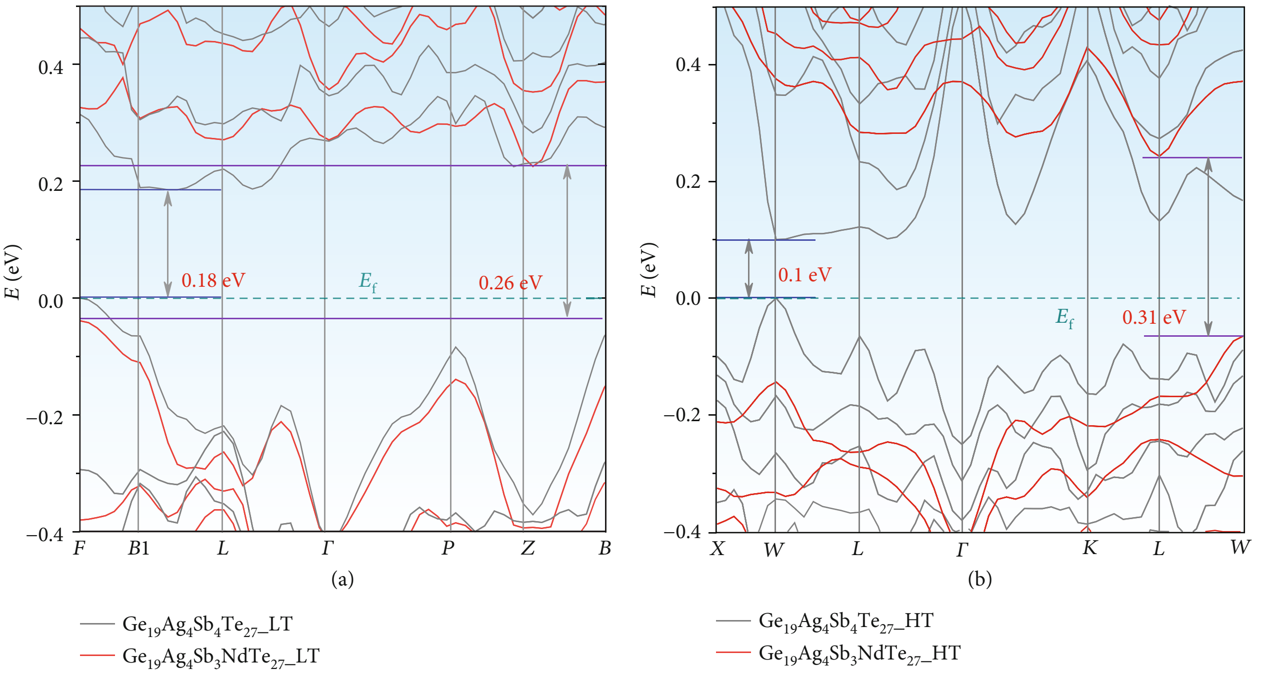

FIGURE 4: Calculated band structures of pristine TAGS-85 ($Ge_{19}Ag_4Sb_4Te_{27}$) and Nd-doped TAGS-85 ($Ge_{19}Ag_4Sb_3Nd_1Te_{27}$) in (a) low-temperature phase and (b) high-temperature phase.

detector was employed to explore the morphologies and compositions. To further understand the structural information, the $Ge_{0.74}Ag_{0.13}Sb_{0.11}Nd_{0.02}Te$ sample was characterized by a transmission electron microscope (TEM, Tecnai F20, Philips, United States).

2.3. Thermoelectric Property Measurement. S and σ of the sintered pellets were simultaneously measured by ZEM-3 (ULVAC Technologies, Inc., Japan). κ_{total} is calculated by $\kappa_{total} = D \times C_p \times \rho$, where C_p is the specific heat estimated from the Dulong-Petit approximation [34], ρ is the pellet densities measured by Archimedes method, the densities are shown in supporting information Table S1, and D is the thermal diffusivity coefficient measured by the laser flash diffusivity apparatus (LFA 457, Netzsch, Germany). The Hall coefficient (R_H) was measured based on the Van der Pauw technique [35]. n_p and hole mobility (μ) were through the equation $n_p = 1/(eR_H)$ and $\mu = \sigma R_H$, where e is the electron charge.

2.4. Density Functional Theory Calculations. Band structures were calculated by using the plane-wave self-consistent field code [36]. A uniform mesh of $2 \times 2 \times 2k$-points was used in sampling integrations over the Brillouin zone. The band structures of pristine TAGS-85 and Nd-doped TAGS-85 were calculated based on $Ge_{19}Ag_4Sb_4Te_{27}$ and $Ge_{19}Ag_4Sb_3Nd_1Te_{27}$ with the uniform mesh of $2 \times 2 \times 2k$-points, respectively.

3. Results and Discussions

Figure 2(a) shows room temperature X-ray diffraction (XRD) patterns of the as-sintered ($Ge_{0.74}Ag_{0.13}Sb_{0.13\text{-}x}Nd_xTe$) ($x = 0$, 0.02, and 0.04) pellets. All main peaks can be indexed as R-GeTe (space group R3m) whose structure is a slightly distorted rock-salt structure along the [111] direction [20]. Ge precipitates (purple triangle) were detected as normal due to the nature of easily formed Ge vacancies in GeTe-based thermoelectric materials [37–39]. When the Nd doping level reaches as high as $x = 0.04$, $NdTe_2$ (yellow diamond) and $NdTe_3$ (blue square) impurities can be found. Figure 2(b) shows the backscattered scanning electron microscopy (SEM) image and corresponding energy-dispersive spectrum (EDS) maps of the $Ge_{0.74}Ag_{0.13}Sb_{0.11}Nd_{0.02}Te$ sample. As can be seen, Ge, Te, Ag, Sb, and Nd are homogeneously distributed in the matrix, indicating that Nd has successfully doped into TAGS-85. Figures 2(c) and 2(d) show high-resolution (HR) transition electron microscopy (TEM) image of $Ge_{0.74}Ag_{0.13}Sb_{0.11}Nd_{0.02}Te$ pellet along the [110] zone axis (indexed from the selected area electron diffraction (SEAD) pattern as shown in the inset of Figure 2(c)). Figure 2(d) shows its enlarged HRTEM image in the marked square area of Figure 2(c), where the dislocations caused by Nd doping-induced dense point defects can be clearly observed.

Figure 3(a) shows temperature-dependent σ of the as-sintered $Ge_{0.74}Ag_{0.13}Sb_{0.13\text{-}x}Nd_xTe$ pellets. All samples show degenerated semiconducting behavior, and σ of $Ge_{0.74}Ag_{0.13}Sb_{0.11}Nd_{0.02}Te$ decreases from 1178.10 at room temperature to 687.45 S cm^{-1} at 673 K. With increasing the Nd doping level, σ at room temperature reduces from 1424.45 to 1108.89 S cm^{-1}. The observed reduced σ should be attributed to reduced n_p as shown in Figure 3(b). Figure 3(c) shows temperature-dependent S of the as-sintered $Ge_{0.74}Ag_{0.13}Sb_{0.13\text{-}x}Nd_xTe$ pellets. With increasing the Nd doping level, room temperature S of $Ge_{0.74}Ag_{0.13}Sb_{0.13\text{-}x}Nd_xTe$ slightly increases from 92 to 104 μV K^{-1} due to the reduced n_p. S of $Ge_{0.74}Ag_{0.13}Sb_{0.09}Nd_{0.04}Te$ can approach as high as 210 μV K^{-1} at 678 K.

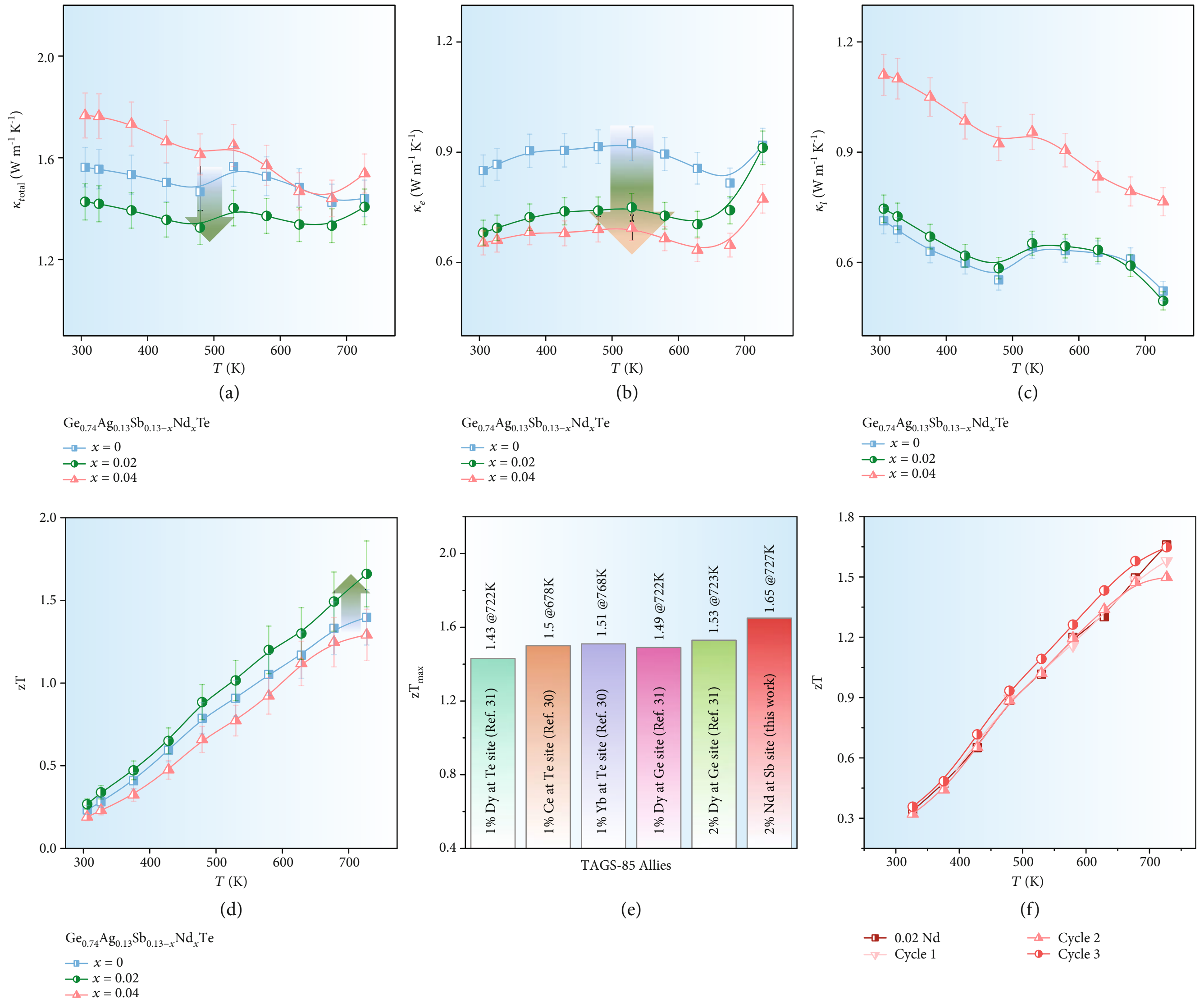

Figure 5: Analysis of thermal performance and optimized zT values. (a) Temperature-dependent κ_{total}, (b) κ_e, (c) κ_l, and (d) zT values of the as-sintered $Ge_{0.74}Ag_{0.13}Sb_{0.13-x}Nd_xTe$ ($x = 0$, 0.02, and 0.04). (e) Comparison of the obtained zT_{max} of $Ge_{0.74}Ag_{0.13}Sb_{0.11}Nd_{0.02}Te$ with other rare-earth element-doped TAGS-85 [30, 31] and (f) cycle test results for $Ge_{0.74}Ag_{0.13}Sb_{0.11}Nd_{0.02}Te$.

Figure 3(d) illustrates temperature-dependent $S^2\sigma$ of the as-sintered $Ge_{0.74}Ag_{0.13}Sb_{0.13-x}Nd_xTe$ pellets. An enhanced $S^2\sigma$ of 32 μW cm^{-1} K^{-2} at 727 K can be observed in $Ge_{0.74}Ag_{0.13}Sb_{0.11}Nd_{0.02}Te$.

To understand the change of electrical transport properties, we calculated the electronic band structure of pristine TAGS-85 ($Ge_{19}Ag_4Sb_4Te_{27}$) and Nd-doped TAGS-85 ($Ge_{19}Ag_4Sb_3Nd_1Te_{27}$). Figure 4(a) compares the calculated electronic band structures of low-temperature (LT) $Ge_{19}Ag_4Sb_4Te_{27}$ and $Ge_{19}Ag_4Sb_3Nd_1Te_{27}$. After Nd doping, the valence band maximum (VBM) shifts result in changed band gap from indirect to direct type. The band gap increases from 0.18 eV of $Ge_{19}Ag_4Sb_4Te_{27}$ to 0.26 eV of $Ge_{19}Ag_4Sb_3Nd_1Te_{27}$. Nd doping also effectively enlarges the band gap of high-temperature (HT) TAGS-85 from 0.1 eV of $Ge_{19}Ag_4Sb_4Te_{27}$ to 0.31 eV of $Ge_{19}Ag_4Sb_3Nd_1Te_{27}$, as shown in Figure 4(b). The enlarged band gap of both LT and HT TAGS-85 after Nd doping can well explain the decrease of n_p.

Figures 5(a)–5(c) show temperature-dependent thermal transport properties of the as-sintered $Ge_{0.74}Ag_{0.13}Sb_{0.13-x}Nd_xTe$ pellets. As shown in Figure 5(a), κ_{total} of TAGS-85 slightly decreases after Nd doping. However, with increasing the content of Nd to 0.04, the room temperature κ_{total} increases to 1.76 W m^{-1} K^{-1}. To better understand the effect of Nd doping on the thermal transport properties of TAGS-85, κ_e and κ_l were further calculated as shown in Figures 5(b) and 5(c). κ_l was estimated by subtracting κ_e from κ_{total}. κ_e and the Lorenz number (L) were calculated based on the classic single parabolic band model. As can be seen, κ_e decreases from 0.85 to 0.65 W m^{-1} K^{-1} at room temperature with increasing the Nd content due to reduced σ. With 2% Nd doping, κ_l shows no obvious change. When the Nd doping level further increases to 4% to surpass the solubility limit, the room temperature κ_l increases from 0.70 to 1.11 W m^{-1} K^{-1} due to additional impurity phases $NdTe_2$ and $NdTe_3$ [40]. Figure 5(d) plots temperature-dependent zT values of the as-sintered $Ge_{0.74}Ag_{0.13}Sb_{0.13\text{-}x}Nd_xTe$ pellets and shows increased zT values with increasing temperature. The zT_{max} value of $Ge_{0.74}Ag_{0.13}Sb_{0.11}Nd_{0.02}Te$ can reach 1.65 at 727 K. Figure 5(e) compares the zT_{max} values of this study with previously reported Ce-, Yb-, and Dy-doped TAGS-85 [30, 31]. In our study, Nd tends to substitute the Sb site, which is different from Ce, Yb (Te site), and Dy (Ge site). Different occupation sites can result in various effects on electrical and thermal properties. Thus, Nd doping in the Sb site can decrease both the carrier concentration and thermal conductivity. This results in the highest zT value of 1.65 at 727 K. Figure 5(f) presents the reproductivity of $Ge_{0.74}Ag_{0.13}Sb_{0.11}Nd_{0.02}Te$ in three cycling tests, suggesting high stability of the Nd-doped TAGS-85.

4. Conclusion

In this study, we achieve a record-high zT of 1.65 at 727 K in $Ge_{0.74}Ag_{0.13}Sb_{0.11}Nd_{0.02}Te$ mainly due to κ_{total} reduction while maintaining high $S^2\sigma$. Reduced κ_{total} should be attributed to reduced σ due to decreased n_p. Although reduced n_p deteriorates σ, reduced n_p also slightly increases S, leading to nearly unchanged $S^2\sigma$. Our DFT calculation suggests that reduced n_p is caused by the Nd doping-induced band gap enlargement. Comparing with other rare-earth elements, Nd is more effective in enhancing the thermoelectric performance of TAGS-85. The Nd-doped TAGS-85 also shows high stability.

Data Availability

All data required to support this study are presented in the paper and the supporting document. Additional data are available upon request from the authors.

Conflicts of Interest

The authors declare that they have no conflicts of interest.

Acknowledgments

This work was financially supported by the Australian Research Council, Innovation Centre for Sustainable Steel project, and University of Southern Queensland strategic research grant. LWY thanks the Chinese Scholarship Council for providing the Ph.D. stipend.

Supplementary Materials

Figure S1: Hall mobility (μ) of the Nd-doped TAGS-85 at the room temperature. Table S1: the density of as-prepared samples. *(Supplementary Materials)*

References

[1] J. He and T. M. Tritt, “Advances in thermoelectric materials research: looking back and moving forward,” *Science*, vol. 357, no. 6358, article eaak9997, 2017.

[2] G. J. Snyder and E. S. Toberer, “Complex thermoelectric materials,” *Nature Materials*, vol. 7, no. 2, pp. 105–114, 2008.

[3] L. E. Bell, “Cooling, heating, generating power, and recovering waste heat with thermoelectric systems,” *Science*, vol. 321, no. 5895, pp. 1457–1461, 2008.

[4] D. M. Rowe, *Thermoelectrics-Handbook-Macro-to-Nano*, CRC Press, 2006.

[5] Y. Pei, A. D. LaLonde, N. A. Heinz et al., “Stabilizing the optimal carrier concentration for high thermoelectric efficiency,” *Advanced Materials*, vol. 23, no. 47, pp. 5674–5678, 2011.

[6] Y. Pei, A. F. May, and G. J. Snyder, “Self-tuning the carrier concentration of PbTe/Ag2Te composites with excess Ag for high thermoelectric performance,” *Advanced Energy Materials*, vol. 1, no. 2, pp. 291–296, 2011.

[7] M. Hong, Z. G. Chen, L. Yang et al., “Realizing *zT* of 2.3 in $Ge_{1-x-y}Sb_xIn_yTe$ via reducing the phase-transition temperature and introducing resonant energy doping,” *Advanced Materials*, vol. 30, no. 11, article 1705942, 2018.

[8] Y. Tang, Z. M. Gibbs, L. A. Agapito et al., “Convergence of multi-valley bands as the electronic origin of high thermoelectric performance in $CoSb_3$ skutterudites,” *Nature Materials*, vol. 14, no. 12, pp. 1223–1228, 2015.

[9] Y. Pei, H. Wang, and G. J. Snyder, “Band engineering of thermoelectric materials,” *Advanced Materials*, vol. 24, no. 46, pp. 6125–6135, 2012.

[10] W. He, D. Wang, H. Wu et al., “High thermoelectric performance in low-cost $SnS_{0.91}Se_{0.09}$ crystals,” *Science*, vol. 365, no. 6460, pp. 1418–1424, 2019.

[11] H. R. Yang, J. H. Bahk, T. Day et al., “Enhanced Thermoelectric Properties in Bulk Nanowire Heterostructure-Based Nanocomposites through Minority Carrier Blocking,” *Nano Letters*, vol. 15, no. 2, pp. 1349–1355, 2015.

[12] M. S. Dresselhaus, G. Chen, M. Y. Tang et al., “New directions for low-dimensional thermoelectric materials,” *Advanced Materials*, vol. 19, no. 8, pp. 1043–1053, 2007.

[13] M. Hong, W. Lyv, M. Li et al., “Rashba Effect Maximizes Thermoelectric Performance of GeTe Derivatives,” *Joule*, vol. 4, no. 9, pp. 2030–2043, 2020.

[14] H. Xie, H. Wang, Y. Pei et al., “Beneficial contribution of alloy disorder to electron and phonon transport in half-Heusler thermoelectric materials,” *Advanced Functional Materials*, vol. 23, no. 41, pp. 5123–5130, 2013.

[15] J. Mao, J. L. Niedziela, Y. Wang et al., “Self-compensation induced vacancies for significant phonon scattering in InSb,” *Nano Energy*, vol. 48, pp. 189–196, 2018.

[16] L. Yang, Z.-G. Chen, G. Han, M. Hong, Y. Zou, and J. Zou, “High-performance thermoelectric Cu_2Se nanoplates through nanostructure engineering,” *Nano Energy*, vol. 16, pp. 367–374, 2015.

[17] S. N. Girard, J. He, C. Li et al., “In situ nanostructure generation and evolution within a bulk thermoelectric material to reduce lattice thermal conductivity,” *Nano Letters*, vol. 10, no. 8, pp. 2825–2831, 2010.

[18] K. Biswas, J. He, I. D. Blum et al., “High-performance bulk thermoelectrics with all-scale hierarchical architectures,” *Nature*, vol. 489, no. 7416, pp. 414–418, 2012.

[19] Q. Zhang, B. Liao, Y. Lan et al., “High thermoelectric performance by resonant dopant indium in nanostructured SnTe,” *Proceedings National Academy of Sciences of the United States of America*, vol. 110, no. 33, pp. 13261–13266, 2013.

[20] M. Hong, Y. Wang, W. D. Liu et al., “Arrays of planar vacancies in superior thermoelectric $ge_{1-x-y}Cd_xBi_yTe$ with band

convergence," *Advanced Energy Materials*, vol. 8, no. 30, article 1801837, 2018.

[21] J. Li, Z. W. Chen, X. Y. Zhang, Y. X. Sun, J. Yang, and Y. Z. Pei, "Electronic origin of the high thermoelectric performance of GeTe among the p-type group IV monotellurides," *NPG Asia Materials*, vol. 9, no. 3, article e353, 2017.

[22] Y. J. Kim, L. D. Zhao, M. G. Kanatzidis, and D. N. Seidman, "Analysis of nanoprecipitates in a Na-doped PbTe–SrTe thermoelectric material with a high figure of merit," *ACS Applied Materials & Interfaces*, vol. 9, no. 26, pp. 21791–21797, 2017.

[23] Z. Ma and J. Lei, "Enhancement of thermoelectric properties in Pd–In Co-doped SnTe and its phase transition behavior," *ACS Applied Materials & Interfaces*, vol. 11, no. 37, pp. 33792–33802, 2019.

[24] M. Hong, Y. Wang, T. L. Feng et al., "strong phonon–phonon interactions securing extraordinary thermoelectric $Ge_{1-x}Sb_xTe$ with Zn-alloying-induced band alignment," *Journal of the American Chemical Society*, vol. 141, pp. 1742–1748, 2019.

[25] L. Xie, Y. Chen, R. Liu et al., "Stacking faults modulation for scattering optimization in GeTe-based thermoelectric materials," *Nano Energy*, vol. 68, article 104347, 2020.

[26] J. R. Salvador, J. Yang, X. Shi, H. Wang, and A. A. Wereszczak, "Transport and mechanical property evaluation of $(AgSbTe)_{1-x}(GeTe)_x$(x=0.80, 0.82, 0.85, 0.87, 0.90)," *Journal of Solid State Chemistry*, vol. 182, no. 8, pp. 2088–2095, 2009.

[27] H. S. Kim, P. Dharmaiah, and S. J. Hong, "Thermoelectric properties of texture-controlled $(GeTe)_x(AgSbTe_2)_{100-x}$ (x=75, 80, 85, and 90) alloys fabricated by gas-atomization and hot-extrusion processes," *Journal of Electronic Materials*, vol. 47, no. 6, pp. 3119–3126, 2018.

[28] H. J. Wu, L. D. Zhao, F. S. Zheng et al., "Broad temperature plateau for thermoelectric figure of merit ZT>2 in phase-separated $PbTe_{0.7}S_{0.3}$," *Nature Communications*, vol. 5, no. 1, article 4515, 2014.

[29] T. J. Zhu, H. L. Gao, Y. Chen, and X. B. Zhao, "Ioffe–Regel limit and lattice thermal conductivity reduction of high performance $(AgSbTe_2)_{15}(GeTe)_{85}$ thermoelectric materials," *Journal of Materials Chemistry A*, vol. 2, no. 9, pp. 3251–3256, 2014.

[30] E. M. Levin, B. A. Cook, J. L. Harringa, S. L. Bud'ko, R. Venkatasubramanian, and K. Schmidt-Rohr, "Analysis of Ce- and Yb-doped TAGS-85 materials with enhanced thermoelectric figure of merit," *Advanced Functional Materials*, vol. 21, no. 3, pp. 441–447, 2011.

[31] E. M. Levin, S. L. Bud'ko, and K. Schmidt-Rohr, "Enhancement of thermopower of TAGS-85 high-performance thermoelectric material by doping with the rare earth Dy," *Advanced Functional Materials*, vol. 22, no. 13, pp. 2766–2774, 2012.

[32] A. Novitskii, G. Guélou, D. Moskovskikh et al., "Reactive spark plasma sintering and thermoelectric properties of Nd-substituted BiCuSeO oxyselenides," *Journal of Alloys and Compounds*, vol. 785, pp. 96–104, 2019.

[33] A. Kumar, P. A. Vermeulen, B. J. Kooi et al., "A cubic room temperature polymorph of thermoelectric TAGS-85," *RSC Advances*, vol. 8, no. 74, pp. 42322–42328, 2018.

[34] J. Li, X. Y. Zhang, S. Q. Lin, Z. W. Chen, and Y. Z. Pei, "Realizing the high thermoelectric performance of GeTe by Sb-doping and Se-alloying," *Chemistry of Materials*, vol. 29, no. 2, pp. 605–611, 2017.

[35] K. A. Borup, E. S. Toberer, L. D. Zoltan et al., "123902Measurement of the electrical resistivity and Hall coefficient at high temperatures," *The Review of Scientific Instruments*, vol. 83, no. 12, 2012.

[36] P. Giannozzi, O. Andreussi, T. Brumme et al., "QUANTUM ESPRESSO: a modular and open-source software project for quantum simulations of materials," *Journal of Physics: Condensed Matter*, vol. 21, no. 39, article 395502, 2009.

[37] A. Edwards, A. Pineda, P. Schultz et al., "Electronic structure of intrinsic defects in crystalline germanium telluride," *Physical Review B*, vol. 73, no. 4, article 045210, 2006.

[38] D. H. Damon, M. S. Lubell, and R. Mazelsky, "Nature of the defects in germanium telluride," *Journal of Physics and Chemistry of Solids*, vol. 28, no. 3, pp. 520–522, 1967.

[39] F. Fahrnbauer, D. Souchay, G. Wagner, and O. Oeckler, "High thermoelectric figure of merit values of germanium antimony tellurides with kinetically stable cobalt germanide precipitates," *Journal of the American Chemical Society*, vol. 137, no. 39, pp. 12633–12638, 2015.

[40] S. Kim and H. S. Lee, "Effects of addition of Si and Sb on the microstructure and thermoelectric properties of GeTe," *Metals and Materials International*, vol. 25, no. 2, pp. 528–538, 2019.

6.3. Conclusion

Rare earth Nd doping in TAGS-85 ($GeTe_{85}(AgSbTe_2)_{15}$) obtained the highest *zT* values in this TAGS-85 system. In this study, a record-high *zT* of 1.65 at 727K in $Ge_{0.74}Ag_{0.13}Sb_{0.11}Nd_{0.02}Te$ was achieved due to κ_{tot} reduction and a maintained high $S^2\sigma$ caused by the reduced n_p. The rare earth shows great potential for thermoelectric performance enhancement. Other optimization, including increasing the doping limit by tuning synthesis conditions, may strengthen the point defect scattering effect and also make a great contribution to *S* by further reducing carrier concentration.

CHAPTER 7: DISCUSSION AND CONCLUSIONS

7.1. Conclusion

GeTe thermoelectric materials have been one of the most promising thermoelectric materials in the medium temperature range, with a high *zT* value above 2. The current performance improvement strategies mostly use the doping of common elements, and the influence of the doping of rare earth elements and their own magnetic properties on thermoelectric performance remains to be studied. The reported κ_{lat} still higher than the theoretically minimal κ_{min}, rare earth elements theoretically have the largest mass and strain-field fluctuation effect on point defect scattering, which dominates the phonon scattering of the lattice. This motivates us to investigate the rare earth elements doped GeTe system for the purpose of reducing the κ_{lat}, exploring the effect of doping with magnetic momentum elements on the thermoelectric properties of GeTe, providing a forward thrust for the thermoelectric properties of materials to advance the commercialization process, and filling knowledge gaps in elemental doping of thermoelectric materials. This project focuses on rare earth elements doped with GeTe. Firstly, the thermoelectric performance of GeTe-based thermoelectric materials can be significantly enhanced by introducing RE (Eu, Gd, Er, and Tm) substitutions at the Ge site of GeTe. The increased local magnetic moment of REs induces increased m^* and enhanced S, which correspondingly leads to overall enhanced $S^2\sigma$ at the entire temperature range. The additional mass and radius fluctuations induced by RE substitutions also effectively increase the Γ_{EXP}, reduce the v, and correspondingly achieve the ultralow κ_{lat} as low as 0.07 W m^{-1} K^{-1}. Accordingly, the *zT* values at the entire temperature range are enhanced, leading to an increased zT_{ave} from 0.38 of pristine GeTe to ~ 0.60 of $Ge_{0.98}RE_{0.02}Te$. Our study demonstrates the effectiveness of RE substitutions at the Ge site in GeTe and can inspire the development of

GeTe thermoelectrics with enhanced thermoelectric properties. The thermoelectric performance of RE-doped GeTe can possibly be further enhanced by Sb or Bi co-doping. Secondly, rare earth Lu doping was conducted to examine the lattice thermal conductivity limited by doping content, and Sb/Bi co-doping was applied to further n_p optimization. Lu reduces lattice thermal conductivity by condensing point defect scattering. Sb co-doping optimizes the carrier concentration to 1.77×10^{20} cm^{-3}. The enhanced figure of merit of 1.75 was obtained for $Ge_{0.9}Lu_{0.02}Sb_{0.08}Te$ at 673 K. TAGS-85 is one of the promising GeTe-based materials that have been used to achieve devices with high efficiency. Rare earth Nd doping in TAGS-85 ($GeTe_{85}(AgSbTe_2)_{15}$) obtained the highest zT values in this TAGS-85 system. In this study, a record-high zT of 1.65 at 727K was obtained in $Ge_{0.74}Ag_{0.13}Sb_{0.11}Nd_{0.02}Te$ due to κ_{tot} reduction and a high $S^2\sigma$ due to the reduced n_p. This is caused by the Nd doping-induced band gap enlargement.

7.2. Contribution

i. Academic contribution: Firstly, we may solve the remaining problems of thermoelectric materials in GeTe. We may find new ways to optimize efficiency to a higher level, which will push the application of thermoelectric effects. Furthermore, we may enrich the scientific knowledge tree and provide a reference for peers by contributing to the novel material optimization of the thermoelectric material GeTe.

ii. Commercial benefit: Secondly, improving the figure of merit of GeTe may push the thermoelectric device into diversified thermoelectric products.

iii. Environment and Energy: Therefore, the wide application of thermoelectric devices can effectively replace some fossil fuels, which will mitigate environmental pollution and energy shortages.

7.3. Outlook

With massive efforts and continuously optimized strategies, the above discussion clarifies the great potential of the thermoelectric material GeTe with high *zT* values larger than 2.5. However, there are still directions in which the GeTe system can make some breakthroughs:

1) Element doping enters the direction of multi-element high-entropy alloys, and the doping of high-entropy alloys is beneficial to optimizing the thermoelectric properties of GeTe in many aspects.

2) The doping of element types and components brings about the reduction of mobility caused by energy barriers and weakens the improvement of the power factor. Therefore, improving carrier mobility by decoupling electrical and thermal transport properties can be an effective way to further increase the *zT* value.

3) The research on material properties has tended to be saturated, and the research on GeTe-based thermoelectric devices is very urgent.

REFERENCES

A. Schlieper, Y. Feutelai, S.G. Fries, B. Legendre, & Blachnik, R. (1999). Thermodynamic Evaluation of the Germanium - Tellurium System. *Calphad, 23*, 1-18.

A. V. Kolobov, J. Tominaga, P. Fons, & Uruga, T. (2003). Local structure of crystallized GeTe films. *Appl. Phys. Lett., 82*, 382. doi:10.1063/1.1539926

Altenkirch, E. (1909). *Physikalische Zeitschrift, 10*, 560–580.

Altenkirch, E. (1911). *Physikalische Zeitschrift, 12*, 920.

Arvieu, C., Cassiopée Galy, Guen, E. L., & Lacoste, E. (2020). Relative Density of SLM-Produced Aluminum Alloy Parts: Interpretation of Results. *Journal of Manufacturing and Materials Processing 4*, 83. doi:10.3390/jmmp4030083

Bayikadi, K. S., Sankar, R., Wu, C. T., Xia, C. L., Chen, Y., Chen, L. C., . . . Chou, F. C. (2019). Enhanced thermoelectric performance of GeTe through in situ microdomain and Ge-vacancy control. *Journal of Materials Chemistry A, 7*(25), 15181-15189. doi:10.1039/c9ta03503f

Ben Amar, A., Kouki, A. B., & Cao, H. (2015). Power Approaches for Implantable Medical Devices. *Sensors (Basel), 15*(11), 28889-28914. doi:10.3390/s151128889

Bhat, D. K., & Shenoy, U. S. (2020). Resonance levels in GeTe thermoelectrics: zinc as a new multifaceted dopant. *New Journal of Chemistry, 44*(41), 17664-17670. doi:10.1039/d0nj04273k

Biswas, K., He, J., Blum, I. D., Wu, C. I., Hogan, T. P., Seidman, D. N., . . . Kanatzidis, M. G. (2012). High-performance bulk thermoelectrics with all-scale hierarchical architectures. *Nature, 489*(7416), 414-418. doi:10.1038/nature11439

Boschker, J. E., Wang, R., & Calarco, R. (2017). GeTe: a simple compound blessed with a plethora of properties. *CrystEngComm, 19*(36), 5324-5335. doi:10.1039/c7ce01040k

Brown, S. R., Kauzlarich, S. M., Gascoin, F., & Snyder, G. J. (2006). Yb14MnSb11: New High Efficiency Thermoelectric Material for Power Generation. Chemistry of Materials. *18*, 1873–1877.

Bu, Z., Li, W., Li, J., Zhang, X., Mao, J., Chen, Y., & Pei, Y. (2019). Dilute Cu2Te-alloying enables extraordinary performance of r-GeTe thermoelectrics. *Materials Today Physics, 9*. doi:10.1016/j.mtphys.2019.100096

Burton, M., Howells, G., Atoyo, J., & Carnie, M. (2022). Printed Thermoelectrics. *Adv Mater, 34*(18), e2108183. doi:10.1002/adma.202108183

Cao, T., Shi, X.-L., & Chen, Z.-G. (2023). Advances in the design and assembly of flexible thermoelectric device. *Progress in Materials Science, 131*. doi:10.1016/j.pmatsci.2022.101003

Chatterji, T., Kumar, C. M. N., & Wdowik, U. D. (2015). Anomalous temperature-induced volume contraction in GeTe. *Phys. Rev. B, 91*(5). doi:10.1103/PhysRevB.91.054110

Chen, W.-Y., Shi, X.-L., Zou, J., & Chen, Z.-G. (2022). Thermoelectric coolers for on-chip thermal management: Materials, design, and optimization. *Materials Science and Engineering: R: Reports, 151*. doi:10.1016/j.mser.2022.100700

Chen, Z.-G., Shi, X., Zhao, L.-D., & Zou, J. (2018). High-performance SnSe thermoelectric materials: Progress and future challenge. *Progress in Materials Science, 97*, 283-346. doi:10.1016/j.pmatsci.2018.04.005

Chen, Z., Zhang, X., & Pei, Y. (2018). Manipulation of Phonon Transport in Thermoelectrics. *Advanced Materials, 30*(17), e1705617. doi:10.1002/adma.201705617

Christian Pauly, Marcus Liebmann, Alessandro Giussani, Jens Kellner, Sven Just, Jaime Sánchez-Barriga, . . . Morgenstern, M. (2013). Evidence for topological band inversion of the phase change material $Ge_2Sb_2Te_5$. *Appl. Phys. Lett., 103*, 243109. doi:10.1063/1.4847715

Damon, D. H., Lubell, M. S., & Mazelsky, R. (1967). Nature of the defects in germanium telluride. *J. Phys. Chem. Solids 28*, 520–522. doi:10.1016/0022-3697(67)90323-X

Davide Beretta, Neophytos Neophytou, James M. Hodges, Mercouri G. Kanatzidis, Dario Narducci, Marisol Martin-Gonzalez, . . . Caironi*, M. (2019). Thermoelectrics. From history, a window on the future. *Materials Science and Engineering: R: Reports, 138*, 100501.

Dismukes, J. P., Ekstrom, L., Steigmeier, E. F., Kudman, I., & Beers, D. S. (1964). Thermal and Electrical Properties of Heavily Doped Ge-Si Alloys up to 1300°K. *Journal of Applied Physics, 35*(10), 2899-2907. doi:10.1063/1.1713126

Dong, J., Sun, F.-H., Tang, H., Pei, J., Zhuang, H.-L., Hu, H.-H., . . . Li, J.-F. (2019). Medium-temperature thermoelectric GeTe: vacancy suppression and band structure engineering leading to high performance. *Energy & Environmental Science, 12*(4), 1396-1403. doi:10.1039/c9ee00317g

Dresselhaus, M. S., Chen, G., Tang, M. Y., Yang, R. G., Lee, H., Wang, D. Z., . . . Gogna, P. (2007). New Directions for Low-Dimensional Thermoelectric Materials. *Advanced Materials, 19*(8), 1043-1053. doi:10.1002/adma.200600527

Edwards, A., Pineda, A., Schultz, P., Martin, M., Thompson, A., Hjalmarson, H., & Umrigar, C. (2006). Electronic structure of intrinsic defects in crystalline germanium telluride. *Physical Review B, 73*(4). doi:10.1103/PhysRevB.73.045210

Fahrnbauer, F., Souchay, D., Wagner, G., & Oeckler, O. (2015). High Thermoelectric Figure of Merit Values of Germanium Antimony Tellurides with Kinetically Stable Cobalt Germanide Precipitates. *Journal of the American Chemical Society, 137*(39), 12633-12638. doi:10.1021/jacs.5b07856

Fu, C., Bai, S., Liu, Y., Tang, Y., Chen, L., Zhao, X., & Zhu, T. (2015). Realizing high figure of merit in heavy-band p-type half-Heusler thermoelectric materials. *Nat Commun, 6*, 8144. doi:10.1038/ncomms9144

Gao, W., Liu, Z., Zhang, W., Sato, N., Guo, Q., & Mori, T. (2021). Improved thermoelectric performance of GeTe via efficient yttrium doping. *Appl. Phys. Lett., 118*(3). doi:10.1063/5.0038957

Girard, S. N., He, J., Li, C., Moses, S., Wang, G., Uher, C., . . . Kanatzidis, M. G. (2010). In situ nanostructure generation and evolution within a bulk thermoelectric material to reduce lattice thermal conductivity. *Nano Letters, 10*(8), 2825-2831. doi:10.1021/nl100743q

Haken, W. (1910). Annalen der Physik *832*, 291-336

He, J., & Tritt, T. M. (2017). Advances in thermoelectric materials research: Looking back and moving forward. *Science, 357*(6358). doi:10.1126/science.aak9997

He, R., Schierning, G., & Nielsch, K. (2018). Thermoelectric Devices: A Review of Devices, Architectures, and Contact Optimization. *Advanced Materials Technologies, 3*(4). doi:10.1002/admt.201700256

He, W., Wang, D., Wu, H., Xiao, Y., Zhang, Y., He, D., & … Zhao, L.-D. (2019). High thermoelectric performance in low-cost SnS0.91Se0.09 crystals. *Science, 365*(6460), 1418–1424. doi:10.1126/science.aax5123

Heremans, J. P., Jovovic, V., Toberer, E. S., Saramat, A., Kurosaki, K., Charoenphakdee, A., & Snyder, G. J. . (2008). Enhancement of Thermoelectric Efficiency in PbTe by Distortion of the Electronic Density of States. *Science, 321*, 554-557.

Hong, M., Chen, Z.-G., Yang, L., & Zou, J. (2016). Enhancing thermoelectric performance of Bi2Te3-based nanostructures through rational structure design. *Nanoscale, 8*(16), 8681-8686. doi:10.1039/c6nr00719h

Hong, M., Chen, Z.-G., & Zou, J. (2018). Fundamental and progress of Bi2Te3-based thermoelectric materials. *Chinese Physics B, 27*(4). doi:10.1088/1674-1056/27/4/048403

Hong, M., & Chen, Z. G. (2022). Chemistry in Advancing Thermoelectric GeTe Materials. *Acc Chem Res, 55*(21), 3178-3190. doi:10.1021/acs.accounts.2c00467

Hong, M., Chen, Z. G., Yang, L., Zou, Y. C., Dargusch, M. S., Wang, H., & Zou, J. (2018). Realizing zt of 2.3 in ge1-x-ysbxinyte via reducing the phase-transition temperature and introducing resonant energy doping. *Advanced Materials, 30*(11), 1705942. doi:10.1002/adma.201705942

Hong, M., Lyv, W., Li, M., Xu, S., Sun, Q., Zou, J., & & Chen, Z. G. (2020). Rashba Effect Maximizes Thermoelectric Performance of GeTe Derivatives. *Joule, 4*(9), 2030-2043. doi:10.1016/j.joule.2020.07.021

Hong, M., Wang, Y., Liu, W. D., Matsumura, S., Wang, H., Zou, J., & Chen, Z. G. (2018). Arrays of Planar Vacancies in Superior Thermoelectric $Ge_{1-x-y}Cd_xBi_yTe$ with band convergence. *Adv. Energy Mater., 8*(30), 1801837. doi:10.1002/aenm.201801837

Hong, M., Zou, J., & Chen, Z. G. (2019a). Thermoelectric GeTe with Diverse Degrees of Freedom Having Secured Superhigh Performance. *Advanced Materials, 31*(14). doi:10.1002/adma.201807071

Hong, M., Zou, J., & Chen, Z. G. (2019b). Thermoelectric GeTe with Diverse Degrees of Freedom Having Secured Superhigh Performance. *Adv. Mater., 31*(14). doi:10.1002/adma.201807071

Hu, L., Wu, H., Zhu, T., Fu, C., He, J., Ying, P., & Zhao, X. (2015). Tuning Multiscale Microstructures to Enhance Thermoelectric Performance of n-Type Bismuth-Telluride-Based Solid Solutions. *Advanced Energy Materials, 5*(17). doi:10.1002/aenm.201500411

Huang, B., & Robertson, J. (2012). Nature of defects and gap states in GeTe model phase change materials. *Physical Review B, 85*(12). doi:10.1103/PhysRevB.85.125305

Huang, L., Lin, S., Xu, Z., Zhou, H., Duan, J., Hu, B., & Zhou, J. (2019). Fiber-Based Energy Conversion Devices for Human-Body Energy Harvesting. *Advanced Materials, 32*(5). doi:10.1002/adma.201902034

Jo, S., Choo, S., Kim, F., Heo, S. H., & Son, J. S. (2019). Ink Processing for Thermoelectric Materials and Power-Generating Devices. *Adv Mater, 31*(20), e1804930. doi:10.1002/adma.201804930

Joshi, G., Lee, H., Lan, Y., Wang, X., Zhu, G., Wang, D., ··· Ren, Z. . (2008). Enhanced Thermoelectric Figure-of-Merit in Nanostructured p-type Silicon Germanium Bulk Alloys. *Nano Letters, 8*, 4670–4674.

Kim, Y. J., Zhao, L. D., Kanatzidis, M. G., & & Seidman, D. N. (2017). Analysis of Nanoprecipitates in a Na-Doped PbTe–SrTe Thermoelectric Material with a High Figure of Merit. *ACS Appl. Mater. Interfaces, 9*(26), 21791-21797. doi:10.1021/acsami.7b04098

Kishore, R. A., Nozariasbmarz, A., Poudel, B., Sanghadasa, M., & Priya, S. (2019). Ultra-high performance wearable thermoelectric coolers with less materials. *Nature Communications, 10*(1). doi:10.1038/s41467-019-09707-8

Kusrini, E., Hakim, I. I., Putra, N., Usman, M., Juwono, F. H., Yatim, A., & Setiawan, E. A. (2018). Analysis of the use of thermoelectric generator and heat pipe for waste heat utilization. *E3S Web of Conferences, 67*. doi:10.1051/e3sconf/20186702057

Lafaurie Ponce, L. G., Chejne, F., Ramirez Aristeguieta, L. M., Gómez, C. A., & Múnera Cano, A. F. (2019). Predicting a thermal stimulator's heating/cooling rate for medical applications. *Applied Thermal Engineering, 163*. doi:10.1016/j.applthermaleng.2019.114376

Levin, E. M., Besser, M. F., & Hanus, R. (2013). Electronic and thermal transport in gete: A versatile base for thermoelectric materials. *Journal of Applied Physics, 114*(8), 083713. doi:10.1063/1.4819222

Li, J. Q., Xie, Y. C., Zhang, C. X., Ma, K., Liu, F. S., Ao, W. Q., . . . Zhang, C. H. (2019). Stacking Fault-Induced Minimized Lattice Thermal Conductivity in the High-Performance GeTe-Based Thermoelectric Materials upon Bi2Te3 Alloying. *Acs Applied Materials & Interfaces, 11*(22), 20064-20072. doi:10.1021/acsami.9b04984

Li, N., He, W., Li, C., Wang, G., Wang, G., Zhou, X., & Lu, X. (2021). The role of electronegativity in the thermoelectric performance of GeTe–I–V–VI2 solid solutions. *Journal of Materials Chemistry A*. doi:10.1039/d0ta10268g

Liebl, J., S. Neugebauer, A. Eder, M. Linde, B. Mazar, and W. Stütz (2009). The Thermoelectric Generator from BMW is Making Use of Waste Heat. *MTZ Worldwide, 70(4)*, 4-11.

Liu, W.-S., Zhang, B.-P., Li, J.-F., & Zhao, L.-D. (2007). Thermoelectric property of fine-grained CoSb3skutterudite compound fabricated by mechanical alloying and spark plasma sintering. *Journal of Physics D: Applied Physics, 40*(2), 566-572. doi:10.1088/0022-3727/40/2/035

Liu, W. D., Wang, D. Z., Liu, Q., Zhou, W., Shao, Z., & Chen, Z. G. (2020). High-Performance GeTe - Based Thermoelectrics: from Materials to Devices. *Advanced Energy*

Materials, 10(19). doi:10.1002/aenm.202000367

Liu, Z., Gao, W., Zhang, W., Sato, N., Guo, Q., & Mori, T. (2020). High Power Factor and Enhanced Thermoelectric Performance in Sc and Bi Codoped GeTe: Insights into the Hidden Role of Rhombohedral Distortion Degree. *Advanced Energy Materials, 10*(42). doi:10.1002/aenm.202002588

Nisar, A., Zhang, C., Boesl, B., & Agarwal, A. (2021). Unconventional Materials Processing Using Spark Plasma Sintering. *Ceramics, 4*(1), 20-39. Retrieved from https://www.mdpi.com/2571-6131/4/1/3

Nshimyimana, E., Hao, S., Su, X., Zhang, C., Liu, W., Yan, Y., . . . Tang, X. (2020). Discordant nature of Cd in GeTe enhances phonon scattering and improves band convergence for high thermoelectric performance. *Journal of Materials Chemistry A, 8*(3), 1193-1204. doi:10.1039/c9ta10436d

Park, S. H., Jin, Y., Cha, J., Hong, K., Kim, Y., Yoon, H., . . . Chung, I. (2018). High-Power-Density Skutterudite-Based Thermoelectric Modules with Ultralow Contact Resistivity Using Fe–Ni Metallization Layers. *ACS Applied Energy Materials, 1*(4), 1603-1611. doi:10.1021/acsaem.8b00064

Pei, Y., LaLonde, A. D., Heinz, N. A., Shi, X., Iwanaga, S., Wang, H., . . . Snyder, G. J. (2011). Stabilizing the Optimal Carrier Concentration for High Thermoelectric Efficiency. *Advanced Materials, 23*(47), 5674-5678. doi:10.1002/adma.201103153

Pei, Y., May, A. F., & Snyder, G. J. (2011). Self-Tuning the Carrier Concentration of PbTe/Ag2Te Composites with Excess Ag for High Thermoelectric Performance. *Adv. Energy Mater., 1*(2), 291-296. doi:10.1002/aenm.201000072

Pei, Y., Wang, H., & Snyder, G. J. (2012). Band Engineering of Thermoelectric Materials. *Advanced Materials, 24*(46), 6125-6135. doi:10.1002/adma.201202919

Peltier, J. C. A. (1834). *Ann. Chim. Phys,, 56*, 371-386.

Perumal, S., Roychowdhury, S., & Biswas, K. (2016). High performance thermoelectric materials and devices based on GeTe. *J. Mater. Chem. C, 4*(32), 7520-7536. doi:10.1039/c6tc02501c

Perumal, S., Roychowdhury, S., & Biswas, K. (2016). Reduction of thermal conductivity through nanostructuring enhances the thermoelectric figure of merit in $Ge_{1-x}Bi_xTe$. *Inorg. Chem. Front., 3*(1), 125-132. doi:10.1039/c5qi00230c

Perunnal, S., Roychowdhury, S., Negi, D. S., Datta, R., & Biswas, K. (2015). High Thermoelectric Performance and Enhanced Mechanical Stability of p-type $Ge_{1-x}Sb_xTe$. *Chem. mater., 27*(20), 7171–7178. doi:10.1021/acs.chemmater.5b03434

Physik, E. L.-A. d. (1838). Wiley Online Libr.

Prilepo, Y. P., Pustovalov, A. A., Sinyavskiy, V. V., Sudak, N. M., & Yatsenko, O. B. (2012). Problems of designing radioisotope thermoelectric power generators with a service life of decades for use in outer space exploration vehicles. *Thermal Engineering, 59*(13), 981-983. doi:10.1134/s004060151213006x

Roychowdhury, S., Samanta, M., Perumal, S., & Biswas, K. (2018). Germanium chalcogenide thermoelectrics: Electronic structure modulation and low lattice thermal conductivity. *Chemistry of Materials, 30*(17), 5799-5813.

doi:10.1021/acs.chemmater.8b02676

Salvador, J. R., Cho, J. Y., Ye, Z., Moczygemba, J. E., Thompson, A. J., Sharp, J. W., . . . Meisner, G. P. (2012). Thermal to Electrical Energy Conversion of Skutterudite-Based Thermoelectric Modules. *Journal of Electronic Materials, 42*(7), 1389-1399. doi:10.1007/s11664-012-2261-9

Salvador, J. R., Yang, J., Shi, X., Wang, H., & Wereszczak, A. A. (2009). Transport and mechanical property evaluation of (agsbte)(1-x)(gete)(x) (x=0.80, 0.82, 0.85, 0.87, 0.90). *Journal of Solid State Chemistry, 182*(8), 2088-2095. doi:10.1016/j.jssc.2009.05.024

Samanta, M., Roychowdhury, S., Ghatak, J., Perumal, S., & Biswas, K. (2017). Ultrahigh average thermoelectric figure of merit, low lattice thermal conductivity and enhanced microhardness in nanostructured (gete)(x)(agsbse2)(100-x). *Chemistry-a European Journal, 23*(31), 7438-7443. doi:10.1002/chem.201701480

Santhanam, S. C., A. K. Mater. Res. Bull. 1981, 16, . (1981). Transport properties of SnTe interpreted by means of a two valence band model. *Materials Research Bulletin, 16*, 911−917.

Shakouri, A. (2011). Recent Developments in Semiconductor Thermoelectric Physics and Materials. *Annual Review of Materials Research, 41*(1), 399-431. doi:10.1146/annurev-matsci-062910-100445

Sharma, S., Dwivedi, V. K., & Pandit, S. N. (2014). A Review of Thermoelectric Devices for Cooling Applications. *International Journal of Green Energy, 11*(9), 899-909. doi:10.1080/15435075.2013.829778

Shi, X. L., Zou, J., & Chen, Z. G. (2020). Advanced Thermoelectric Design: From Materials and Structures to Devices. *Chem Rev, 120*(15), 7399-7515. doi:10.1021/acs.chemrev.0c00026

Shuai, J., Sun, Y., Tan, X., & Mori, T. (2020). Manipulating the Ge Vacancies and Ge Precipitates through Cr Doping for Realizing the High-Performance GeTe Thermoelectric Material. *Small, 16*(13), e1906921. doi:10.1002/smll.201906921

Shuai, J., Tan, X. J., Guo, Q., Xu, J. T., Gellé, A., Gautier, R., . . . Mori, T. (2019). Enhanced thermoelectric performance through crystal field engineering in transition metal–doped GeTe. *Mater. Today Phys. , 9*, 100094. doi:10.1016/j.mtphys.2019.100094

Siegert, K. S., Lange, F. R. L., Sittner, E. R., Volker, H., Schlockermann, C., Siegrist, T., & Wuttig, M. (2015). Impact of vacancy ordering on thermal transport in crystalline phase-change materials. *Reports on Progress in Physics, 78*(1). doi:10.1088/0034-4885/78/1/013001

Snyder, G. J., Snyder, A. H., Wood, M., Gurunathan, R., Snyder, B. H., & Niu, C. (2020). Weighted Mobility. *Adv Mater, 32*(25), e2001537. doi:10.1002/adma.202001537

Srinivasan, B., Gelle, A., Gucci, F., Boussard-Pledel, C., Fontaine, B., Gautier, R., . . . Bureau, B. (2019a). Realizing a stable high thermoelectric zT ~ 2 over a broad temperature range in $\mathrm{Ge}_{1-x-y}\mathrm{Ga}_x\mathrm{Sb}_y\mathrm{Te}$ *via* band engineering and hybrid flash-SPS processing. *Inorg. Chem. Front., 6*(1), 63-73. doi:10.1039/c8qi00703a

Srinivasan, B., Gelle, A., Gucci, F., Boussard-Pledel, C., Fontaine, B., Gautier, R., . . . Bureau,

B. (2019b). Realizing a stable high thermoelectric zt similar to 2 over a broad temperature range in ge1-x-ygaxsbyte via band engineering and hybrid flash-sps processing. *Inorganic Chemistry Frontiers, 6*(1), 63-73. doi:10.1039/c8qi00703a

Sun, H., Lu, X., Chi, H., Morelli, D. T., & Uher, C. (2014). Highly efficient (in2te3)(x)(gete)(3-3x) thermoelectric materials: A substitute for tags. *Physical Chemistry Chemical Physics, 16*(29), 15570-15575. doi:10.1039/c4cp01294a

Sun, T., Zhou, B., Zheng, Q., Wang, L., Jiang, W., & Snyder, G. J. (2020). Stretchable fabric generates electric power from woven thermoelectric fibers. *Nat Commun, 11*(1), 572. doi:10.1038/s41467-020-14399-6

Tan, G., Shi, F., Hao, S., Chi, H., Zhao, L. D., Uher, C., . . . Kanatzidis, M. G. (2015). Codoping in SnTe: Enhancement of Thermoelectric Performance through Synergy of Resonance Levels and Band Convergence. *Journal of the American Chemical Society, 137*(15), 5100-5112. doi:10.1021/jacs.5b00837

Tan, H., Zhang, B., Wang, G. Y., Chen, Y. J., Shen, X. C., Guo, L. J., . . . Zhou, X. Y. (2019). Rapid preparation of ge0.9sb0.1te1+x via unique melt spinning: Hierarchical microstructure and improved thermoelectric performance. *Journal of Alloys and Compounds, 774*, 129-136. doi:10.1016/j.jallcom.2018.09.144

Tan, X., Wang, H., Liu, G., Noudem, J. G., Hu, H., Xu, J., . . . Jiang, J. (2018). Designing band engineering for thermoelectrics starting from the periodic table of elements. *Materials Today Physics, 7*, 35-44. doi:10.1016/j.mtphys.2018.10.004

Tang, Y., Gibbs, Z. M., Agapito, L. A., Li, G., Kim, H., Nardelli, M. B., . . . Snyder, G. J. (2015). Convergence of multi-valley bands as the electronic origin of high thermoelectric performance in CoSb3 skutterudites. *Nat. Mater., 14*, 1223-1228. doi:10.1038/nmat4430

Tang, Y., Hanus, R., Chen, S. W., & Snyder, G. J. (2015). Solubility design leading to high figure of merit in low-cost Ce-CoSb3 skutterudites. *Nat Commun, 6*, 7584. doi:10.1038/ncomms8584

Thomson, W. (1851). On the Dynamical Theory of Heat. Trans. *R. Soc. Edinburgh: Earth Sci., 3*, 91–98.

Wang, X. W., Lee, H., Lan, Y. C., Zhu, G. H., Joshi, G., Wang, D. Z., . . . Ren, Z. F. (2008). Enhanced thermoelectric figure of merit in nanostructured n-type silicon germanium bulk alloy. *Applied Physics Letters, 93*(19). doi:10.1063/1.3027060

Wang, Y., Yang, L., Shi, X. L., Shi, X., Chen, L., Dargusch, M. S., . . . Chen, Z. G. (2019). Flexible Thermoelectric Materials and Generators: Challenges and Innovations. *Advanced Materials, 31*(29). doi:10.1002/adma.201807916

Wu, D., Xie, L., Xu, X., & He, J. (2019). High Thermoelectric Performance Achieved in GeTe–Bi2Te3 Pseudo‐Binary via Van der Waals Gap‐Induced Hierarchical Ferroelectric Domain Structure. *Advanced Functional Materials, 29*(18). doi:10.1002/adfm.201806613

Wu, H. J., Zhao, L. D., Zheng, F. S., Wu, D., Pei, Y. L., Tong, X., . . . He, J. Q. (2014). Broad temperature plateau for thermoelectric figure of merit ZT>2 in phase-separated

PbTe0.7S0.3. *Nat. Commun., 5*, 4515. doi:10.1038/ncomms5515

Wu, L., Li, X., Wang, S., Zhang, T., Yang, J., Zhang, W., . . . Yang, J. (2017). Resonant level-induced high thermoelectric response in indium-doped GeTe. *NPG Asia Materials, 9*(1), e343-e343. doi:10.1038/am.2016.203

Xie, W., Tang, X., Yan, Y., Zhang, Q., & Tritt, T. M. (2009). Unique nanostructures and enhanced thermoelectric performance of melt-spun BiSbTe alloys. *Applied Physics Letters, 94*(10). doi:10.1063/1.3097026

Xie, W., Weidenkaff, A., Tang, X., Zhang, Q., Poon, J., & Tritt, T. M. (2012). Recent Advances in Nanostructured Thermoelectric Half-Heusler Compounds. *Nanomaterials (Basel), 2*(4), 379-412. doi:10.3390/nano2040379

Yang, L., Chen, Z.-G., Han, G., Hong, M., Zou, Y., & Zou, J. (2015). High-performance thermoelectric Cu2Se nanoplates through nanostructure engineering. *Nano Energy, 16*, 367-374. doi:10.1016/j.nanoen.2015.07.012

Yin, L. C., Liu, W. D., Li, M., Sun, Q., Gao, H., Wang, D. Z., . . . Chen, Z. G. (2021). High Carrier Mobility and High Figure of Merit in the CuBiSe2 Alloyed GeTe. *Advanced Energy Materials, 11*(45). doi:10.1002/aenm.202102913

Yu, Y., Xu, X., Wang, Y., Jia, B., Huang, S., Qiang, X., . . . He, J. (2022). Tunable quantum gaps to decouple carrier and phonon transport leading to high-performance thermoelectrics. *Nat Commun, 13*(1), 5612. doi:10.1038/s41467-022-33330-9

Yue, L., Cui, W., Zheng, S., Wu, Y., Wang, L., Bai, P., & Dong, X. (2020). Band Engineering and Thermoelectric Performance Optimization of p-Type GeTe-Based Alloys through Ti/Sb Co-Doping. *J. Phys. Chem. C, 124*(10), 5583-5590. doi:10.1021/acs.jpcc.0c00045

Yue, L., Fang, T., Zheng, S. Q., Cui, W. L., Wu, Y., Chang, S. Y., . . . Zhao, H. Z. (2019). Cu/Sb Codoping for Tuning Carrier Concentration and Thermoelectric Performance of GeTe-Based Alloys with Ultralow Lattice Thermal Conductivity. *ACS Appl. Energy Mater., 2*(4), 2596-2603. doi:10.1021/acsaem.8b02213

Zhang, Q., Liao, B., Lan, Y., Lukas, K., Liu, W., Esfarjani, K., . . . Ren, Z. (2013). High thermoelectric performance by resonant dopant indium in nanostructured SnTe. *Proc. Natl. Acad. Sci. U.S.A., 110*(33), 13261-13266. doi:10.1073/pnas.1305735110

Zhang, W., Thiess, A., Zalden, P., Zeller, R., Dederichs, P. H., Raty, J. Y., . . . Mazzarello, R. (2012). Role of vacancies in metal-insulator transitions of crystalline phase-change materials. *Nat Mater, 11*(11), 952-956. doi:10.1038/nmat3456

Zhang, X., Bu, Z., Lin, S., Chen, Z., Li, W., & Pei, Y. (2020). GeTe Thermoelectrics. *Joule, 4*(5), 986-1003. doi:10.1016/j.joule.2020.03.004

Zhang, X., Bu, Z., Shi, X., Chen, Z., Lin, S., Shan, B., . . . Pei, Y. (2020). Electronic quality factor for thermoelectrics. *Sci Adv, 6*(46). doi:10.1126/sciadv.abc0726

Zhao, L. D., Tan, G., Hao, S., He, J., Pei, Y., Chi, H., ... & Uher, C. (2016). Ultrahigh power factor and thermoelectric performance in hole-doped single-crystal SnSe. *Science, 351*, 141-144.

Zhu, T., Hu, L., Zhao, X., & He, J. (2016). New Insights into Intrinsic Point Defects in V2VI3 Thermoelectric Materials. *Adv Sci (Weinh), 3*(7), 1600004.

doi:10.1002/advs.201600004

APPENDIX A

This appendix A is attached as the supporting information (published) for Paper 1 on Chapter 4: THE EFFECT OF RARE EARTH ELEMENT DOPING ON THERMOELECTRIC PROPERTIES OF GETE

Supporting Information

The effect of rare earth element doping on thermoelectric properties of GeTe

Wan-Yu Lyu,[a,b] Wei-Di Liu,[b] Meng Li,[b] Min Hong,[a,b] Kai Guo,[c,*] Jun Luo,[d] Juanjuan Xing,[d] Qiang Sun,[b] Shengduo Xu,[b] Jin Zou,[b,e] Zhi-Gang Chen[f,*]

[a]Centre for Future Materials, University of Southern Queensland, Springfield, Queensland 4300, Australia.

[b]School of Mechanical and Mining Engineering, The University of Queensland, Brisbane, Queensland 4072, Australia.

[c]School of Physics and Materials Science, Guangzhou University, Guangzhou 510006, China

[d]School of Materials Science and Engineering, Shanghai University, 99 Shangda Road, Shanghai 200444, China

[e]Centre for Microscopy and Microanalysis, The University of Queensland, Brisbane, Queensland 4072, Australia.

[f]School of Chemistry and Physics, Queensland University of Technology, Brisbane, Queensland 4001, Australia

Email: zhigang.chen@qut.edu.au (ZGC); kai.guo@gzhu.edu.cn (KG)

Key words: GeTe, rare earth elements, lattice thermal conductivity, *zT*

1. Experimental section

1.1 Synthesis

Melting and quenching method was mostly used to prepare thermoelectric materials in many systems. Raw materials, including Ge (99.999%, Sigma-Aldrich, Australia), Te (99.999%, Sigma-Aldrich, Australia), Eu (99.99%, Sigma-Aldrich, United States), Gd (99.999%, Alfa-Aesar, United States), Er (99.999%, Alfa-Aesar, United States), and Tm (99.999%, Alfa-Aesar, United States), were weighed following the nominal compositions GeTe and $Ge_{0.98}RE_{0.02}Te$ (RE=Eu, Gd, Er, Tm). The mixtures were putted in quartz ampules marked 1 to 5 and then sealed in quartz ampules with high vacuum degree. These mixed-samples were heated in 1223 K at muffle furnace for 24 hours followed by water quenching. After that, the obtained samples were annealed at 873 K for 3 days. The resultant products were further ground into powders in an agate mortar and then sintered into pellets by SPS (Spark Plasma Sintering, 65 Mpa, 673K, 5min) for performance measurement. Thus, the high density (>97%, see Table S1 RE substituted GeTe bulks were obtained.

1.2 Characterization

X-ray diffraction (XRD, Bruker, United States, Cu K_α radiation with a wavelength of 1.5418 Å, $10° \leq 2\theta \leq 80°$, step with 0.02°) was used to characterize the crystal structures of as-prepared samples. The morphologies and compositions of GeTe and $Ge_{0.98}RE_{0.02}Te$ (RE=Eu, Gd, Er, Tm) was characterized by Field-emission scanning electron microscope (FE-SEM, JSM-7001F, JEOL, Japan) equipped with energy dispersive spectrum (EDS) detector.

1.3 Thermoelectrical Property Measurement

Electrical transport properties, including S and σ, of the sintered pellets were simultaneously measured by ZEM-3 (ULVAC Technologies, Inc., Japan). Thermal conductivity κ_{TOTAL} is calculated by $\kappa_{TOTAL} = D \times C_p \times \rho$, where D is the thermal diffusivity coefficient measured by the laser flash diffusivity apparatus (LFA 457, Netzsch, Gemany), C_p is the specific heat estimated from the Dulong-Petit approximation, ρ is the pellet densities measured by Archimedes method. The Hall coefficient (R_H) was measured based on Van der Paw technique to further analysis the transport properties of GeTe and $Ge_{0.98}RE_{0.02}Te$ (RE=Eu, Gd, Er, Tm). The n_H and μ_H were obtained through the equation $n_H = 1/(eR_H)$, and $\mu_H = \sigma R_H$, where e is the electron charge.

2. Basic characteristics of GeTe and $Ge_{0.98}RE_{0.02}Te$ (RE=Eu, Gd, Er, Tm)

2.1. Composition and density of GeTe and $Ge_{0.98}RE_{0.02}Te$ (RE=Eu, Gd, Er, Tm)

As shown in **Table S1**, the composition of GeTe and $Ge_{0.98}RE_{0.02}Te$ (RE=Eu, Gd, Er, Tm) was characterized by SEM-EDS mapping.

Table S1. The nominated composition, real composition confirmed by EDS mapping result, density and relative density of pristine GeTe and $Ge_{0.98}RE_{0.02}Te$ (RE=Eu, Gd, Er, Tm) at room temperature.

Nominated composition	Real composition (by EDS mapping data)	Density (g cm^{-3})	Relative density (%)
GeTe	$Ge_{1.02}Te$	6.0924	98%
$Ge_{0.98}Eu_{0.02}Te$	$Ge_{1.02}Eu_{0.008}Te$	6.1554	98.8%
$Ge_{0.98}Gd_{0.02}Te$	$Ge_{1.02}Gd_{0.008}Te$	6.1077	97.8%
$Ge_{0.98}Er_{0.02}Te$	$Ge_{1.02}Er_{0.012}Te$	6.0546	97.1%
$Ge_{0.98}Tm_{0.02}Te$	$Ge_{1.03}Tm_{0.018}Te$	6.0991	97.8%

Figure S1 shows the EDS maps of Ge and Te for $Ge_{0.98}RE_{0.02}Te$ (RE=Eu, Gd, Er, Tm), where small amount of Ge precipitates can be clearly observed.

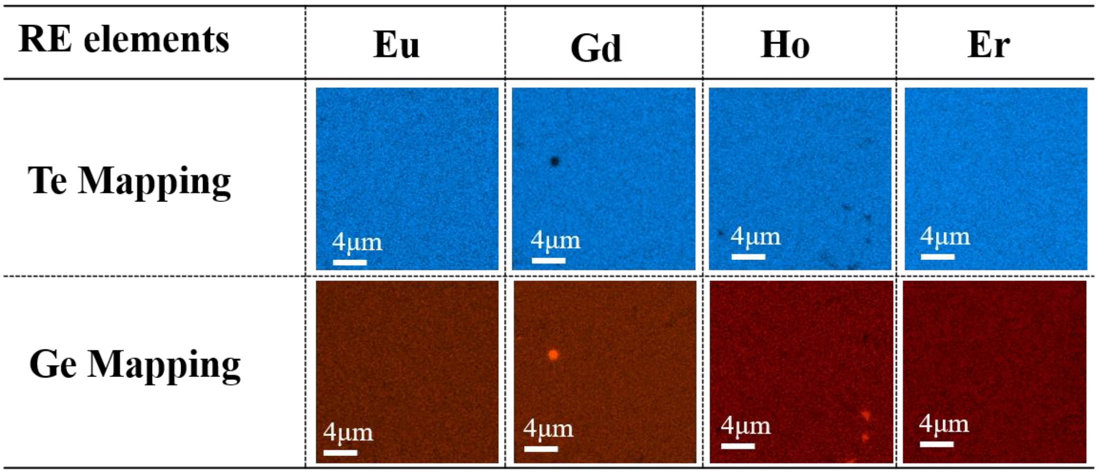

Figure S1. the EDS mapping result of Ge and Te for $Ge_{0.98}RE_{0.02}Te$ (RE=Eu, Gd, Er, Tm).

2.2. Effective magnetic moment

The effective magnetic moment (μ_J) of these rare earth elements was calculated below:

$$\mu_J = g_J\sqrt{J(J+1)}\mu_B \tag{1}$$

Where g_J means Landé factor, J represents total angular momentum, μ_B is the Bohr magneton.

As shown in **Table S2**, the REs with unpaired 4f electrons have large local magnetic moment, which can contribute to higher *S* through the magnetic contribution from magnetic atoms.

Table S2. μ_J, and experimental μ_J of rare earth elements Eu, Gd, Er, Tm.

Rare earth elements	μ_J (μ_B)	Experimental μ_J (μ_B)
Eu	0	3.4
Gd	7.94	8.0
Er	9.58	9.5
Tm	7.56	7.3

2.3. Electronegativity (χ) and atomic radius (R) of Ge, Eu, Gd, Er, Tm.

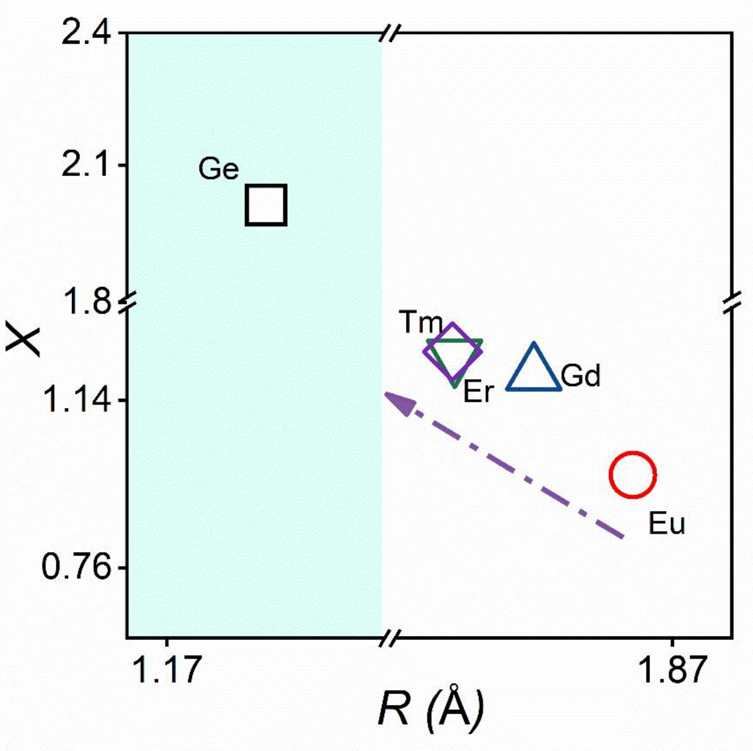

Figure S2. χ and R of Ge, Eu, Gd, Er, Tm.

3. Electrical transport property

3.1. Electrical transport properties

Table S3. Electrical transport properties of pristine GeTe and $Ge_{0.98}RE_{0.02}Te$ (RE=Eu, Gd, Er, Tm) at room temperature.

Nominated composition	n_H (10^{21} cm^{-3})	μ_H (cm^2 V^{-1} s^{-1})	σ (S cm^{-1})	S (μV K^{-1})	m^* (m_0)
GeTe	1.45	30	7199	37.2	2.35
$Ge_{0.98}Eu_{0.02}Te$	1.53	23	6849	43.4	2.82
$Ge_{0.98}Gd_{0.02}Te$	1.58	18	6211	41.4	2.75
$Ge_{0.98}Er_{0.02}Te$	1.67	17	5494	43.2	2.98
$Ge_{0.98}Tm_{0.02}Te$	1.49	19	5650	40.8	2.6

3.2. Piserokoline relationship

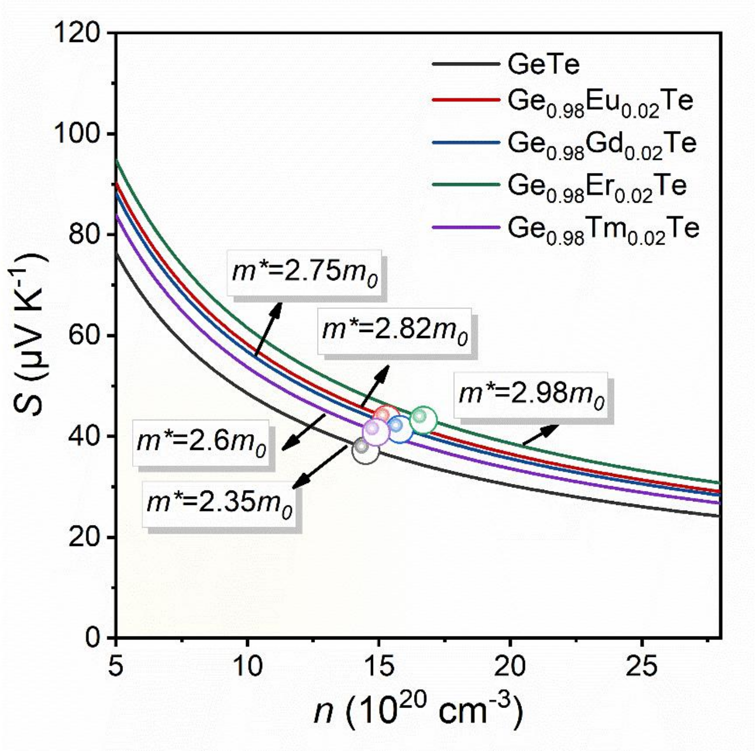

Figure S3. *n* dependent *S* of as-sintered GeTe, and $Ge_{0.98}RE_{0.02}Te$ (RE=Eu, Gd, Er, Tm).

4. Lattice thermal conductivity (κ_L) and electrical thermal conductivity (κ_E) calculation

The lattice thermal conductivity κ_{L} is estimated by deducting κ_{E} from measured κ_{TOTAL}:

$$\kappa_{\mathrm{L}} = \kappa_{\mathrm{TOTAL}} - \kappa_{\mathrm{E}} \tag{2}$$

The κ_{E} is calculated following the Wiedemann−Franz law formula:

$$\kappa_{\mathrm{E}} = L\sigma T \tag{3}$$

where L is the Lorenz number, σ represents the electrical conductivity, and T is the absolute temperature. The L is calculated using the following equation proposed by Kim *et al*. based on single parabolic band assumption[1]:

$$L = 1.5 + exp\frac{-|S|}{116} \tag{4}$$

where S is the Seebeck coefficient.

As shown in **Figure S4**, κ_{E} was reduced with increasing atomic number due to decreased σ.

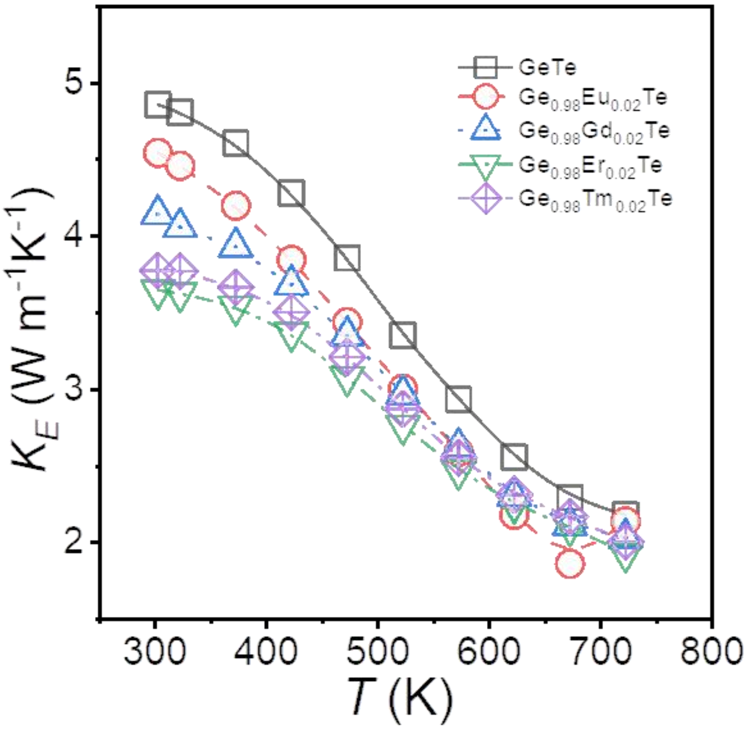

Figure S4. κ_E of pristine GeTe and $Ge_{0.98}RE_{0.02}Te$ (RE=Eu, Gd, Er, Tm).

5. Comparation of zT_{ave}

The zT_{ave} of different element doping in GeTe according to doping content was shown in **Figure S5**. Due to the different synthesis methods, and different χ and R of different doping elements, the solid solubility of In, Cr, Cd, Ti, Sc doped GeTe are different, which presents different influence on zT_{ave}.

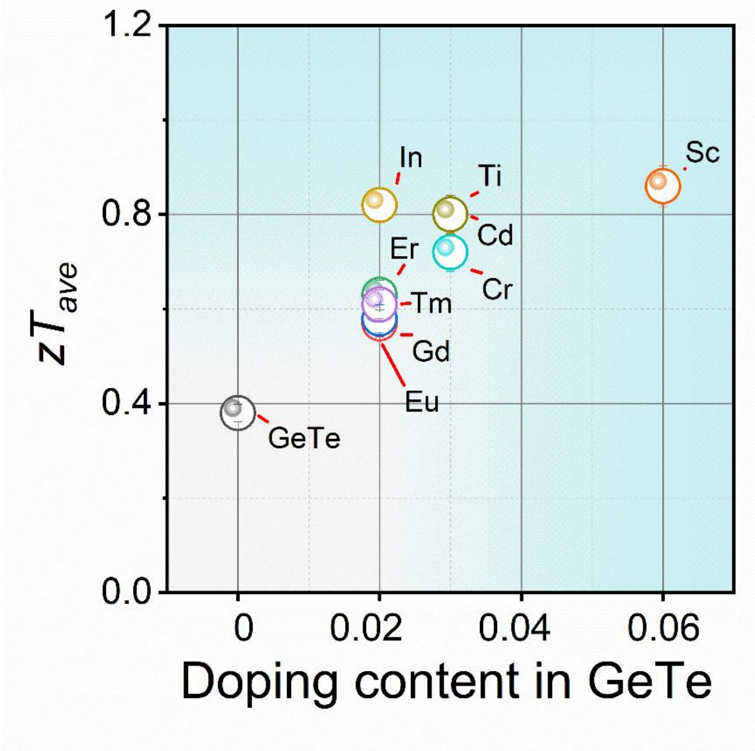

Figure S5. The zT_{ave} of single elements doped GeTe [2-6].

6. Theoretical κ_L of $Ge_{0.98}RE_{0.02}Te$ (RE=Eu, Gd, Er, Tm)

Element substitution can cause lattice fluctuation and led to a disorder of the crystal matrix, which can be expressed by the Callaway[7] and Klmen[8] model, which has been used by many thermoelectric systems[9-11]. The lattice distribution can be evaluated by κ_L / κ_{L0}, which κ_{L0} represents the lattice thermal conductivity of pristine GeTe, κ_L is calculated lattice thermal conductivity of REs substituted GeTe.

$$\frac{\kappa_L}{\kappa_{L0}} = \frac{tan^{-1}(u)}{u} \tag{5}$$

$$u^2 = \frac{\pi^2 \theta_D \Omega}{h {v_s}^2} \kappa_{L0} \Gamma_{tot} \tag{6}$$

where u, Ω, υ_s, θ_D, and Γ_{TOT} are the disorder scaling parameter, the average volume per atom, the sound velocity, the Debye temperature, and the experimental disorder scattering parameter, respectively. Γ_{TOT} can be derived from measured κ_L. Total disorder parameter (Γ_{TOT}) including strain-field fluctuation (Γ_S), and mass fluctuation (Γ_M) was calculated, where $\Gamma_{TOT} = \Gamma_M + \Gamma_S$. Where the scattering parameters Γ_M and Γ_S are due to mass fluctuation, and strain-field fluctuation, respectively. For the binary GeTe, Γ_M and Γ_S are given by equal (7-8), where, M1, M2, and M3 are the atomic mass of Ge, REs, and Te, respectively; r_1 and r_2 are the atomic radius of Ge and REs, respectively; x is the content of RE; and ε is regarded as a phenomenological adjustable parameter.

$$\Gamma_M = \frac{1}{2}(\frac{\overline{M}}{\overline{\overline{M}}})x(1-x)(\frac{M_1-M_2}{\overline{M}})^2 \quad (7)$$

$$\Gamma_S = \frac{1}{2}(\frac{\overline{M}}{\overline{\overline{M}}})x(1-x)\varepsilon(\frac{r_1-r_2}{\overline{r}})^2 \quad (8)$$

$$\overline{M} = M_1x + M_2(1-x) \quad (9)$$

$$\overline{\overline{M}} = \frac{1}{2}(\overline{M} + M_3) \quad (10)$$

$$\overline{r} = r_1x + r_2(1-x) \quad (11)$$

The experiment disorder scattering parameter, Γ_{EXP}, can also be calculated by the formula (5-6) with experiment lattice thermal conductivity κ_L of $Ge_{0.98}RE_{0.02}Te$ (RE=Eu, Gd, Er, Tm). And the experiment Γ_S can be calculated according to the assumption

$$\Gamma_{EXP} = \Gamma_M + \Gamma_S \quad (12)$$

The results and calculation parameters were shown in **Table S4**and **Table S5**

Table S4. Room temperature lattice thermal conductivity, κ_L, disorder scaling parameter, u, disorder scattering parameters Γ_{EXP}, Γ_M , Γ_S, and the strain field related adjustable parameter ε.

Samples	κ_L (W/m/K)	u	Γ_{EXP}	Γ_M	Γ_S	ε
GeTe	3.37	N	N	N	N	N
$Ge_{0.98}Eu_{0.02}Te$	2.99	0.67	0.0089	0.0055	0.0034	2.95
$Ge_{0.98}Gd_{0.02}Te$	2.73	0.91	0.0165	0.0062	0.0102	9.03
$Ge_{0.98}Er_{0.02}Te$	2.08	1.66	0.0548	0.0078	0.0471	42.58
$Ge_{0.98}Tm_{0.02}Te$	1.99	1.8	0.0645	0.008	0.0564	51.11

Table S5. Parameters for phonon modeling calculation.

Parameter	Description	Values

υ_L	Longitudinal phonon velocity (m s^{-1})	2930
υ_T	Transverse phonon velocity (m s^{-1})	1780
υ_S	Average phonon velocity	1967
θ_D	Acoustic Debye temperature (K)	195
Ω	Average atomic volume (m^{-3})	$2.708*10^{-29}$
$\bar{M}$	Average atomic mass (kg)	$1.66*10^{-25}$
γ	Grüneisen parameter	1.56

Reference

[1] H.-S. Kim, Z.M. Gibbs, Y. Tang, H. Wang, G.J. Snyder, Characterization of Lorenz number with Seebeck coefficient measurement, APL Mater. 3 (2015) 041506. https://doi.org/10.1063/1.4908244.

[2] L. Wu, X. Li, S. Wang, T. Zhang, J. Yang, W. Zhang, L. Chen, J. Yang, Resonant level-induced high thermoelectric response in indium-doped GeTe, NPG Asia Materials 9 (2017) e343-e343. https://doi.org/10.1038/am.2016.203.

[3] J. Shuai, Y. Sun, X. Tan, T. Mori, Manipulating the Ge Vacancies and Ge Precipitates through Cr Doping for Realizing the High-Performance GeTe Thermoelectric Material, Small 16 (2020) e1906921. https://doi.org/10.1002/smll.201906921.

[4] E. Nshimyimana, S. Hao, X. Su, C. Zhang, W. Liu, Y. Yan, C. Uher, C. Wolverton, M.G. Kanatzidis, X. Tang, Discordant nature of Cd in GeTe enhances phonon scattering and improves band convergence for high thermoelectric performance, Journal of Materials Chemistry A 8 (2020) 1193-1204. https://doi.org/10.1039/c9ta10436d.

[5] Z. Liu, W. Gao, W. Zhang, N. Sato, Q. Guo, T. Mori, High Power Factor and Enhanced Thermoelectric Performance in Sc and Bi Codoped GeTe: Insights into the Hidden Role of Rhombohedral Distortion Degree, Advanced Energy Materials 10 (2020) 2002588. https://doi.org/10.1002/aenm.202002588.

[6] M. Li, M. Hong, X. Tang, Q. Sun, W.-Y. Lyu, S.-D. Xu, L.-Z. Kou, M. Dargusch, J. Zou, Z.-G. Chen, Crystal symmetry induced structure and bonding manipulation boosting thermoelectric performance of GeTe, Nano Energy 73 (2020) 104740. https://doi.org/10.1016/j.nanoen.2020.104740.

[7] J. Callaway, H.C. von Baeyer, Effect of Point Imperfections on Lattice Thermal Conductivity, Phys. Rev. 120 (1960) 1149-1154. https://doi.org/10.1103/PhysRev.120.1149.

[8] P.G. Klemens, Thermal Resistance due to Point Defects at High Temperatures, Phys. Rev. 119 (1960) 507-509. https://doi.org/10.1103/PhysRev.119.507.

[9] J. Yang, G.P. Meisner, L. Chen, Strain field fluctuation effects on lattice thermal conductivity of ZrNiSn-based thermoelectric compounds, Appl. Phys. Lett. 85 (2004) 1140-1142. https://doi.org/10.1063/1.1783022.

[10] H. Wang, A.D. LaLonde, Y. Pei, G.J. Snyder, The Criteria for Beneficial Disorder in Thermoelectric Solid Solutions, Adv. Funct. Mater. 23 (2013) 1586-1596. https://doi.org/10.1002/adfm.201201576.

[11] Z. Zheng, X.L. Su, R.G. Deng, C. Stoumpos, H.Y. Xie, W. Liu, Y.G. Yan, S.Q. Hao, C. Uher, C. Wolverton, M.G. Kanatzidis, X.F. Tang, Rhombohedral to cubic conversion of gete via mnte alloying leads to ultralow thermal conductivity, electronic band convergence, and high thermoelectric performance, J. Am. Chem. Soc. 140 (2018) 2673-2686. https://doi.org/10.1021/jacs.7b13611.

APPENDIX B

This appendix B is attached as the supporting information (published) for Paper 2 on Chapter 5: CONDENSED POINT DEFECTS ENHANCE THERMOELECTRIC PERFORMANCE OF RARE EARTH LU-DOPED GETE

Supporting Information

Condensed Point Defects Enhance Thermoelectric Performance of Rare-Earth Lu-Doped GeTe

Wan-Yu Lyu[a, b], Wei-Di Liu[c], Meng Li[b], Xiao-Lei Shi[b], Min Hong[a], Tianyi Cao[b], Kai Guo[d, *], Jun Luo[e], Jin Zou[f, g], Zhi-Gang Chen[b, *]

[a]Centre for Future Materials, University of Southern Queensland, Springfield, Queensland 4300, Australia

[b]School of Chemistry and Physics, Queensland University of Technology, Brisbane, Queensland 4001, Australia

[c]Australian Institute for Bioengineering and Nanotechnology, The University of Queensland, Brisbane, Queensland 4072, Australia

[d]School of Physics and Materials Science, Guangzhou University, Guangzhou 510006, China

[e]School of Materials Science and Engineering, Shanghai University, Shanghai 200444, China

[f]School of Mechanical and Mining Engineering, The University of Queensland, Brisbane, Queensland 4072, Australia.

[g]Centre for Microscopy and Microanalysis, The University of Queensland, Brisbane, Queensland 4072, Australia

*Corresponding authors.

E-mail addresses: zhigang.chen@qut.edu.au (Z.G. Chen); kai.guo@gzhu.edu.cn (K. Guo).

1. **Experimental section**

1.1. Synthesis

The single doping $Ge_{1-x}Lu_xTe$ (x = 0, 0.02, 0.04) and co-doping $Ge_{0.98-y}Lu_{0.02}M_yTe$ (M_y = $Bi_{0.06}$, $Sb_{0.08}$) samples were prepared by melting and quenching method. Raw materials Ge (99.999%, Sigma-Aldrich, Australia), Te (99.999%, Sigma-Aldrich, Australia), Lu (99.99%, Sigma-Aldrich, United States), Bi (99.999%, Alfa-Aesar, United States), and Sb (99.999%, Alfa-Aesar, United States) were weighed following the designed stoichiometric ratio. These mixtures were put in quartz ampules and then sealed in quartz ampules with a high vacuum degree. These mixed samples were heated in 1223 K at a muffle furnace for 1 day and then followed by water quenching. After that, the obtained samples were annealed at 873 K for 3 days. The resultant products were further ground into powders in an agate mortar and then sintered into pellets by SPS (Spark Plasma Sintering, 65 MPa, 673 K, 5 min) for thermoelectric performance measurement.

1.2 Characterization

X-ray diffraction (XRD, Bruker, United States, Cu K_α radiation with a wavelength of 1.5418 Å, 10° $\leq 2\theta \leq$ 80°, step with 0.02°) was used to characterize the crystal structures of as-prepared samples. The valence state of $Ge_{1-x}Lu_xTe$ (x = 0, 0.02, 0.04) was characterized by X-ray photoelectron spectroscopy (XPS, Kratos Axis ULTRA, Kratos Analytical Limited, Japan). The morphologies and compositions of $Ge_{1-x}Lu_xTe$ (x = 0, 0.02, 0.04) and $Ge_{0.98-y}Lu_{0.02}M_yTe$ (M_y = $Bi_{0.06}$, $Sb_{0.08}$) were characterized by a field-emission scanning electron microscope (FE-SEM, JSM-7001F, JEOL, Japan) equipped with an energy dispersive spectrum (EDS) detector.

1.3 Thermoelectrical Property Measurement

Electrical transport properties, including the Seebeck coefficient (S) and electrical conductivity (σ), of the sintered pellets were simultaneously measured by ZEM-3 (ULVAC Technologies, Inc., Japan). Thermal conductivity (κ_{tot}) is calculated by $\kappa_{\mathrm{tot}} = D \times C_{\mathrm{p}} \times \rho$, where D is the thermal diffusivity coefficient measured by the laser flash diffusivity apparatus (LFA 467, Netzsch, Germany), C_{p} is the specific heat estimated from the Dulong–Petit approximation, ρ is the pellet densities measured by Archimedes method. The Hall coefficient (R_{H}) was measured based on the Van der Paw technique to further analyze the transport properties of $Ge_{1-x}Lu_xTe$ (x = 0, 0.02, 0.04) and $Ge_{0.98-y}Lu_{0.02}M_yTe$ (M_y = $Bi_{0.06}$, $Sb_{0.08}$). The n_{H} and μ_{H} were obtained through the equation $n_{\mathrm{H}} = 1/(eR_{\mathrm{H}})$, and $\mu_{\mathrm{H}} = \sigma R_{\mathrm{H}}$, where e is the electron charge.

1.4 Band structure calculation

Density functional theory (DFT) calculations were used to calculate the energy band structure of Lu-doped GeTe. DFT calculations were performed based on a projector-augmented wave method as implemented in the Vienna Ab initio Simulation Package (VASP) [1–3]. Fully relativistic Perdew–Burke–Ernzerhof generalized gradient approximation functional (GGA-PBE) was adopted to tackle the exchange-correlation interactions [4]. A 3 × 3 × 3 supercell of $Ge_{27}Te_{27}$ was built and substituted with one Lu element ($Ge_{26}Lu_1Te_{27}$) for calculation simplicity, corresponding to a doping level of 3 mol.%–4 mol.% in GeTe. Then it was sampled by a 7 × 7 × 7 Monkhorst-Pack k-mesh for relaxation, based on a ve cut-off energy of 450 eV, and a convergence criterion of 1×10^{-7} eV per electron and 1×10^{-3} eV Å^{-1} per atom. The band structures were calculated along a line-mode k-path consisting of the Brillouin path features of the AFLOW framework [5].

2. Basic characteristics of $Ge_{1-x}Lu_xTe$ (x = 0, 0.02, 0.04) and $Ge_{0.98-y}Lu_{0.02}M_yTe$ ($M_y = Bi_{0.06}, Sb_{0.08}$)

2.1. *Composition and density of $Ge_{1-x}Lu_xTe$ (x=0, 0.02, 0.04) and $Ge_{0.98-y}Lu_{0.02}M_yTe$ ($M_y=Bi_{0.06}, Sb_{0.08}$)*

As shown in Table S1, the composition of $Ge_{1-x}Lu_xTe$ (x = 0, 0.02, 0.04) and $Ge_{0.98-y}Lu_{0.02}M_yTe$ ($M_y = Bi_{0.06}, Sb_{0.08}$) was characterized by SEM-EDS mapping.

Table S1. Nominated composition, real composition confirmed by EDS mapping result, real composition confirmed by XPS result, density and relative density of $Ge_{1-x}Lu_xTe$ (x = 0, 0.02, 0.04) and $Ge_{0.98-y}Lu_{0.02}M_yTe$ ($M_y = Bi_{0.06}, Sb_{0.08}$) at room temperature.

Nominated composition	Real composition (by EDS mapping data)	Real composition (by XPS results)	Density (g cm^{-3})	Relative density (%)
GeTe	$Ge_{0.98}Te_1$	$Ge_{0.97}Te_1$	6.09	99%
$Ge_{0.98}Lu_{0.02}Te$	$Ge_{0.98}Lu_{0.01}Te$	$Ge_{0.98}Lu_{0.01}Te_1$	6.04	97%
$Ge_{0.96}Lu_{0.04}Te$	$Ge_{0.96}Lu_{0.01}Te$	$Ge_{0.95}Lu_{0.02}Te_1$	6.07	95%
$Ge_{0.92}Lu_{0.02}Bi_{0.06}Te$	$Ge_{0.9}Lu_{0.01}Bi_{0.06}Te$	NA	5.98	93%

$Ge_{0.90}Lu_{0.02}Sb_{0.08}Te$	$Ge_{0.89}Lu_{0.01}Sb_{0.08}Te$	NA	5.90	93%

Fig. S1 shows the EDS maps of Ge and Te for $Ge_{1-x}Lu_xTe$ (x = 0.02, 0.04) and $Ge_{0.98-y}Lu_{0.02}M_yTe$ (M_y = $Bi_{0.06}$, $Sb_{0.08}$), where a small amount of Ge precipitates can be clearly observed.

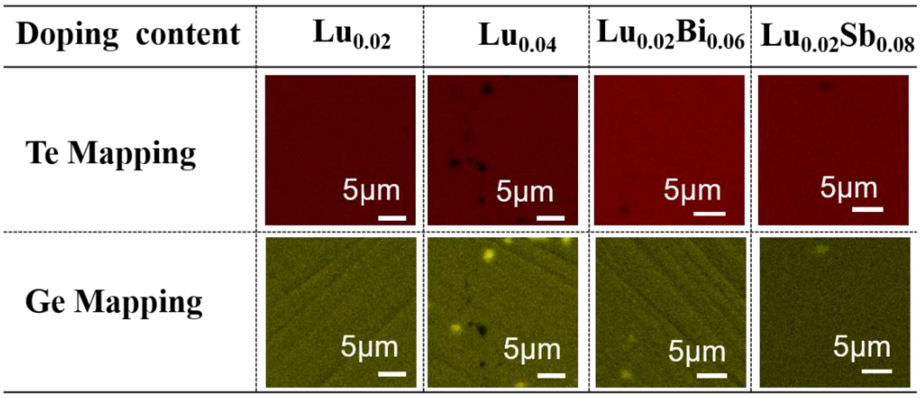

Fig. S1. EDS mapping results of Ge and Te for $Ge_{1-x}Lu_xTe$ (x = 0.02, 0.04) and $Ge_{0.98-y}Lu_{0.02}M_yTe$ (M_y = $Bi_{0.06}$, $Sb_{0.08}$).

3. Electrical transport property

3.1. Electrical transport properties

The determination of effective mass m^* in this work is based on the single parabolic band (SPB) approximation with the acoustic phonon scattering [6].

$$m^* = \frac{h^2}{2k_\mathrm{B}T}\left[\frac{n}{4\pi F_{1/2}(\eta)}\right]^{2/3} \tag{1}$$

$$S = \pm\frac{k_\mathrm{B}}{\mathrm{e}}\left(\frac{2F_1(\eta)}{F_0(\eta)} - \eta\right) \tag{2}$$

$$F_n(\eta) = \int_0^\infty \frac{x^n\,\mathrm{d}x}{1+\mathrm{e}^{x-\eta}} \tag{3}$$

$$\eta = \frac{E_\mathrm{f}}{k_\mathrm{B}T} \tag{4}$$

Where k_B is the Boltzmann constant, e is the electron charge, *h* is the Planck constant, E_f is the Fermi energy, η is the reduced Fermi energy, and $F_n(\eta)$ is the *n*-th order Fermi integral. Based on the measured room temperature Seebeck coefficient (*S*) and carrier concentration (*n*), m^* can then be determined from Eqs. (1–4).”

Table S2. Electrical transport properties of pristine $Ge_{1-x}Lu_xTe$ ($x = 0, 0.02, 0.04$) and $Ge_{0.98-y}Lu_{0.02}M_yTe$ ($M_y = Bi_{0.06}, Sb_{0.08}$) at room temperature.

Composition	n_p (10^{20} cm^{-3})	μ_p (cm^2 V^{-1} s^{-1})	σ (S cm^{-1})	S (µV K^{-1})	m^* (m_0)
GeTe	11.2	41	7463	43.5	2.27
$Ge_{0.98}Lu_{0.02}Te$	10.2	33	5435	48.3	2.37
$Ge_{0.96}Lu_{0.04}Te$	10.7	27	4608	32.2	1.64
$Ge_{0.92}Lu_{0.02}Bi_{0.06}Te$	2.7	29	1271	94.9	1.97
$Ge_{0.90}Lu_{0.02}Sb_{0.08}Te$	1.77	45	1276	106	1.70

4. Lattice thermal conductivity (κ_l) and electrical thermal conductivity (κ_e) calculation

The κ_l is estimated by deducting κ_e from measured κ_{tot}:

$$\kappa_l = \kappa_{tot} - \kappa_e \tag{5}$$

The κ_e is calculated following the Wiedemann−Franz law formula:

$$\kappa_e = L\sigma T \tag{6}$$

where L is the Lorenz number, σ represents the electrical conductivity, and T is the absolute temperature. The L is calculated using the following equation proposed by Kim *et al*. based on a single parabolic band assumption[7]:

$$L = 1.5 + \exp\frac{-|S|}{116} \tag{7}$$

where S is the Seebeck coefficient.

As shown in Fig. S2, κ_e was reduced with the increasing atomic number due to decreased σ.

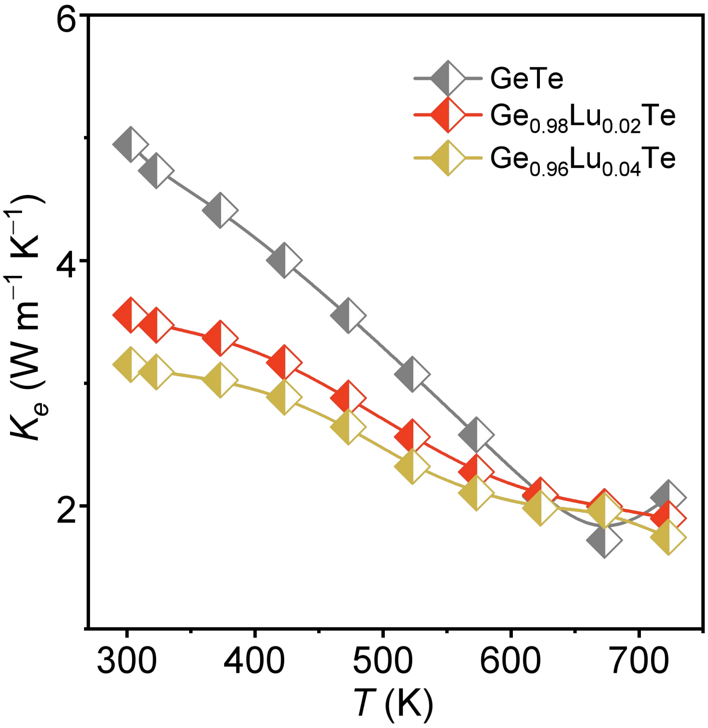

Fig. S2. κ_e of $Ge_{1-x}Lu_xTe$ (x = 0, 0.02, 0.04).

5. Theoretical κ_l of $Ge_{1-x}Lu_xTe$ (x = 0, 0.02, 0.04)

Element substitution can cause lattice fluctuation and lead to a disorder of the crystal matrix, which can be expressed by the Callaway [8] and Klmen [9] model, which has been used by many thermoelectric systems [10–12]. The lattice distribution can be evaluated by κ_l/κ_{l0}, which κ_{l0} represents the lattice thermal conductivity of pristine GeTe, κ_l is calculated lattice thermal conductivity of Lu substituted GeTe.

$$\frac{\kappa_l}{\kappa_{l0}} = \frac{\tan^{-1}(u)}{u} \tag{8}$$

$$u^2 = \frac{\pi^2\theta_D\Omega}{hv_s{}^2}\kappa_{l0}\Gamma_{tot} \tag{9}$$

where u, Ω, v_s, θ_D, and Γ_{tot} are the disorder scaling parameter, the average volume per atom, the sound velocity, the Debye temperature, and the experimental disorder scattering parameter, respectively. Γ_{tot} can be derived from measured κ_l. Total disorder parameter (Γ_{tot}) including strain-field fluctuation (Γ_S) and mass fluctuation (Γ_M) was calculated, where $\Gamma_{tot} = \Gamma_M + \Gamma_S$. Where the scattering parameters Γ_M and Γ_S are due to mass fluctuation, and strain-field fluctuation, respectively. For the binary GeTe, Γ_M and Γ_S are given by Eqs. (10) and (11), where, M1, M2, and M3 are the atomic mass of Ge, Lu, and Te, respectively; r_1 and r_2 are the atomic radii of Ge and Lu, respectively; x is the content of Lu; and ε is regarded as a phenomenological adjustable parameter.

$$\Gamma_M = \frac{1}{2}\left(\frac{\overline{M}}{\overline{\overline{M}}}\right)x(1-x)\left(\frac{M_1-M_2}{\overline{M}}\right)^2 \tag{10}$$

$$\Gamma_S = \frac{1}{2}\left(\frac{\overline{M}}{\overline{\overline{M}}}\right)x(1-x)\varepsilon\left(\frac{r_1-r_2}{\overline{r}}\right)^2 \tag{11}$$

$$\overline{M} = M_1x + M_2(1-x) \tag{12}$$

$$\overline{\overline{M}} = \frac{1}{2}(\overline{M} + M_3) \tag{13}$$

$$\overline{r} = r_1x + r_2(1-x) \tag{14}$$

The experiment disorder scattering parameter, Γ_{exp}, can also be calculated by the Eqs. (8) and (9) with experiment lattice thermal conductivity κ_l of $Ge_{1-x}Lu_xTe$ ($x = 0$, 0.02, 0.04). And the experiment Γ_S can be calculated according to the assumption

$$\Gamma_{\mathrm{exp}} = \Gamma_{\mathrm{M}} + \Gamma_{\mathrm{S}} \quad (15)$$

The results and calculation parameters were shown in Table S3.

Table S3. Parameters for phonon modeling calculation.

Parameter	Description	Values
υ_L	Longitudinal phonon velocity (m s^{-1})	2930
υ_T	Transverse phonon velocity (m s^{-1})	1780
υ_S	Average phonon velocity	1967
θ_D	Acoustic Debye temperature (K)	195
Ω	Average atomic volume (m^{-3})	2.708×10^{-29}
$\bar{M}$	Average atomic mass (kg)	1.66×10^{-25}
γ	Grüneisen parameter	1.56

Reference

[1] G. Kresse, J. Furthmüller, Comput. Mater. Sci. 6 (1996) 15–50.

[2] G. Kresse, D. Joubert, Phys. Rev. B 59 (1999) 1758–1775.

[3] G. Kresse, J. Furthmüller, Phys. Rev. B 54 (1996) 11169–11186.

[4] J.P. Perdew, K. Burke, M. Ernzerhof, Phys. Rev. Lett. 77 (1996) 3865–3868.

[5] W. Setyawan, S. Curtarolo, Comput. Mater. Sci. 49 (2010) 299–312.

[6] H.J. Goldsmid, Introduction to Thermoelectricity, Springer Series in Materials Science, Heidelberg, 2016.

[7] H.S. Kim, Z.M. Gibbs, Y. Tang, H. Wang, G.J. Snyder, APL Mater. 3 (2015) 041506.

[8] J. Callaway, H.C. von Baeyer, Phys. Rev. 120 (1960) 1149–1154.

[9] P.G. Klemens, Phys. Rev. 119 (1960) 507–509.

[10] J. Yang, G.P. Meisner, L. Chen, Appl. Phys. Lett. 85 (2004) 1140–1142.

[11] H. Wang, A.D. LaLonde, Y. Pei, G.J. Snyder, Adv. Funct. Mater. 23 (2013) 1586–1596.

[12] Z. Zheng, X.L. Su, R.G. Deng, C. Stoumpos, H.Y. Xie, W. Liu, Y.G. Yan, S.Q. Hao, C. Uher, C. Wolverton, M.G. Kanatzidis, X.F. Tang, J. Am. Chem. Soc. 140 (2018) 2673–2686.

APPENDIX C

This appendix C is attached as the supporting information (published) for Paper 3 on Chapter 6: RARE-EARTH ND INDUCING RECORD-HIGH THERMOELECTRIC PERFORMANCE OF $(GeTe)_{85}(AgSbTe_2)_{15}$

Supporting Information

Rare-earth Nd Inducing record-high thermoelectric performance of $(GeTe)_{85}(AgSbTe_2)_{15}$

W. Y. Lyu,[1,2] M. Hong,[1,2] W. D. Liu,[1,2] M. Li,[2] Q. Sun,[2] S. D. Xu,[2] J. Zou,[2,3] Z. G. Chen[1,2,] *

[1]Centre for Future Materials, University of Southern Queensland, Springfield, Queensland 4300, Australia.

[2]School of Mechanical and Mining Engineering, The University of Queensland, Brisbane, Queensland 4072, Australia.

[3]Centre for Microscopy and Microanalysis, The University of Queensland, Brisbane, Queensland 4072, Australia.

Email: zhigang.chen@usq.edu.au (ZGC);

1. Hall mobility (μ) of the Nd-doped TAGS-85

As shown in **Figure S1**, μ decreases from 10.8 to 9.3 $cm^2V^{-1}s^{-1}$ and then increase to 10.3 $cm^2V^{-1}s^{-1}$ at 300 K with adding Nd content, which may attributed to the alloy defect scattering [1].

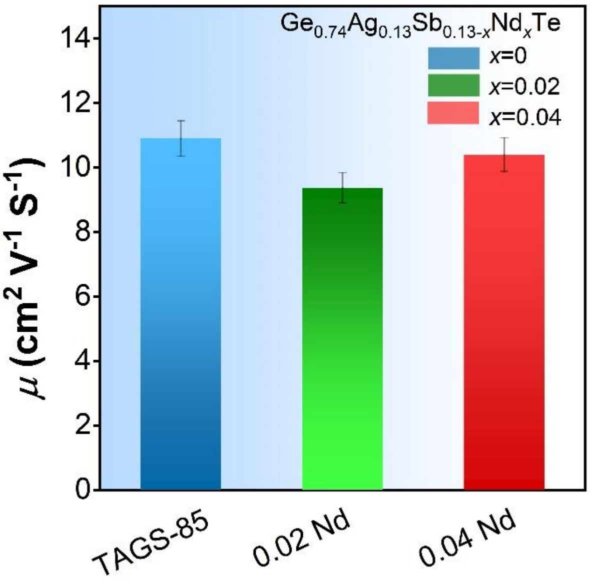

Figure S1. Hall mobility (μ) of the Nd-doped TAGS-85 at the room temperature.

2. As shown in **Table S1,** high density values were obtained for all samples.

Table S1. The density of as-prepared samples.

Composition	Density (g cm^{-3})
$Ge_{0.74}Ag_{0.13}Sb_{0.13}Te$	6.3779
$Ge_{0.74}Ag_{0.13}Sb_{0.11}Nd_{0.02}Te$	6.4068
$Ge_{0.74}Ag_{0.13}Sb_{0.09}Nd_{0.04}Te$	6.3773

Reference

[1] H. Wang; A. D. LaLonde; Y. Pei; G. J. Snyder, *Adv. Funct. Mater.* **2013,** *23*, 1586-1596.